



Characterization of the plasma electrolytic oxidation of titanium in sodium metasilicate

S. Stojadinović^{a,*}, R. Vasilčić^b, M. Petković^a, B. Kasalica^a, I. Belča^a, A. Žekić^a, Lj. Zeković^a

^a Faculty of Physics, University of Belgrade, Studentski trg 12-16, 11000 Belgrade, Serbia

^b Faculty of Environmental Governance and Corporate Responsibility, Educons University, Vojvode Putnika 87, Sremska Kamenica, Serbia

ARTICLE INFO

Article history:

Received 9 July 2012

Received in revised form 20 October 2012

Accepted 30 October 2012

Available online 6 November 2012

Keywords:

Titanium

Plasma electrolytic oxidation (PEO)

Sodium metasilicate

Optical emission spectroscopy

ABSTRACT

Plasma electrolytic oxidation (PEO) of titanium in sodium metasilicate at 200 mA/cm² is investigated using real-time imaging and optical emission spectroscopy. It has been detected that during the PEO process the size of microdischarges becomes larger, while the number of microdischarges is reduced. The species and their ionization states present in PEO microdischarges are identified. The species originate both from titanium anode and from the electrolyte. The spectral line shape analysis of hydrogen Balmer line H_β (486.13 nm) indicates the presence of two types of microdischarges during PEO. The discharges are characterized by relatively low electron number densities of $N_e = 3.8 \times 10^{15} \text{ cm}^{-3}$ and $N_e = 4.5 \times 10^{16} \text{ cm}^{-3}$. For electron temperature (T_e) measurement we used Ti I lines at 398.18 nm and 501.42 nm and obtained T_e in the range of $3700 \pm 500 \text{ K}$. Surface coatings formed by PEO process were characterized by AFM, SEM-EDX and XRD. The main elemental components of PEO coatings are Ti, Si and O. The PEO coatings are partly crystallized and mainly composed of anatase, rutile, and amorphous SiO₂.

© 2012 Elsevier B.V. All rights reserved.

1. Introduction

Titanium and its alloys are important engineering materials featuring high strength-to-weight ratio, good corrosion resistance, high melting point, good mechanical behavior, and a good biocompatibility. Because of these properties they are becoming significantly important in many industries such as aerospace, automobile, biomedical, energy, military and biomedicine. [1–3]. However, low wear resistance and high friction coefficient limit their extensive applications. Anodization of titanium and its alloys are one of the methods used for forming protective oxide coatings that can help to overcome these deficiencies. In recent years, high-voltage anodization, so-called plasma electrolytic oxidation, has proved to be a very useful technique for the formation of protective oxide coatings [4–8].

Plasma electrolytic oxidation (PEO), also called microarc oxidation (MAO) or anodic spark deposition (ASD), is an economic, efficient, and environmentally benign technology capable of producing a stable oxide coating on the surface of lightweight metals (aluminum, magnesium, zirconium, titanium, etc.) or metal alloys [9,10]. Oxide coatings have controllable morphology and composition, excellent bonding strength with the substrate, good electrical

and thermal properties, high microhardness, and high-quality wear and corrosion resistance.

PEO process is coupled with the formation of plasma, as indicated by the presence of microdischarges on the metal surface, accompanied by gas evolution [11,12]. The anodic gas consists predominantly of oxygen with minor fractions of other elements [13]. Various processes including chemical, electrochemical, thermodynamical, and plasma-chemical reactions occur at the discharge sites, due to increased local temperature (10^3 K to 10^4 K) and pressure ($\sim 10^2 \text{ MPa}$). These processes are responsible for modifying the structure, composition and morphology of obtained oxide coatings. The oxide coatings formed by PEO process usually contain crystalline and amorphous phases with constituent species originating both from metal and electrolyte.

Understanding the microdischarge phenomena is important for characterization of the PEO process. Distribution and types of microdischarges have important effects on the formation mechanism, composition, morphology, and various properties of the resultant oxide coatings. Given the liquid environment, optical emission spectroscopy (OES) is the best available technique for PEO plasma characterization. The most popular application of OES for PEO diagnostics is spectra characterization and observation of temporal evolution of spectral lines in the visible and near UV spectral region. The main difficulty in an application of OES for PEO characterization comes from space and time inhomogeneity of microdischarges appearing randomly across the anode surface. Despite numerous articles using OES for the characterization of

* Corresponding author. Tel.: +381 11 7158161; fax: +381 11 3282619.
E-mail address: sstevan@ff.bg.ac.rs (S. Stojadinović).

the PEO process on metals, mostly on aluminum [14–22] and magnesium [22–26], there is a deficiency of data on the OES characterization of the PEO process on titanium and titanium alloys [27,28].

The present paper describes PEO process of titanium in sodium metasilicate. Since the occurrence of plasma electrolytic oxidation is both electrolyte and metal sensitive we have decided to use sodium metasilicate solution because of good experience we had in our previous investigations of the PEO process on magnesium and its alloys [25,26]. At the same time, electrolytes containing sodium metasilicate are among the most commonly used electrolytes for the formation of oxide coatings by PEO process on lightweight metals. Microdischarge characteristics during PEO process of titanium were investigated by optical emission spectroscopy and real-time imaging. Atomic force microscopy (AFM), scanning electron microscopy (SEM-EDX) and x-ray diffraction (XRD) served as tools for examining surface morphology, chemical and phase composition of obtained oxide coatings.

2. Experimental

In the experiment, oxide coatings were formed on titanium samples of dimensions 25 mm × 5 mm × 0.25 mm and 99.5% purity. Before the anodization, samples were degreased in acetone, ethanol and distilled water, using ultrasonic cleaner, and dried in a warm air stream. The oxidation process was carried out in an electrolytic cell with flat glass windows [29]. Platinum wires were used as cathodes. For anodization of titanium we used water solution of 10 g/l Na₂SiO₃·5H₂O. The electrolyte was prepared by using double distilled and deionized water and PA (pro analysis) grade chemical compound. Anodizing was carried out at current density of 200 mA/cm². During the anodization, the electrolyte circulated through the chamber–reservoir system. The temperature of the electrolyte was maintained during the anodization process at (294 ± 1) K. After anodization, the samples were rinsed in distilled water to prevent additional deposition of electrolyte components during drying.

Spectral luminescence measurements during PEO of titanium were taken on a spectrometer system based on the intensified charge coupled device (ICCD). Optical detection system consisted of a large-aperture achromatic lens, a Hilger spectrometer with diffraction grating of 1200 grooves/mm (wavelength range of 43 nm), and a very sensitive PI-MAX ICCD thermoelectrically cooled camera (233 K) with high quantum efficiency, manufactured by Princeton Instruments. The system was used with several grating positions with overlapping wavelength range of 5 nm. In all experiments the image of the anode surface was projected with unity magnification to the entrance slit of spectrograph. The optical-detection systems were calibrated using a standard tungsten strip lamp (OSRAM Wi-17G). The obtained spectra were adjusted to the spectral response of the measuring system.

Real-time images during PEO were recorded utilizing a video camera Sony DCR-DVD110 (800 K pixels CCD, 40× optical zoom and 40 mm lens filter). The information obtained was split into separate frames and the image of individual frames was processed using our custom made software, which counts microdischarges in selected frame and determines spatial density of discharges including their dimensional distribution.

The topography and roughness of oxide coatings were characterized using an atomic force microscope (AFM; Veeco Instruments, model Dimension V). Micrographs were obtained in tapping mode under ambient conditions, using TAP300 tips (resonant frequency 300 kHz, force constant 40 N/m). Roughness data were obtained using diNanoScope software (version 7.0).

Scanning electron microscope (SEM) JEOL 840A equipped with X-ray energy dispersive spectroscopy (EDX) was used to characterize morphology and chemical composition of formed surface coatings. The crystallinity of samples was analyzed by X-ray powder diffraction (XRD), using a Phillips PW 1050 powder diffractometer in Bragg-Brentano geometry, with Ni-filtered Cu K α radiation ($\lambda = 1.54178 \text{ \AA}$). Diffraction data were acquired over scattering angle 2θ from 10° to 80° with a step of 0.050° and acquisition time of 1s/step.

3. Results and discussion

3.1. Spectroscopic and real-time imaging characterization of PEO process

Fig. 1 shows typical voltage versus time and luminescence intensity versus time characteristics during anodization of titanium samples in 10 g/l Na₂SiO₃·5H₂O at current density of 200 mA/cm². The relatively uniform growth of a compact barrier oxide film, at constant current density, is characterized by an almost linear increase in the anodization voltage. This stage of anodization is followed by apparent deflection from linearity in voltage–time curve, starting from so-called breakdown voltage. After the breakdown, voltage continually increases, but the voltage–time slope decreases and a large number of small size microdischarges appear, evenly distributed over the whole sample surface.

The appearance of microdischarges at various stages of PEO process of titanium is shown in Fig. 2. First microdischarges are visible after 15 s, accompanied by low acoustic emissions. During the PEO process the size of microdischarges becomes larger, while the number of microdischarges is reduced. It can be seen that relatively small microdischarges, with average cross-sectional area $\approx 0.03 \text{ mm}^2$, are dominant in the early stage of PEO process. The population of small microdischarges decreases during PEO. On the other hand, large microdischarges become noticeable with extended PEO time and after about 3 min large microdischarges with average cross-sectional area $\geq 0.13 \text{ mm}^2$ are dominant, while small microdischarges are being hardly observed on the surface.

The increased size and decreased spatial density of microdischarges during PEO is related to the number of discharging sites through which higher anodic current is able to pass. The surface topography of oxide coatings in various stages of PEO process (Fig. 3) shows that the number of micropores decreases, while their size increases during PEO process. Also, thicker coatings have higher surface roughness. In the initial stage of PEO, the discharge channels are well distributed and oxide coatings exhibit

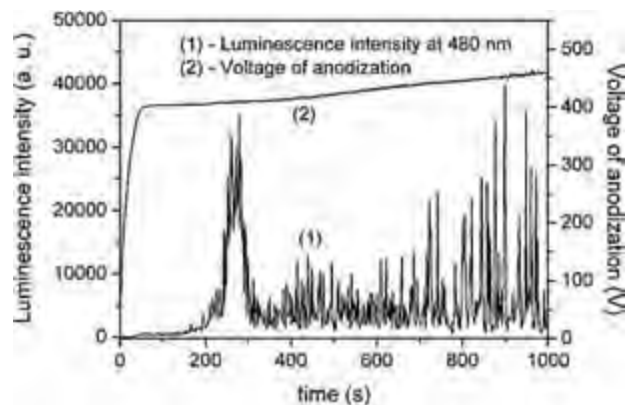


Fig. 1. Time variation of voltage of anodization and luminescence intensity at 480 nm during galvanostatic anodization of titanium in sodium metasilicate.

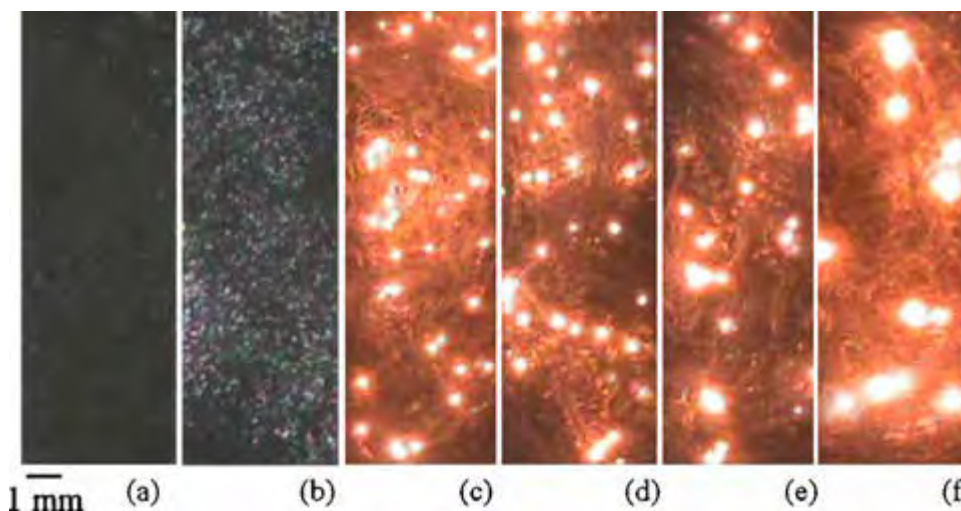


Fig. 2. Microdischarge appearance at various stages of PEO process: (a) 15 s; (b) 30 s; (c) 150 s; (d) 300 s; (e) 600 s; (f) 1200 s.

lower surface roughness (~ 280 nm, Fig. 3a). As the number of discharge channels decreases with PEO time, non-uniformities in the oxide coatings appear causing an increase in surface roughness (~ 1600 nm, Fig. 3c). In a thicker layer of oxide coating, higher energy is required for the current to pass through it. Under this condition, the current is localized at weak points of the layer formed to find its way through the oxide coating. This is the reason why the diameter of the discharge channels increases.

Typical optical emission spectrum of PEO microdischarges in the spectral range from 370 nm to 850 nm is shown in Fig. 4. Atomic and ionic lines were identified using the NIST online spectral database [30]. The strongest lines originate from electrolyte and belong to Na I at 588.99 nm and 589.59 nm, Balmer line H_{α} (656.28 nm), O I at 777.19 nm, 777.42 nm, 777.54 nm, Na I at 818.33 nm and 819.47 nm, O I at 844.62 nm, 844.64 nm and 844.68 nm. We also detected the following relatively strong lines: Balmer line H_{β} (486.13 nm), O I at 715.67 nm, three lines of O I at 794.75 nm, 795.08 nm, 795.22 nm. In order to identify weaker emission lines at lower wavelengths we thoroughly investigated the spectral region from 375 nm to 510 nm (Fig. 5). Many lines of O II, Balmer line H_{γ} (434.05 nm) and Si II which originate from electrolyte as well as Ti I and Ti II lines from substrate are identified. The notations I and II refers to neutral and singly ionized atoms, respectively. The continuum emission between 370 nm and 850 nm results from collision–radiative recombination of electrons [31] and bremsstrahlung radiation [14].

For the explanation of microdischarge formation during PEO process two models were suggested. According to the first model [32,33], the appearance of microdischarges is a result of dielectric breakdown of oxide layer in strong electric field ($\sim 10^7$ V/m). The second model [16,34] considers microdischarges as a gas discharges occurring in a micropores of the oxide films. The formation of a gas phase in micropores is induced by initial dielectric breakdown of a barrier layer in the bottom of the micropores. The temporal variation of the intensity of different lines during the PEO, after subtracting the continuum emission, is shown in Fig. 6. Three lines O II at 459.09 nm, H I at 486.13 nm, and Ti I at 498.17 nm were recorded simultaneously. Emission line intensity indicates that the species in the plasma have similar trends over the treatment time. Among these lines, Ti line gives information about phenomena occurring at the titanium/oxide interface. At the beginning of the PEO process, emission lines are not observed in optical emission spectrum and luminescence originates from radiative recombination of electrons at flaws in oxide coatings [31,33]. During the PEO process, when the electric field in the oxide layer reaches a critical value beyond

which the film breaks down, a number of channels are formed and plasma chemical reactions take place in the channels.

According to Hussein et al. [16] three plasma discharge models have been proposed (see, Fig. 9 in [16]): metal–oxide interface discharge type (B) and oxide–electrolyte interface discharge types within the coating upper layer (A) and at the coating top layer (C). Our recent investigation of PEO process of different metals have shown that type of discharge with evaporation of anodic material (type B) always occurs during PEO of aluminum and magnesium [19,22] regardless of the type of electrolyte, but does not occur during the PEO of tantalum [12] and titanium [27] in 12-tungstosilicic acid. We assumed that the high melting temperature of tantalum ($T_m = 3290$ K) and titanium ($T_m = 1941$ K) does not allow evaporation of anode material during PEO, unlike in the case of PEO on aluminum and magnesium. Aluminum and magnesium have much lower melting point (for aluminum $T_m = 933$ K, for magnesium $T_m = 923$ K), what is of importance for metal plasma generation in discharge channels after evaporation of anode materials. With tantalum and titanium metals in 12-tungstosilicic acid plasma is not generated and lines of Ta and Ti were not detected in PEO spectra.

In contrast, during the PEO of titanium in sodium metasilicate all three discharge models can be distinguished. More intense microdischarges of titanium in sodium metasilicate (compared to those in 12-tungstosilicic acid) [27] are related to the evaporation of titanium substrate. Therefore, Ti I and Ti II lines are emitted from titanium plasma generated in microchannels across the oxide layer, corresponding to process of type B, while hydrogen, oxygen and sodium lines are related to processes of type A (discharge in relatively small holes near the surface of oxide layer) and type C (discharge in the micropores at the surface of oxide layer). Distinctive intensity spikes in Fig. 6 may be attributed to the strong discharges through oxide layer.

For electron number density measurements (N_e), we used plasma broadened profile of Balmer H_{β} line. Balmer line H_{α} is very strong in PEO process (Fig. 4) and strongly self-absorbed [12,19,22]. For this reason H_{α} is not suitable for the spectral line shape analysis. Weaker Balmer line H_{γ} in PEO process interferes with O II lines (Fig. 5b) and is too noisy to be used for reliable spectral line shape analysis. During the analysis of the H_{β} line profile (Fig. 7), it was found that the H_{β} line shape can be properly fitted only if two Lorentzian profiles are used. Full Width at Half Maximum (FWHM) of the upper part of the H_{β} profile is ~ 0.25 nm, while for the broad lower profile FWHM is ~ 1.31 nm. This is in conjunction with empirical

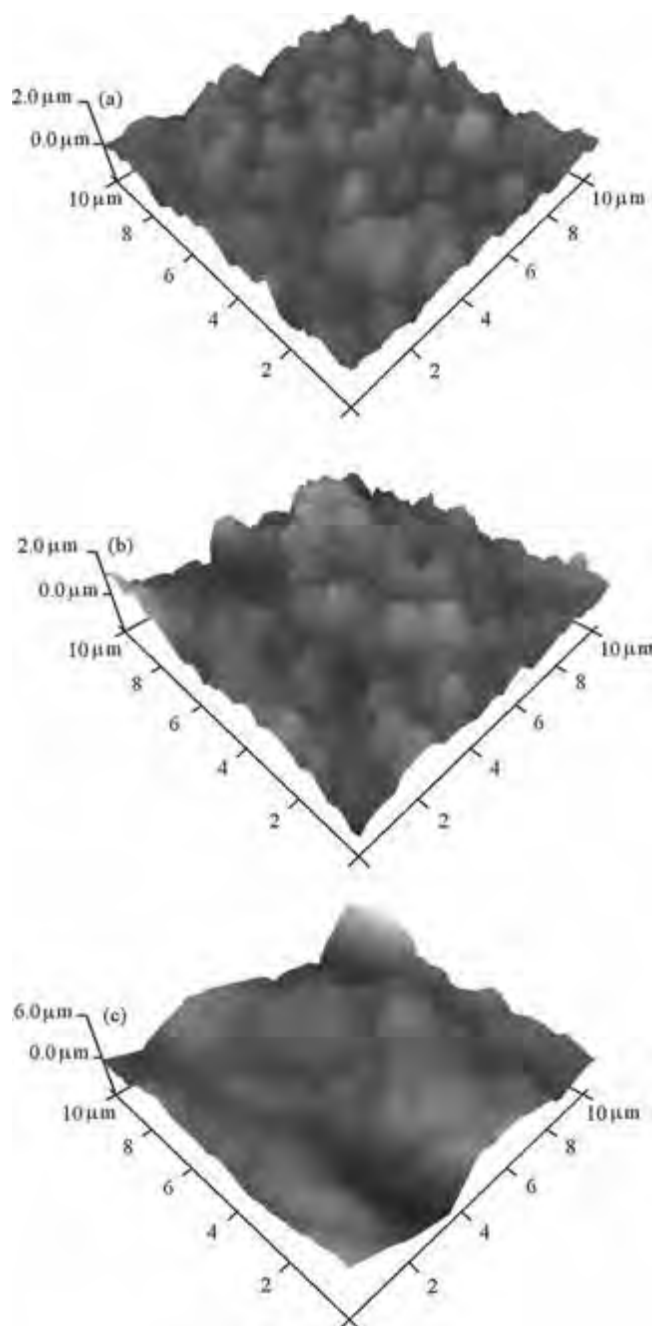


Fig. 3. Three-dimensional AFM images of oxide coatings formed at various stages of PEO process: (a) 1.5 min; (b) 3 min; (c) 5 min.

formula (2a) in [35], corresponding to $N_e = 3.8 \times 10^{15} \text{ cm}^{-3}$ and $N_e = 4.5 \times 10^{16} \text{ cm}^{-3}$, indicating that two plasma processes in discharges always occur. These two electron number densities are close to corresponding N_e results for PEO process on other metals [12,19,22,27].

For electron temperature measurements (T_e) relative line intensities were used. This temperature is assumed to be equal to electron excitation temperature, measured from relative line intensities. For the application of this assumption one must be sure that energy levels used for T_e measurement are populated in accordance with Boltzmann equilibrium distribution i.e. that the upper energy level of the spectral line used is above the lowest level determined by Partial Local Thermal Equilibrium (PLTE) condition. The discussion of the fulfillment of PLTE is given in [19].

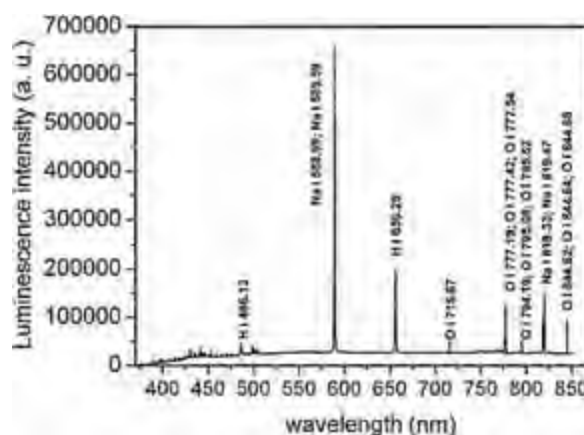


Fig. 4. Optical emission spectrum obtained during PEO in the range from 370 nm to 850 nm.

The relative line intensities of the same atomic species can be used to calculate T_e using the equation [36]:

$$T_e = \frac{E_{m(2)} - E_{m(1)}}{k \cdot \ln[(I_1 \cdot A_{mn(2)} \cdot g_{m(2)} \cdot \lambda_{o(1)}) / (I_2 \cdot A_{mn(1)} \cdot g_{m(1)} \cdot \lambda_{o(2)})]} \quad (1)$$

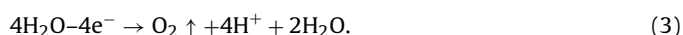
where k is the Boltzmann constant, I_1 and I_2 are relative line intensities of the same species, $A_{mn(i)}$ are the transition probabilities, m is the upper and n is the lower level of the respective lines, $g_{m(i)}$ are the statistical weights of the upper level, $E_{m(i)}$ are energies of the upper levels of the lines and $\lambda_{o(i)}$ are the wavelengths of the line centers in vacuum. For T_e measurement we used Ti I lines (Table 1) at 398.18 nm and 501.42 nm. Difficulty in estimation of T_e using Eq. (1) is related to the question whether T_e in PEO is measured from the same plasma region and in the same time of microdischarge evolution. Since it is not possible to perform space and time resolved microdischarge PEO diagnostics with presently available plasma diagnostic techniques, T_e is measured in a standard way from time integrated relative line intensities. We performed a series of measurements with different integration times and obtained T_e in the range $(3700 \pm 500) \text{ K}$.

3.2. Chemical and phase compositions of PEO coatings

PEO is a complex process combining concurrent partial processes of oxide formation, dissolution, and dielectric breakdown [37]. At the beginning of the titanium anodization, oxide layer grows at the titanium/oxide and oxide/electrolyte interfaces as a result of migration of $\text{O}^{2-}/\text{OH}^-$ and Ti^{4+} ions across the oxide, assisted by a strong electric field. Initial oxide layer forms at the surface of titanium as a result of the following anodic reaction:



while the reaction at the oxide/electrolyte interface is:



The overall reaction is:

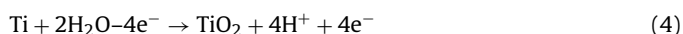


Table 1

The list of the Ti I lines used for the calculation of T_e : λ -wavelength; g_k -statistical weight of upper energy level; A_{ik} -transition probability [30].

Line	λ (nm)	Transition	g_k	Energy (eV)	A_{ki} (10^8 s^{-1})
Ti I	398.18	$3d^2 4s^2 - 3d^2(^3F)4s4p(^1P^\circ)$	5	3.109	0.376
Ti I	501.42	$3d^2 4s^2 - 3d^2(^3F)4s4p(^3P^\circ)$	3	2.469	0.053

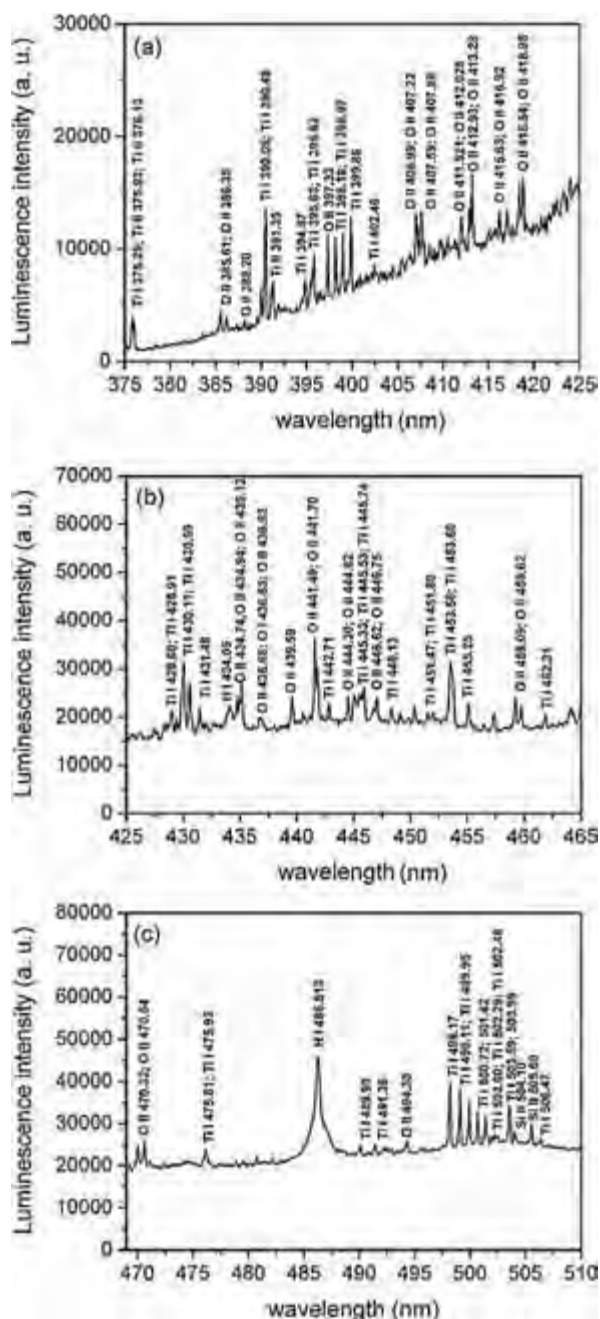


Fig. 5. Optical emission spectra obtained during PEO in the range of (a) 375–425 nm; (b) 425–465 nm; (c) 465–510 nm.

During the PEO process, anionic components of the electrolyte are drawn into the discharge channels. Concurrently, titanium melts out of the substrate, enters the channels, and gets oxidized. At the same time, a separation of oppositely charged ions occurs in the channel due to the presence of the electric field. The cations are ejected from the channels into the electrolyte by electrostatic forces. In the next step, oxidized metal is ejected from the channels into the coating surface in contact with the electrolyte and in that way increases the coating thickness around the channels. Finally, discharge channels get cooled and the reaction products are deposited onto its walls. This process repeats itself at a number of discrete locations over the coating surface, leading to the increase in the coating thickness.

In silicate electrolyte system SiO_3^{2-} ions are transported to the coating/electrolyte interface and under high electric field and high

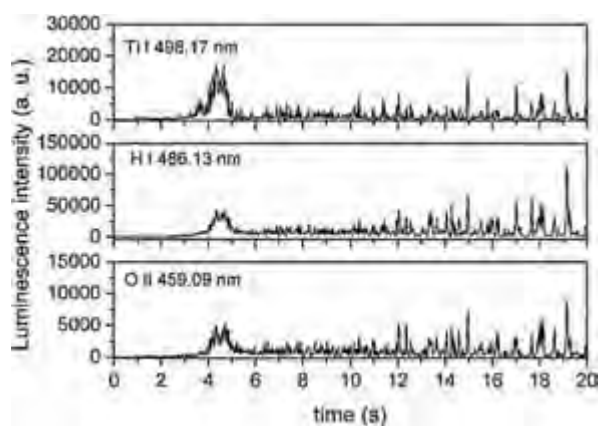


Fig. 6. The temporal variation of the intensity of different lines during the PEO, after subtracting the continuum emission: O II at 459.09 nm; H I at 486.13 nm; and Ti I at 498.17 nm.

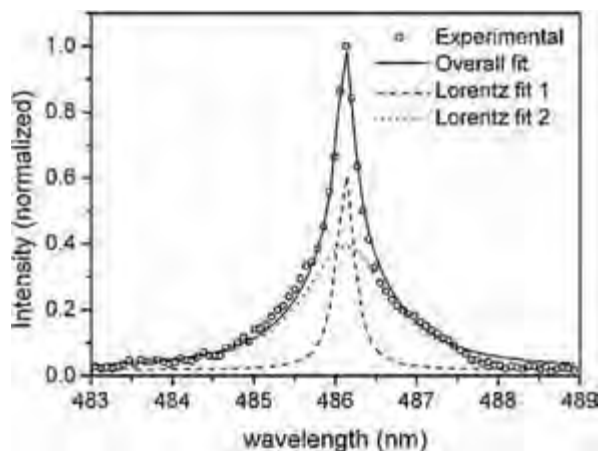


Fig. 7. The H β line profile fitted with two Lorentzian profiles.

temperature conditions, the following reactions can be proposed [38,39]:



Based on the above reactions, increase of PEO time results in the increase of Si content on the top of obtained oxide coatings.

SEM micrographs of the surface coatings obtained at various stages of PEO process are shown in Fig. 8. After breakdown the oxide surface becomes laced with a number microdischarge channels as well as molten regions formed due to rapid cooling effect of the electrolyte. Results of the EDX analyses of surface coatings in Fig. 8 are shown in Table 2. Main elements of the coatings are Ti, O, and

Table 2
EDX analysis of surface coatings in Fig. 8.

Sample	Weight (%)			
	O	Ti	Si	Na
Fig. 2b	38.62	55.94	5.44	
Fig. 2c	54.85	29.12	15.08	0.95
Fig. 2d	55.57	24.38	18.92	1.13
Fig. 2e	56.65	7.71	33.63	2.01
Fig. 2f	56.65	6.17	35.16	2.02

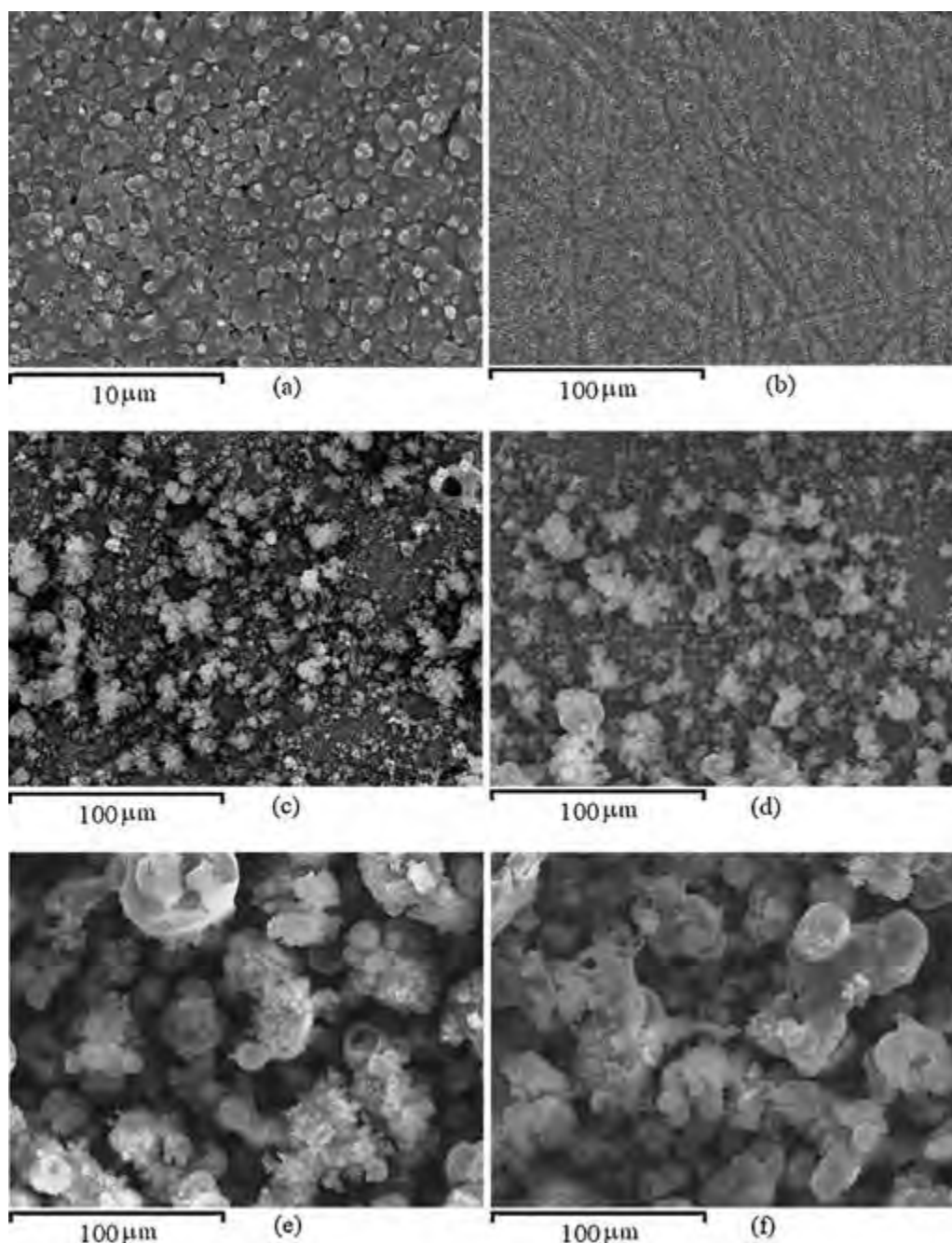


Fig. 8. SEM micrographs of oxide coatings formed at various stages of PEO process: (a) 1.5 min – higher magnification; (b) 1.5 min – lower magnification; (c) 3 min; (d) 5 min; (e) 10 min; (f) 20 min.

Si. The XRD patterns of oxide coatings obtained after various PEO times are shown in Fig. 9. The coatings are partly crystallized and mainly composed of anatase (A) and rutile (R). Amorphous SiO_2 is also detected. Elemental Ti mainly originates from the substrate and therefore Ti diffraction lines are strong. It is clear that species from the electrolyte are incorporated during PEO into the coating layer. The amount of Si in oxide coatings increases with PEO time while the amount of Ti decreases. TiO_2 film forms due to oxidation of titanium during PEO process at titanium/oxide coating interface. For this reason content of Ti is higher in the early stage of PEO process, i.e., for thinner oxide coatings.

The species from the electrolyte are incorporated during PEO oxidation into the outer layer of oxide coating. Contents of Si

increases with PEO time, implying that SiO_2 is predominantly formed in the outer layer of oxide coating. To test this assumption another SEM-EDX experiment was done. SEM micrograph and EDX of three different regions on surface coating processed for 20 min

Table 3
EDX analysis of surface coating in Fig. 10 formed by PEO for 20 min.

	Weight (%)			
	O	Ti	Si	Na
Spectrum 1	38.01	1.82	59.03	1.14
Spectrum 2	7.15	89.96	3.16	
Spectrum 3	58.75	0.55	38.50	2.21

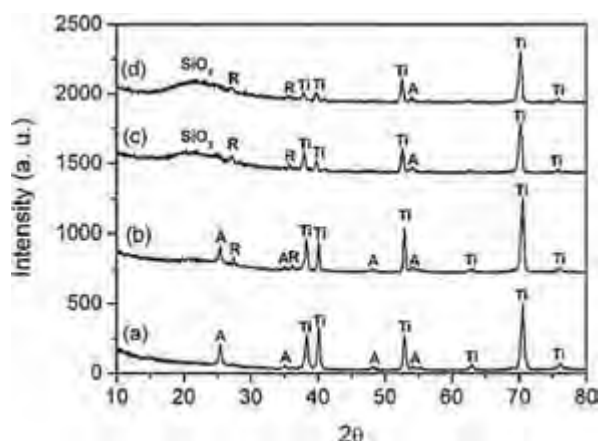


Fig. 9. XRD patterns of oxide coatings formed at various stages of PEO process: (a) 3 min; (b) 5 min; (c) 10 min; (d) 20 min.

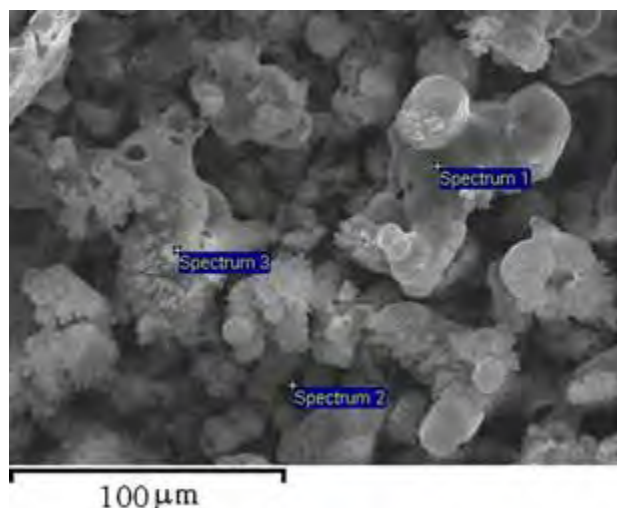


Fig. 10. SEM micrograph with marked positions of EDX spectra in Table 3 of oxide coating formed by PEO for 20 min.

are presented in Fig. 10. Spectrum 1 and spectrum 3 are taken in the area around the discharge channel, while the spectrum 2 is taken in the region where the discharge takes place. It is clear that the content of Ti is much higher in the discharged channel, while content of Si is much higher in the surrounding area, confirming that SiO_2 is predominantly formed in the outer layer of oxide coating.

4. Conclusion

We have studied plasma electrolytic oxidation (PEO) process of titanium in sodium metasilicate. The following conclusions were drawn:

- The size of microdischarges appearing at the oxide/electrolyte interface becomes larger, while the number of microdischarges is reduced, with increasing time of PEO.
- The species that are identified in optical emission spectrum of microdischarges originate either from titanium electrode or from the electrolyte.
- The analysis of hydrogen Balmer line H_β shape indicates the presence of two types of discharges during PEO and electron number density of $N_e = 3.8 \times 10^{15} \text{ cm}^{-3}$ and $N_e = 4.5 \times 10^{16} \text{ cm}^{-3}$ is determined. Plasma electron temperature in the range of

$(3700 \pm 500) \text{ K}$ is estimated from the line intensity ratios of Ti I lines at 398.18 nm and 501.42 nm.

- The surface coatings morphology is strongly dependent on PEO time. During the PEO of titanium density of discharge channels decreases while their diameter increases, resulting in increased roughness of the surface coating. The main elemental components of PEO coatings are Ti, O and Si. The PEO coatings are partly crystallized and mainly composed of anatase, rutile and amorphous SiO_2 .

Acknowledgement

This work is supported by the Ministry of Education and Science of the Republic of Serbia under project no. 171035.

References

- [1] W.D. Brewer, R.K. Bird, T.A. Wallace, *Materials Science and Engineering A* 243 (1998) 299–304.
- [2] C. Leyens, M. Peters, *Titanium and Titanium Alloys: Fundamentals and Applications*, Wiley-VCH, Weinheim, Germany, 2003.
- [3] X. Fana, B. Fenga, Y. Dia, X. Lua, K. Duana, J. Wanga, J. Wenga, *Applied Surface Science* 258 (2012) 7584–7588.
- [4] A.L. Yerokhin, X. Niea, A. Leyland, A. Matthews, *Surface and Coatings Technology* 130 (2000) 195–206.
- [5] M. Mu, X. Zhou, Q. Xiao, J. Liang, X. Huo, *Applied Surface Science* 258 (2012) 8570–8576.
- [6] M. Shokouhfar, C. Dehghanian, A. Baradaran, *Applied Surface Science* 257 (2011) 2617–2624.
- [7] D. Krupa, J. Baszkiewicz, J. Zdunek, J. Smolik, Z. Słomka, J.W. Sobczak, *Surface and Coatings Technology* 205 (2010) 1743–1749.
- [8] M. Montazeri, C. Dehghanian, M. Shokouhfar, A. Baradaran, *Applied Surface Science* 257 (2011) 7268–7275.
- [9] A.L. Yerokhin, X. Nie, A. Leyland, A. Matthews, S.J. Dowey, *Surface and Coatings Technology* 122 (1999) 73–93.
- [10] M. Petković, S. Stojadinović, R. Vasilic, Lj. Zeković, *Applied Surface Science* 257 (2011) 10590–10594.
- [11] S. Stojadinovic, R. Vasilic, I. Belca, M. Petkovic, B. Kasalica, Z. Nedic, Lj. Zekovic, *Corrosion Science* 52 (2010) 3258–3265.
- [12] S. Stojadinović, J. Jovović, M. Petković, R. Vasilic, N. Konjević, *Surface and Coatings Technology* 205 (2011) 5406–5413.
- [13] L.O. Snizhko, A.L. Yerokhin, A. Pilkington, N.L. Gurevina, D.O. Misnyankin, A. Leyland, A. Matthews, *Electrochimica Acta* 49 (2004) 2085–2095.
- [14] M.D. Klapkiv, H.M. Nykyforchyn, V.M. Posuvailo, *Materials Science* 30 (1994) 333–343.
- [15] C.S. Dunleavy, I.O. Golosnoy, J.A. Curran, T.W. Clyne, *Surface and Coatings Technology* 203 (2009) 3410–3419.
- [16] R.O. Hussein, X. Nie, D.O. Northwood, A. Yerokhin, A. Matthews, *Journal of Physics D: Applied Physics* 43 (2010) 105203–105213.
- [17] R.O. Hussein, X. Nie, D.O. Northwood, *Surface and Coatings Technology* 205 (2010) 1659–1667.
- [18] F. Mecuson, T. Czerwicz, T. Belmonte, L. Dujardin, A. Viola, G. Henrion, *Surface and Coatings Technology* 200 (2005) 804–808.
- [19] J. Jovović, S. Stojadinović, N.M. Šišović, N. Konjević, *Surface and Coatings Technology* 206 (2011) 24–28.
- [20] S. Stojadinović, M. Perić, M. Petković, R. Vasilic, B. Kasalica, I. Belča, J. Radić-Perić, *Electrochimica Acta* 56 (2011) 10122–10129.
- [21] M. Petković, S. Stojadinović, R. Vasilic, I. Belča, Z. Nedić, B. Kasalica, U.B. Mioč, *Applied Surface Science* 257 (2011) 9555–9561.
- [22] J. Jovović, S. Stojadinović, N.M. Šišović, N. Konjević, *Journal of Quantitative Spectroscopy and Radiative Transfer* 113 (2012) 1928–1937.
- [23] L. Wang, L. Chen, Z.C. Yan, W. Fu, *Surface and Coatings Technology* 205 (2010) 1651.
- [24] R.O. Hussein, P. Zhang, X. Nie, Y. Xia, D.O. Northwood, *Surface and Coatings Technology* 206 (2011) 1990–1997.
- [25] S. Stojadinović, R. Vasilic, M. Petković, I. Belča, B. Kasalica, M. Perić, Lj. Zeković, *Electrochimica Acta* 59 (2012) 354–359.
- [26] S. Stojadinović, M. Perić, J. Radić-Perić, R. Vasilic, M. Petković, Lj. Zeković, *Surface and Coatings Technology* 206 (2012) 2905–2913.
- [27] S. Stojadinović, R. Vasilic, M. Petković, Lj. Zeković, *Surface and Coatings Technology* 206 (2011) 575–581.
- [28] R.O. Hussein, X. Nie, D.O. Northwood, *Materials Chemistry and Physics* 134 (2012) 484–492.
- [29] S. Stojadinovic, I. Belca, M. Tadic, B. Kasalica, Z. Nedic, Lj. Zekovic, *Journal of Electroanalytical Chemistry* 619–620 (2008) 125–130.
- [30] <http://physics.nist.gov/PhysRefData/ASD/lines.form.html>
- [31] S. Stojadinovic, R. Vasilic, M. Petkovic, Z. Nedic, B. Kasalica, I. Belca, Lj. Zekovic, *Electrochimica Acta* 55 (2010) 3857–3863.
- [32] J.M. Albella, I. Montero, J.M. Martinez-Duart, *Electrochimica Acta* 32 (1987) 255–258.

- [33] S. Ikonopisov, A. Girginov, M. Machkova, *Electrochimica Acta* 24 (1979) 451–456.
- [34] A.L. Yerokhin, L.O. Snizhko, N.L. Gurevina, A. Leyland, A. Pilkington, A. Matthews, *Journal of Physics D: Applied Physics* 36 (2003) 2110–2120.
- [35] M. Ivković, S. Jovičević, N. Konjević, *Spectrochim Acta Part B* 59 (2004) 591–605.
- [36] H.R. Griem, *Plasma Spectroscopy*, McGraw-Hill, New York, 1964.
- [37] G. Sundararajan, L. Rama Krishna, *Surface and Coatings Technology* 167 (2003) 269–277.
- [38] S. Moon, Y. Jeong, *Corrosion Science* 51 (2009) 1506–1512.
- [39] G. Lv, W. Gu, H. Chen, W. Feng, M.L. Khosa, L. Li, E. Niu, G. Zhang, S.Z. Yang, *Applied Surface Science* 253 (2006) 2947–2952.

Continuous wave laser for tailoring the photoluminescence of silicon nanoparticles produced by laser ablation in liquid

Dusan M. Popovic, Akihiro Kushima, Milena I. Bogdanovic, Jong Seo Chai, Becko Kasalica, Milan Trtica, Jelena Stasic, and Andrijana A. Zekic

Citation: *Journal of Applied Physics* **122**, 113107 (2017); doi: 10.1063/1.4990040

View online: <http://dx.doi.org/10.1063/1.4990040>

View Table of Contents: <http://aip.scitation.org/toc/jap/122/11>

Published by the [American Institute of Physics](#)

Articles you may be interested in

[High temperature degradation mechanism of a red phosphor, \$\text{CaAlSiN}_3\text{:Eu}\$ for solid-state lighting](#)

Journal of Applied Physics **122**, 113104 (2017); 10.1063/1.5003087

[Sensitized photoluminescence of erbium silicate synthesized on porous silicon framework](#)

Journal of Applied Physics **122**, 113103 (2017); 10.1063/1.4987035

[Measurement of sputtered beryllium yield and angular distribution during nanostructure growth in a helium plasma](#)

Journal of Applied Physics **122**, 113301 (2017); 10.1063/1.5002114

[Composite electrode with gate-tunable work function for optoelectronic devices](#)

Journal of Applied Physics **122**, 115501 (2017); 10.1063/1.4985863

[Oblique beams interference for mode selection in multimode silicon waveguides](#)

Journal of Applied Physics **122**, 113106 (2017); 10.1063/1.5003252

[Toroidal and magnetic Fano resonances in planar THz metamaterials](#)

Journal of Applied Physics **122**, 113105 (2017); 10.1063/1.5001246





Continuous wave laser for tailoring the photoluminescence of silicon nanoparticles produced by laser ablation in liquid

Dusan M. Popovic,^{1,a)} Akihiro Kushima,^{2,3,a)} Milena I. Bogdanovic,¹ Jong Seo Chai,⁴ Becko Kasalica,¹ Milan Trtica,⁵ Jelena Stasic,⁵ and Andrijana A. Zekic¹

¹University of Belgrade, Faculty of Physics, Studentski trg 12, 11001 Belgrade, Serbia

²Department of Nuclear Science and Engineering, Massachusetts Institute of Technology, Cambridge, Massachusetts 02139, USA

³Advanced Materials Processing and Analysis Center, Department of Materials Science and Engineering, University of Central Florida, Orlando, Florida 32816, USA

⁴School of Electronic and Electrical Engineering, College of Information and Communication Engineering, Sungkyunkwan University, Suwon 440-746, Korea

⁵Vinca Institute of Nuclear Sciences, University of Belgrade, PO Box 522, 11001 Belgrade, Serbia

(Received 13 June 2017; accepted 30 August 2017; published online 20 September 2017)

Silicon nanoparticles (SiNPs) are attracting attention for applications in various fields, from energy storage to bio-imaging. One of their main advantages is good photoluminescence (PL) properties combined with the relatively high bio-compatibility. Here, we fabricated SiNPs by the laser ablation of silicon single crystal in de-ionized water, employing simultaneously the picosecond pulse laser (150 ps, 1064 nm, 7 mJ/pulse) and a continuous wave (CW) laser (532 nm, 270 mW). TEM analysis (bright field TEM, HRTEM, HAADF, EDS) clearly shows that the introduction of the CW laser significantly increases the crystallinity of the produced nanoparticles, which may be crucial for many optical and electronic applications. The obtained SiNPs exhibit good blue photoluminescence properties, and the introduction of the CW laser into the fabrication process leads to the considerable increases in the photoluminescence. Additionally, we conducted a detailed analysis on the aging-time dependence and the excitation wavelength-dependent PL. The results indicate that the blue photoluminescence may be ascribed to quantum confinement effect, interface related states, and defect in the O-containing layer (shell) of the nanoparticles. We demonstrate that the relative share of these mechanisms in overall PL is significantly affected by the introduction of the CW laser to the pulse laser ablation and it may improve the applicability of the Si nanoparticles produced to a wide variety of fields. *Published by AIP Publishing.*

[<http://dx.doi.org/10.1063/1.4990040>]

I. INTRODUCTION

Silicon and silicon-based nanoparticles (SiNPs) have been attracting attention for more than two decades because of their broad field of potential applications, from engineering to biomedicine. In the field of energy storage, silicon is a promising high-capacity anode material for lithium-ion batteries.^{1,2} For instance, Wu *et al.* reported to have designed the Si-nanoparticle-based electrodes and to have achieved a high cycle stability by encapsulating them in a carbon tube structure.³ Single crystal silicon is widely used in electronics, but (due to the indirect bandgap) shows poor optical properties. The discovery of room-temperature visible PL from porous silicon in 1990,^{4,5} and later, from Si nanocrystals embedded in SiO₂,^{6,7} has increased interest in the optical properties of these materials. Despite such interests, which, in turn, resulted in a large number of publications analyzing these issues, there are still a considerable number of unresolved questions about the origin of the photoluminescence properties of SiNPs.

Nanomaterials that can circulate in the body have a great potential in diagnosing and treating various diseases.^{8–10} Their biocompatibility, coupled with the ability to be harmlessly eliminated from the body once they have completed the mission, is of crucial importance. Porous silicon nanoparticle is an alternative to quantum dots containing heavy metal (shown to be toxic in biological environments for *in vivo* use¹¹). Additionally, silicon is a common trace element in the human body, and a biodegradation product of porous silicon is naturally found in numerous tissues.¹¹ Photoluminescence properties are of great importance for the bio-application of Si-nanoparticles. For instance, the SiNPs are used as biological imaging agents.^{8,9,12} Additionally, surface functionalization of the SiNPs has attracted considerable attention.¹³ It is essential for their stabilization, targeting them to specific disease areas and allowing them to selectively bind to the cells or the bio-molecules present on the surface of the cells.¹⁴ Besides SiNPs, the silica (SiO₂) NPs have attracted attention as a promising material for biomedical applications.¹⁵ Although the low toxicity and good biocompatibility are usually recognized as comparative advantages of silicon and silica nanoparticles, the issue of toxicity of these nanomaterials raises some concerns.^{16,17}

^{a)}Authors to whom correspondence should be addressed: kushima@mit.edu and drdmpopovic@gmail.com

The technique of nanoparticle (and nanotubes) fabrication that has attracted attention is the pulsed laser ablation of solid target in liquid media (LAL).^{18–25} Some of the advantages of this technique are that it is simple, fast, and provides easy material handling since nanoparticles are produced directly in the liquid. Additionally, it reduces the contamination risk of the NPs produced. Production of the silicon NPs by LAL is widely reported, with silicon single crystal (pure or doped) used as the target.^{26–29} In most of the cases, the liquid used is de-ionized water, but other liquids—both inorganic and organic—are used as well.³⁰

Bulk single-crystal silicon exhibits poor PL properties due to its indirect band gap (around 1.1 eV). In contrast, due to the quantum confinement (QC) effect, the silicon nanocrystals below the QC size limit show good PL properties. This is ascribed to opening of the band gap and pushing it toward the direct one.³¹ The value of QC size limit varies up to 10 nm.^{32,33} When certain techniques are employed (*inter alia*, LAL) to produce the silicon nanocrystals, they became embedded in the silicon oxide matrix (SiO_x, $x < 2$). On the other hand, it has been reported that the Si/SiO₂ interface (the surface states), besides the QC effect, may play an important role in PL properties.⁷ As far as the SiNPs produced by LAL are concerned, the PL bands could be placed in the whole visible region of the spectrum. The PL band positions and intensities depend on the LAL parameters and the sample history.^{34–36} And there is a noticeable discrepancy in the PL data obtained in different experiments reported in the literature, even when similar LAL parameters are used.

In this paper, we report a fabrication procedure of the blue luminescent SiNPs using picosecond pulsed laser ablation of Si single crystal in de-ionized water (150 ps, 1064 nm, 7 mJ/pulse) with an additional continuous wave (CW) green laser (532 nm, 270 mW) during and for 15 min immediately prior to the ablation. Detailed transmission electron microscopy (TEM) analysis was performed to correlate the photoluminescence (PL) properties and the structures of the SiNPs, focusing on the impact of employing the CW laser on the PL properties and the crystallinity of the SiNPs produced.

II. EXPERIMENTAL

We synthesized SiNPs by pulsed laser ablation in liquid using square-shaped plates of Si single crystal (5.00 mm × 5.00 mm × 0.69 mm in size) as a target. To determine crystal orientation of Si substrate, an X-ray diffraction (XRD) was performed using a Rigaku Ultima IV diffractometer in Bragg-Brentano configuration with Ni-filtered CuK_α radiation ($\lambda = 1.54178 \text{ \AA}$). The orientation of the Si substrate was determined to be $\langle 100 \rangle$. The X-ray powder diffraction (XRPD) patterns of the samples were collected on Rigaku SmartLab 3 kW automatic X-ray diffractometer in 25–50 range of 2θ (°). During the ablation, targets were fixed on the bottom of the vessel. The vessel was filled with 5 ml of de-ionized water (DIW). The water layer thickness was kept to about 3 mm during the experiment. There were splashes during the laser ablation, and the

laser pulses were followed by noticeable bubbles in the DIW. A shield was placed axially around the vessel to reduce splashes around the setup. The target was placed 3 mm under the focal plane of the lens (focal length $f=171 \text{ mm}$).

The picosecond pulse Nd:YAG laser was employed at wavelengths of 1064 nm. Its pulse duration was 150 ps and its repetition rate was 10 Hz. It had a pulse energy of 7 mJ/pulse (laser fluence 4.4 J cm^{-2}) and the laser exposure time was 15 min. The additional continuous wave (CW) green laser (270 mW, 532 nm, laser power density 3.78 W cm^{-2}) was applied during the LAL process and for 15 min prior to the application of the pulse laser. One of the impacts of introducing the CW laser is the increase of the target temperature. Increment in temperature of the silicon substrate produced with CW laser stabilized within 15 min. The centers of the laser spots, both continuous and pulsed, were placed at a fixed position in the center of the silicon substrate. The detail of the experimental setup is presented elsewhere.³⁷

Photoluminescence measurements of SiNPs in DIW were carried out using Horiba Jobin Yvon, FL3-22 spectrofluorometer. A good quality scan was obtained by 450W-xenon lamp in FL3 with a single excitation monochromator. The range of excitation wavelength was 300–360 nm, and the integration time was 0.5 s. The PL measurements were performed using the solution obtained by LAL shortly after the production and then in certain intervals. Transmission electron microscopy analysis was performed at the Center of Materials Science and Engineering in Massachusetts Institute of Technology using JEOL 2010F operated at 200 kV acceleration voltage. The TEM is equipped with energy dispersive X-ray spectrometer (Oxford Instruments). The EDS analysis (including spectrum, line scan profile, and elemental quantification) was conducted in the scanning transmission electron microscopy mode. Dynamic light scattering (DLS) analyses were carried out using Malvern Zetasizer Nano ZS.

III. RESULTS AND DISCUSSION

The photoluminescence spectra (excitation 300 nm) of SiNPs produced by pulsed laser ablation with and without applying the additional continuous wave (CW) laser are shown in Fig. 1. The PL spectrum shows a broad band peaked at 410 nm and 427 nm, and the red-shift of the PL peak is about 17 nm. Additionally, a considerable increase in PL intensity (the PL peak intensity and peak height increase about 50% and 100%, respectively) was observed as a result of introducing the CW laser during the ablation.

To investigate the PL mechanism of the SiNPs samples produce in this work, we performed the transmission electron microscopy (TEM) analysis. The solution obtained by the LAL was dropped onto the silicon nitride TEM window grid (Norcada) and dried under atmospheric pressure at room temperature. The bright field TEM, an electron diffraction pattern, a high resolution TEM, high – angle annular dark field (HAADF) image, and energy – dispersive X – ray spectroscopy (EDS) measurements were carried out to determine

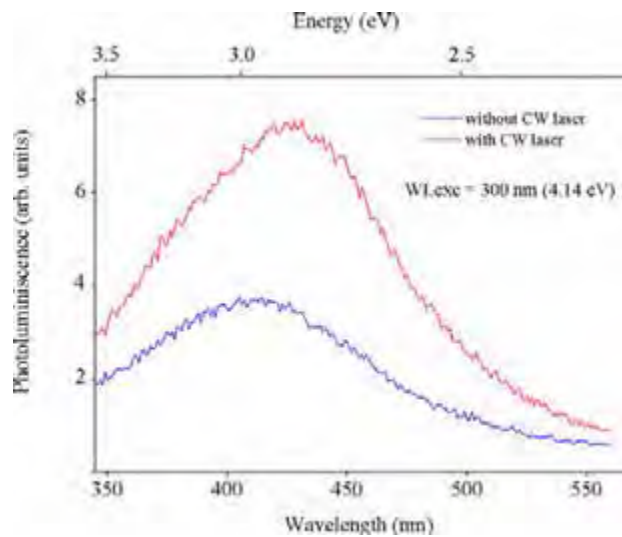


FIG. 1. The photoluminescence spectra (excitation 300 nm) of SiNPs produced by pulsed laser ablation with and without applying the CW laser.

the crystalline structure and the chemical composition of the SiNPs.

Figure 2 shows the results of TEM analysis of SiNPs produced by LAL without the additional CW laser. Figure 2(a) shows the TEM image of the SiNP with the diameter ~ 200 nm. The electron diffraction pattern (EDP) shows amorphous halo with weak crystalline spots [Fig. 2(b)]. The high resolution (HR) TEM images revealed the existence of silicon nanocrystals embedded in the amorphous matrix [Fig. 2(c)]. These nanocrystals had no regular shape and were about 5–10 nm in size. Figure 2(d) is a HAADF image of the same SiNP. The elemental composition analysis by EDS measurement was performed along the solid line in the figure, and the distribution of Si and O is shown in Fig. 2(e). Figure 2(f) depicts EDS spectra measured at the numbered squares in Fig. 2(d). The O peak is clearly seen at the surface, but reduces at the inner regions. The atomic ratio of Si and O at regions (1)–(4) is shown in Fig. 2(g). These EDS analysis results show that the particle consists mostly of

silicon, and only a small portion at the surface contains more significant amount of oxygen. It also revealed the oxygen content was higher towards the particle surface indicating the Si-rich core of the particle was coated by the O-containing layer. It is worth noting that the Si:O ratio in this layer is much higher than that of silicon dioxide [Fig. 2(g)]. Because the size of the silicon nanocrystals embedded in the amorphous matrix is below the QC effect size limit, the QC effect is expected to contribute to the PL of the SiNPs sample produced without the additional CW laser.

The results of TEM analysis of the SiNPs produced by LAL with the additional CW laser are shown in Fig. 3. The TEM micrograph [Fig. 3(a)] and the EDP [Fig. 3(b)] indicate the particle was polycrystalline silicon, in contrast to amorphous structure observed for particles produced without CW laser. The HRTEM image of the particle shows a clear Si lattice structure. The size of these nanocrystals was far above the QC effect size limit. The TEM analysis for few other particles of the same sample showed the same trend. Although some nanocrystals below the QC effect size limit were found in the particles, they are few in number. Therefore, QC effect may not play a significant role in the PL property. HAADF image of the particle is shown in Fig. 3(d), and elemental distribution along the solid line and the EDS spectra taken from the squared regions (1)–(4) are shown in Figs. 3(e) and 3(f), respectively. Similar to the SiNPs produced without the CW laser, the oxygen peak is high at the particle surface and low at the inner regions. The atomic composition ratio of Si and O at the regions (1)–(4) as shown in Fig. 3(g) reveals the O is concentrated on the surface (O-containing layer), but the amount is less compared to the SiNPs produced without the CW laser.

Comparing Figs. 2 and 3, it is obvious that the introduction of the additional CW laser in the LAL process leads to (a) a significant increase in the silicon nanocrystal size (and consequently to increasing crystallinity of the particles produced) and (b) a decrease in the amount of oxygen, both in “the bulk” and in the O-containing layer of SiNP. The exposure time and the power of the CW laser are expected to

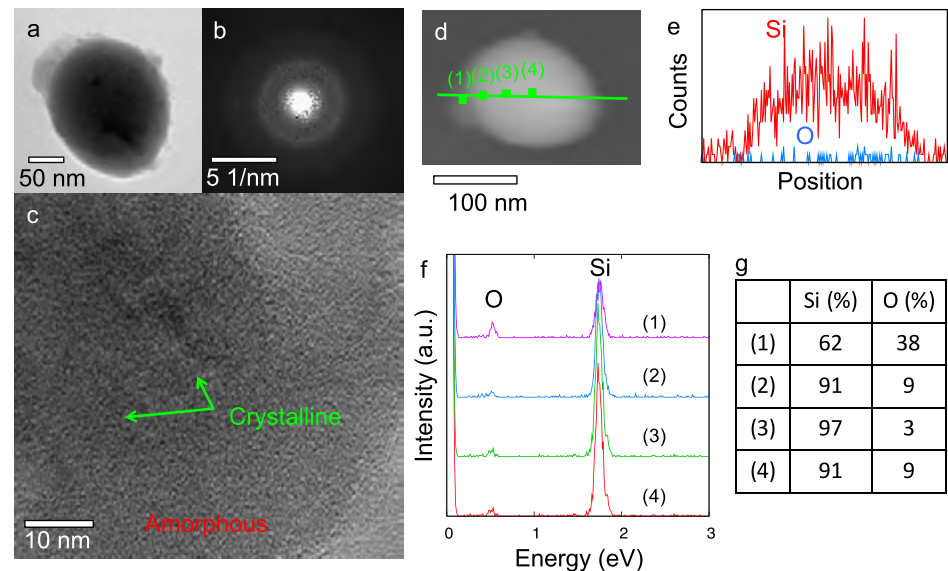


FIG. 2. TEM analysis of SiNPs produced by LAL without the additional CW laser: (a) bright field TEM image, (b) electron diffraction pattern, (c) high resolution TEM image, (d) HAADF image, (e) EDS line scan profile from the solid line in (d), (f) EDS spectra obtained from spots 1–4 in (d), and (g) Si:O ratio in atomic %.

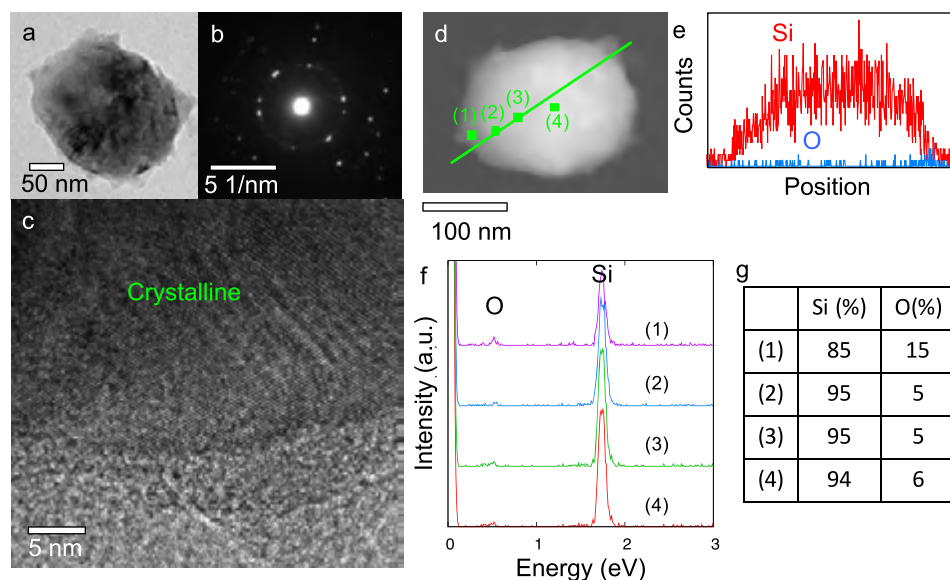


FIG. 3. TEM analysis of SiNPs produced by LAL with the additional CW laser: (a) bright field TEM image, (b) electron diffraction pattern, (c) high resolution TEM image, (d) HAADF image, (e) EDS line scan profile from the solid line in (d), (f) EDS spectra obtained from spots 1–4 in (d), and (g) Si:O ratio in atomic %.

affect the crystallinity of the final product. However, our main purpose in this work is to demonstrate the possibility of introducing a CW laser for designing the structure of the SiNPs in LAL process.

The X-ray powder diffraction (XRPD) patterns of dried SiNPs samples obtained with and without application of CW laser are presented in Fig. 4. The diffraction peaks of both samples coincided with those of silicon (ICCD PDF-2 2016) and no other phases were detected, including SiO_2 . Its absence of diffraction patterns confirms either no oxidation of the particles, or the oxidation of the surface in the form of thin amorphous layer that is below the XRPD detection threshold. The XRPD patterns reveal an evident increase in crystallinity of the SiNPs sample due to introducing the CW laser in the LAL fabrication process.

In general, the particle size distribution can influence on the photoluminescence spectra of SiNPs (related to the total surface of the SiNPs in the solution, etc.). Figure 5 shows the

results of dynamic light scattering (DLS) analysis of SiNPs produced by LAL without and with the additional CW laser. Both distributions are broad and skewed, following the log-normal distribution. It shows that the application of the additional CW laser slightly changed the SiNPs' size distribution, shifting its maximum to smaller values. However, the particle size distributions are almost identical, indicating the considerable increase in photoluminescence intensity from Fig. 1 is not caused by difference in the size distribution of the analyzed SiNPs samples.

It is widely accepted that, in addition to the QC effect, the defects at the interfaces between the silicon nanocrystal below the QC effect size limit and the surrounding matrix greatly affect the PL properties. The well-known non-radiative defects are the Pb centers, the trivalent silicon atoms at the crystalline silicon/silicon dioxide interface.^{38,39} Some of the excitons (electron-hole pairs) in nanoparticles are trapped at these non-radiative defects, decreasing the PL intensity. The radiative interface defects (luminescent recombination centers) can be present at the interfaces as well. Therefore, a

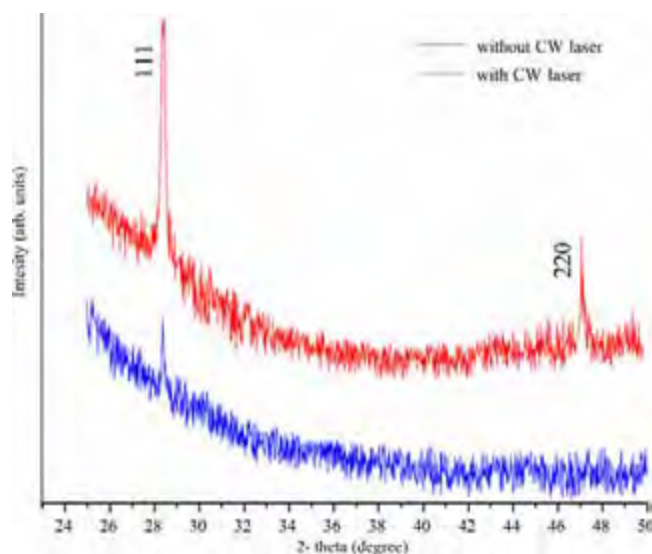


FIG. 4. The X-ray powder diffraction (XRPD) patterns of SiNPs produced by pulsed laser ablation without and with applying the CW laser.

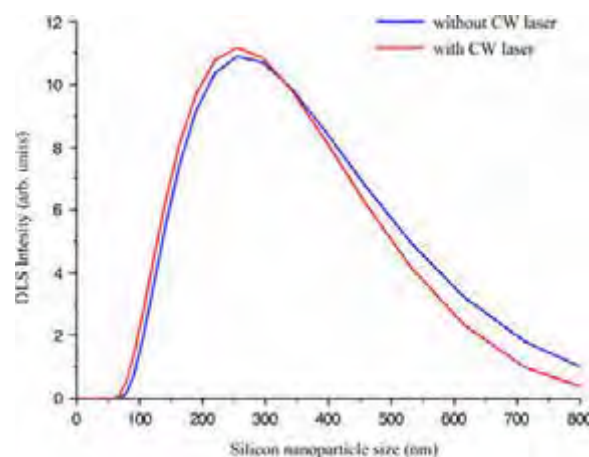


FIG. 5. The particle size distribution obtained by dynamic light scattering (DLS) for SiNPs produced by LAL without and with additional CW laser.

decrease in the concentration of the non-radiative defects, coupled with an increase in the concentration of the radiative centers, may increase the photoluminescence. Some of the experimental results and models reported in the literature support the assumption that the mechanism responsible for the efficient PL from silicon nanocrystals should be assigned to the inhibition of nonradiative channels rather than to the enhancement of the radiative ones.⁴⁰ It is reported that the analysis of interface defects is mostly related to Si/SiO₂ interface, but these defects are also used in the analysis of the PL properties of Si nanoparticles embedded in SiO_x ($x < 2$) matrix.⁴¹ The interface defects mentioned above are oxygen-related – both the radiative and the non-radiative ones. On the other hand, the amorphous core of the SiNPs analyzed here, in which silicon nanocrystals are embedded [Figs. 2(c) and 3(c)], contains less than 10% of oxygen [Figs. 2(g) and 3(g)]. This makes the evaluation of the role of the interface defects at the PL properties more complex.

It has been reported that the amorphous silica exhibits the luminescence properties, due to the existence of oxygen deficient centers.⁴² These luminescent defects are observed in irradiated or oxygen-deficient silica, both in bulk and in porous SiO_x films with high specific surface area.^{43,44} The blue and the UV PL bands from Si/SiO₂ core-shell nanoparticle are attributed to these defects in amorphous silica.⁴⁵ The O-containing shell (O-containing layer) from Figs. 2(e)–2(g) and 3(e)–3(g), may be considered as region of oxygen-deficient amorphous silica. The oxygen deficit was more pronounced in the SiNP sample produced with the additional CW laser [Fig. 3(g)], than for the sample produced without it [Fig. 2(g)]. We speculate that the lower content of the oxygen in the SiNP's O-containing layer may signify a higher concentration of oxygen deficient centers, which lead to an increase in the photoluminescence originating from oxygen-related defects in this layer. Nevertheless, lower content of oxygen in SiO_x does not necessarily lead to an increase in the concentration of oxygen deficient centers; for instance, some oxygen can occupy interstitial sites, exhibiting the luminescence properties.⁴⁶ It is worth noting that, there are other PL active defects in amorphous silica in addition to the oxygen-related defects.

From the results and analysis presented above, the PL properties of the SiNPs analyzed in this paper may be related to (a) QC effect in Si nanocrystals embedded in the amorphous matrix, (b) interface related states, and (c) defects in O-containing layer of the SiNPs. We emphasize here that a relative contribution of these mechanisms in the overall PL is different for the SiNP samples fabricated with and without the additional CW laser. Such difference may be one of the reasons for the red-shift of the PL peak shown in Fig. 1. In some cases (depending on the fabrication of the NPs, sample history, etc.), the PL peaks of silicon-based nanomaterials originated from silicon nanocrystals and amorphous SiO₂ nanoparticles are both broad and close to each other (compare, for instance, previously reported PL data^{35,47}). Therefore, the lower concentration of the oxygen deficient centers in O-containing layer of SiNPs produced without the CW laser (because of the higher oxygen contents) and coupled with the low presence of the QC effect in Si

nanocrystals for the sample produced with the CW laser (because of its size) may cause a shift in the PL peak position (Fig. 1). Some of the reported hypotheses concerning the origin of the red-shift in the PL peak deal with an increase in the sizes of the Si-crystallites (as expected from the QC effects)⁴⁰ and oxidation (related to the recombination involving a trapped electron or exciton).³² Such effects may appear in the NP samples analyzed here, because the introduction of the CW laser in the LAL process increased the size of the Si nanocrystal embedded in the amorphous matrix.

To analyze further the PL properties of the SiNPs and the impact of the CW laser introduction in the LAL process, we performed the excitation wavelength-dependent PL measurements two months after the LAL (Fig. 6). The “cut off” narrow peaks at 331 nm, 356 nm, 383 nm, and 408 nm on Figs. 6(a) and 6(b) are Raman peaks of DIW.⁴⁸ It can be observed from Fig. 6(a) that, for the SiNPs produced without additional CW laser, the PL peak exhibited the red-shift with an increase in the excitation wavelength. When the excitation wavelength increased from 300 to 360 nm, the PL peak exhibited the red-shift of about 20 nm. The wavelength-dependent PL measurements, for the SiNPs produced with additional CW laser, showed that the peak positions slightly depended on the excitation wavelength (the PL peak position for 360 nm-excitation is red-shifted for about 9 nm compared to the PL position for 300 nm-excitation), with clearly noticeable exception for the excitation of 320 nm, where the PL peak position exhibited a drastic blue-shift [Fig. 6(c)].

The excitation wavelength-dependent PL measurements for the silicon nanoparticles have not been extensively studied, and this complex issue remains a subject of controversy. It has been reported that when the excitation wavelength shifts to the red, the visible PL peak position exhibits the red-shift.⁴⁹ Some authors propose, based on quantum confinement theory, that the absence of the red-shift in the PL peak position with the increase in the excitation wavelength is the evidence proving that the band-to-band transition in the silicon nanocrystals ought to be excluded as the origin of the blue PL.⁴¹

In this paper, we proposed several mechanisms contributing to the PL properties of the analyzed SiNPs. Such assumption could be employed to enlighten further the excitation wavelength-dependent PL in Figs. 6(a) and 6(b). For the SiNPs produced without the additional CW, the red-shift of the PL peak position with the increase in the excitation wavelength supports (in accordance with the QC theory) the assumption that the band-to-band transition in the silicon nanocrystals has the significant role in the PL. The weak excitation wavelength-dependent shift (with the exception for apart from the excitation of 320 nm) of the PL peak position for the SiNPs samples produced with the additional CW laser [Figs. 6(b) and (c)] is in a good accordance with the fact that the sizes of the majority of nanocrystals embedded in the amorphous matrix are far above the QC effect size limit. We assume here that the drastic blue-shift of PL peak position for 320 nm – excitation wavelength [Fig. 6(c)] is related to the defects in the SiO_x shells of the SiNPs. For visible luminescence in nanosilica, Vaccaro *et al.* reported the electronic energy level scheme for silica nanoparticles.⁵⁰ If we assume

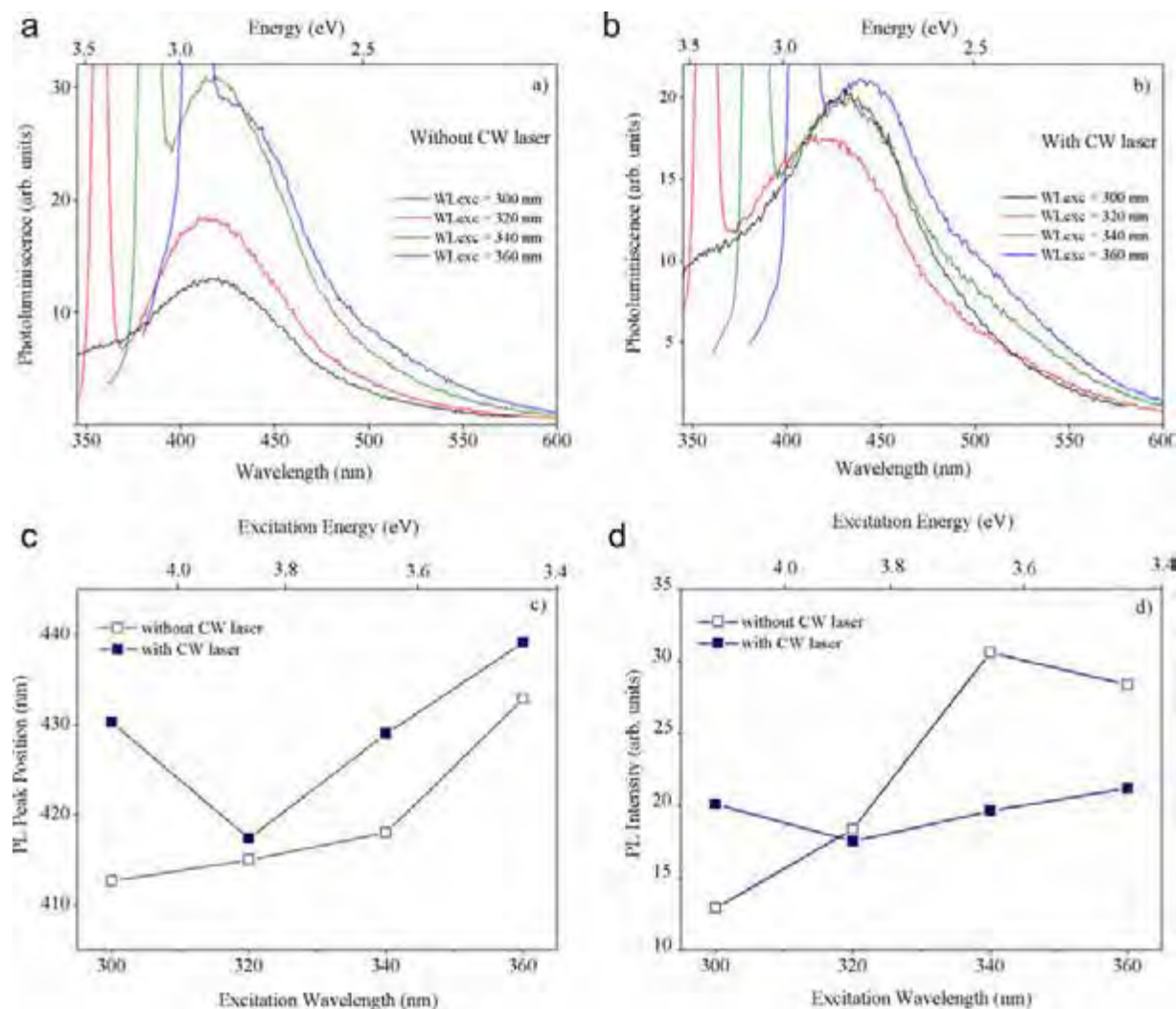


FIG. 6. Excitation wavelength-dependent PL measurements after a two-months aging: (a) spectra of SiNPs produced without CW laser, (b) spectra of SiNPs produced with CW laser, (c) PL peak positions for SiNPs produced with and without CW laser, and (d) PL peak intensities for SiNPs produced with and without CW laser.

that there is a similar energy level scheme for O-containing layer in the SiNPs, the drastic blue-shift of PL peak position for excitation of 320 nm might be explained. Namely, energy of the 320 nm – excitation (3.88 eV) may correspond to the energy gap between the energy states. Consequently, the creation of the excitons is disabled, and the PL excitation pathway is ruined. Therefore, the mechanism related to the defects in the O-containing layer does not contribute to the PL. Due to the exclusion of this PL mechanism for the SiNPs produced with the additional CW laser, the overall effect of the PL was closer to the one for the SiNPs produced without the CW laser. This explanation agrees with our measurement that both, the PL peak position and the intensities for the excitation of 320 nm, are close for both SiNPs samples [Figs. 6(c) and 6(d)]. This supports our previous assumption that the PL properties of the SiNPs analyzed here originated from multiple contributing mechanisms, whose relative share depend on the parameters of the production (in our experiments that would be the additional CW laser). This may open the possibility of using the CW laser in the LAL process as a tool for tailoring the PL properties of the silicon-based nanoparticles. The wavelength-dependent PL peak intensity [Fig. 6(d)] indicates

that the enhancement of the PL peak intensity due to the CW laser employment occurred only for the excitation of 300 nm. This did not occur for the lower PL excitation energy.

The aging-time dependence of the PL spectra (for the excitation at 300 nm) from the SiNPs produced without and with the CW laser is presented in Fig. 7. A noticeable increase in photoluminescence occurred for both samples. The increase was faster for the sample produced without the CW laser. After one month of aging, the PL peak intensity of the samples fabricated with and without the CW laser increased for about 115% and 120%, respectively; after three months of aging, the increase was about 190% and 420%, respectively. Although the PL intensity of the SiNPs fabricated with the CW laser was initially higher than that without the CW laser, the three months of aging reduced the difference to less than 10%.

The PL peak position for the SiNPs produced without the CW laser, exhibited the red-shift due to aging [Fig. 7(a)]; for three months of aging the PL peak shifted for about 7 nm (54.0 meV). The aging-time dependence of the PL peak for the SiNPs produced with the CW laser [Fig. 7(b)] exhibited the red-shift during the first month of aging (about

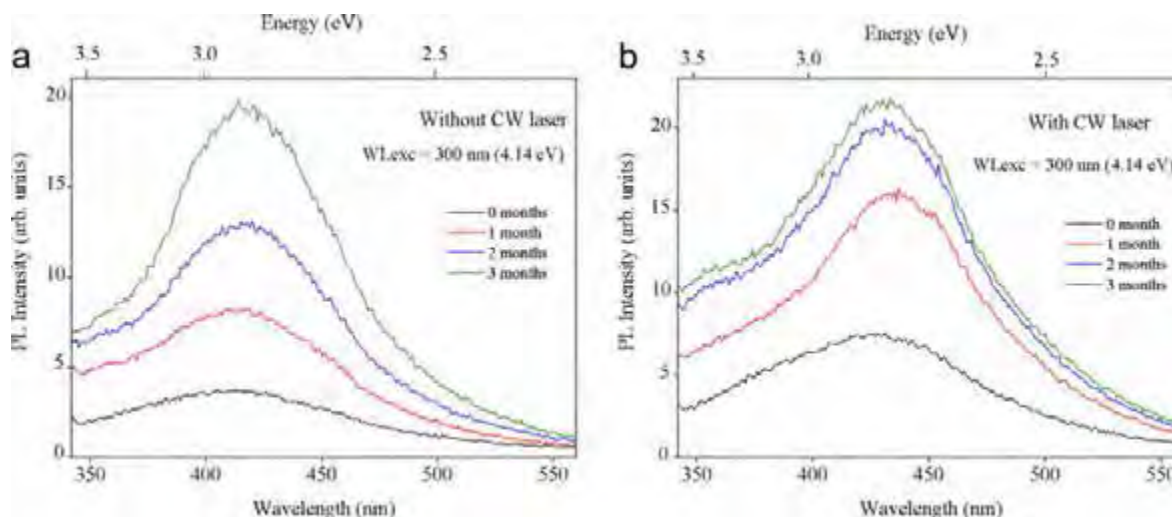


FIG. 7. The aging-time dependence of the PL spectra (excitation 300 nm) for SiNPs produced: (a) without and (b) with additional CW laser.

60.0 meV), followed by the blue-shifting during the next two months (about 35.4 meV).

The aging enhancement of the blue PL reported here agrees well with other literatures. Svrcek *et al.* ascribed such enhancement to the oxide passivation and defect relaxation on the surface of the Si nanocrystal; no aging-induced shift of blue PL peak position was reported.³⁶ Yang *et al.* assumed that the number of Pb centers should decrease gradually during aging, due to the passivation of Si dangling bonds by oxygen atoms.⁴¹ The analysis of the aging-time dependence of the PL spectra we presented here may have more complexity due to the O-containing layer of the SiNPs [Figs. 2(d) and 3(d)]. In general, the presence of oxygen may have a significant impact on the broad range of the PL properties of the nanomaterials. For instance, the investigation of the role of oxygen-containing groups in the fluorescence of nanodiamonds is reported.⁵¹

Pulse laser ablation of solid materials in vacuum or gas was developed soon after the first laser became available. Due to a promising potential in material processing (thin solid film and nanoparticle fabrication, surface cleaning, etc.), this technique has attracted researchers' attention. In principle, pulse laser ablation of solid materials in liquid is a modification of this technique, but the pivotal difference between them is that liquid confines the plasma plume produced due to ablation. Consequently, this confining role of liquid affects the stages of the LAL. Despite the extensive investigations, the mechanism of pulse laser ablation in water remains unclear, especially for silicon.

The absorption of laser pulses by the single crystal target (photon-carrier interaction) is followed by energy transfer to the crystal lattice (carrier-phonon interaction). Immediately after the laser ablation, plasma plume from the solid target will be generated over the laser spot (laser-induced plasma). When nanosecond pulse laser is employed, the laser-induced plasma expands adiabatically,⁵² generating a shock wave under the confinement of the liquid.^{20,53,54} The shock wave induces the pressure increase in the laser-induced plasma (plasma-induced pressure). The increase in the pressure induces an additional increase in temperature of the laser-induced

plasma. The temperature and pressure in the plume rapidly grow to maximal values. When these values start to increase, the condensation of the plasma leads to the formation of parent phase clusters. If these clusters reach a critical size, the crystal starts to grow. For sub-nanosecond-pulse lasers, however, the mechanism of ablation is different and there is no consensus on this issue. The role of the pulse duration depends on the electron cooling time (electron-phonon coupling constant) of the material.⁵⁵ When the picoseconds pulse laser is employed in LAL process, thermal effects or a solid-vapor transition may occur depending on the pulse duration. Also, the pulse duration affects the ablation thresholds of dielectric materials.^{55,56} The high repetition rate of ps lasers is advantageous for enhancing the production of nanoparticles.⁵² It is reported that at the same pulse fluence, nanoparticle productivity is about three times higher for picosecond laser ablation compared with femtosecond lasers, due to the higher repetition rate.⁵⁷ Some recent reports have demonstrated that, compared with nanosecond and femtosecond lasers, the picosecond lasers are superior to improve the production of NPs fabricated by LAL.^{58,59} A theoretical analysis shows that for laser pulse duration of hundreds of picoseconds (150 ps in our experiment), a trivial fragmentation seems to be the only relevant ablation mechanism,⁶⁰ which is in agreement with the reported simulations of laser ablation in silicon.⁶¹ This is in contradiction to the predictions of the widely accepted phase explosion model.⁶²

The issues concerning the way in which the application of CW laser during the LAL affects the properties of the fabricated SiNPs is quite complex due to at least two reasons. First, the application of CW laser may affect more than one stages of the LAL process, which makes the analysis and interpretation of experimental results complex. Second, to the best of our knowledge, there is a lack of theoretical analyses concerning this issue. Enhanced silicon absorption under laser irradiation has been reported.⁶³⁻⁶⁵ Two processes affect this phenomenon – the free-carrier absorption and thermal absorption enhancement.^{66,67} Therefore, introducing the CW laser in LAL may affect the laser absorption by silicon target, and, consequently, the ablation process. This may indirectly affect

the important thermodynamic parameters of the laser-induced plasma (density of species, temperature, and pressure). If fragmentation is the only mechanism, introducing the CW laser in the ablation process could affect it, but analysis of this issue requires a comprehensive theoretical approach. The issues concerning the impact of introducing the CW laser in LAL process on the oxygen presence in the nanoparticles produced by LAL remain unclear. For nanosecond laser ablation in water, Yang reported four kinds of chemical reactions taking place in the laser-induced plasma and the interface between the liquid and the laser-induced plasma.²⁰ Out of the four, three chemical reactions are simultaneously involved two species that result from the solid target and the confining liquid, respectively. We showed here that introducing the CW laser into the ablation process changed the chemical composition of the silicon oxide matrix of the produced nanoparticles (the amount of oxygen). This might indicate that the CW laser has an impact on the laser induced plasma (and, consequently, on the plasma-induced plasma created at the plasma-liquid interface²⁰). On the other hand, we speculate that the O-containing layer of SiNPs is primarily formed when the particles enter from the plume into the de-ionized water.

IV. CONCLUSION

In summary, we have analyzed blue photoluminescence and crystallinity of silicon nanoparticles produced by pulsed laser ablation of silicon single crystal in de-ionized water. Simultaneously with the picosecond pulse laser, we employed the continuous wave laser during the production.

It is clearly demonstrated here that introducing the continuous wave laser in the ablation process impacts the properties of the produced silicon nanoparticles and leads to (1) a significant increase in crystallinity (increases the size of silicon nanocrystals embedded in amorphous matrix), (2) an increase in the photoluminescence for 300 nm- excitation, and (3) a slight decrease in the amount of oxygen.

Additionally, we demonstrated that introduction of the continuous wave laser affects both the excitation-wavelength and aging-time dependence photoluminescence properties of the silicon nanoparticles. This is interpreted as the impact of the continuous wave laser during the fabrication process on the relative share of the different contributing photoluminescence mechanisms (related to quantum confinement effect, interface related states, etc.). Therefore, the introduction of the continuous wave laser into the pulse laser ablation process has a potential as a tool for tailoring the properties of silicon nanoparticles produced.

ACKNOWLEDGMENTS

This work was supported partially by the Ministry of Education, Science and Technological Development of the Republic of Serbia (Grant No. 172019).

¹A. Verma and F. Stellacci, "Effect of surface properties on nanoparticle-cell interactions," *Small* **6**(1), 12–21 (2010).

²J. K. Lee, K. B. Smith, C. M. Hayner, and H. H. Kung, "Silicon nanoparticles-graphene paper composites for Li ion battery anodes," *Chem. Commun.* **46**(12), 2025–2027 (2010).

³H. Wu, G. Zheng, N. Liu, T. J. Carney, Y. Yang, and Y. Cui, "Engineering empty space between Si nanoparticles for lithium-ion battery anodes," *Nano Lett.* **12**(2), 904–909 (2012).

⁴L. T. Canham, "Silicon quantum wire array fabrication by electrochemical and chemical dissolution of wafers," *Appl. Phys. Lett.* **57**(10), 1046–1048 (1990).

⁵V. Lehmann and U. Gösele, "Porous silicon formation: A quantum wire effect," *Appl. Phys. Lett.* **58**(8), 856–858 (1991).

⁶B. Krummheuer, V. M. Axt, and T. Kuhn, "Theory of pure dephasing and the resulting absorption line shape in semiconductor quantum dots," *Phys. Rev. B* **65**(19), 195313 (2002).

⁷G. Hadjisavvas and P. C. Kelires, "Structure and energetics of Si nanocrystals embedded in a-SiO₂," *Phys. Rev. Lett.* **93**(22), 226104 (2004).

⁸C. Caltagirone, A. Bettoschi, A. Garau, and R. Montis, "Silica-based nanoparticles: A versatile tool for the development of efficient imaging agents," *Chem. Soc. Rev.* **44**(14), 4645–4671 (2015).

⁹J.-H. Park, L. Gu, G. von Maltzahn, E. Ruoslahti, S. N. Bhatia, and M. J. Sailor, "Biodegradable luminescent porous silicon nanoparticles for in vivo applications," *Nat. Mater.* **8**(4), 331–336 (2009).

¹⁰J.-H. Lee, Y.-M. Huh, Y. Jun, J. Seo, J. Jang, H.-T. Song, S. Kim, E.-J. Cho, H.-G. Yoon, J.-S. Suh *et al.*, "Artificially engineered magnetic nanoparticles for ultra-sensitive molecular imaging," *Nat. Med.* **13**(1), 95–99 (2007).

¹¹A. M. Derfus, W. C. W. Chan, and S. N. Bhatia, "Probing the cytotoxicity of semiconductor quantum dots," *Nano Lett.* **4**(1), 11–18 (2004).

¹²C. M. Hessel, M. R. Rasch, J. L. Hueso, B. W. Goodfellow, V. A. Akhavan, P. Puvanakrishnan, J. W. Tunnel, and B. A. Korgel, "Alkyl passivation and amphiphilic polymer coating of silicon nanocrystals for diagnostic imaging," *Small* **6**(18), 2026–2034 (2010).

¹³F. Erogbogbo, K.-T. Yong, I. Roy, R. Hu, W.-C. Law, W. Zhao, H. Ding, F. Wu, R. Kumar, M. T. Swihart *et al.*, "In vivo targeted cancer imaging, sentinel lymph node mapping and multi-channel imaging with biocompatible silicon nanocrystals," *ACS Nano* **5**(1), 413–423 (2011).

¹⁴J. H. Ahire, I. Chambrier, A. Mueller, Y. Bao, and Y. Chao, "Synthesis of D-Mannose capped silicon nanoparticles and their interactions with MCF-7 human breast cancerous cells," *ACS Appl. Mater. Interfaces* **5**(15), 7384–7391 (2013).

¹⁵M. A. Malvindi, V. Brunetti, G. Vecchio, A. Galeone, R. Cingolani, and P. P. Pompa, "SiO₂ nanoparticles biocompatibility and their potential for gene delivery and silencing," *Nanoscale* **4**(2), 486–495 (2012).

¹⁶K. Fujoka, S. Hanada, F. Kanaya, A. Hoshino, K. Sato, S. Yokosuka, Y. Takigami, K. Hirakuri, A. Shiohara, R. D. Tilley *et al.*, "Toxicity test: Fluorescent silicon nanoparticles," *J. Phys. Conf. Ser.* **304**(1), 012042 (2011).

¹⁷T. J. Brunner, P. Wick, P. Manser, P. Spohn, R. N. Grass, L. K. Limbach, A. Bruinink, and W. J. Stark, "In vitro cytotoxicity of oxide nanoparticles: Comparison to asbestos, silica, and the effect of particle solubility," *Environ. Sci. Technol.* **40**(14), 4374–4381 (2006).

¹⁸G.-W. Yang, J.-B. Wang, and Q.-X. Liu, "Preparation of nano-crystalline diamonds using pulsed laser induced reactive quenching," *J. Phys. Condens. Matter.* **10**(35), 7923 (1998).

¹⁹W. T. Nichols, T. Sasaki, and N. Koshizaki, "Laser ablation of a platinum target in water. I. ablation mechanisms," *J. Appl. Phys.* **100**(11), 114911–114916 (2006).

²⁰G. W. Yang, "Laser ablation in liquids: Applications in the synthesis of nanocrystals," *Prog. Mater. Sci.* **52**(4), 648–698 (2007).

²¹S. Petersen and S. Barcikowski, "In situ bioconjugation: Single step approach to tailored nanoparticle-bioconjugates by ultrashort pulsed laser ablation," *Adv. Funct. Mater.* **19**(8), 1167–1172 (2009).

²²P. Liu, Y. Liang, H. B. Li, J. Xiao, T. He, and G. W. Yang, "Violet-blue photoluminescence from Si nanoparticles with zinc-blende structure synthesized by laser ablation in liquids," *AIP Adv.* **3**(2), 022127 (2013).

²³A. De Bonis, T. Lovaglio, A. Galasso, A. Santagata, and R. Teghil, "Iron and iron oxide nanoparticles obtained by ultra-short laser ablation in liquid," *Appl. Surf. Sci.* **353**, 433–438 (2015).

²⁴J. H. Yan, P. Liu, Z. Y. Lin, H. Wang, H. J. Chen, C. X. Wang, and G. W. Yang, "Magnetically induced forward scattering at visible wavelengths in silicon nanosphere oligomers," *Nat. Commun.* **6**, 7042 (2015).

²⁵P. Liu, Y. L. Cao, C. X. Wang, X. Y. Chen, and G. W. Yang, "Micro- and nanocubes of carbon with C8-like and blue luminescence," *Nano Lett.* **8**(8), 2570–2575 (2008).

²⁶R. Intartaglia, K. Bagga, and F. Brandi, "Study on the productivity of silicon nanoparticles by picosecond laser ablation in water: Towards gram per hour yield," *Opt. Express* **22**(3), 3117–3127 (2014).

- ²⁷D. Rioux, M. Laferrière, A. Douplik, D. Shah, L. Lilge, A. V. Kabashin, and M. M. Meunier, "Silicon nanoparticles produced by femtosecond laser ablation in water as novel contamination-free photosensitizers," *J. Biomed. Opt.* **14**(2), 021010–021010-5 (2009).
- ²⁸D. M. Popovic, J. S. Chai, A. A. Zekic, M. Trtica, M. Momcilovic, and S. Maletic, "Synthesis of silicon-based nanoparticles by 10.6 Mm nanosecond CO₂ laser ablation in liquid," *Laser Phys. Lett.* **10**(2), 026001 (2013).
- ²⁹V. Svrcek and M. Kondo, "Blue light emitting silicon nanocrystals prepared by laser ablation of doped Si wafers in water," *J. Laser Micro/Nanoeng.* **5**, 103–108 (2010).
- ³⁰P. A. Perminov, I. O. Dzhun, A. A. Ezhov, S. V. Zaboltnov, L. A. Golovan, G. D. Ivlev, E. I. Gatskevich, V. L. Malevich, and P. K. Kashkarov, "Creation of silicon nanocrystals using the laser ablation in liquid," *Laser Phys.* **21**(4), 801 (2011).
- ³¹B. Delley and E. F. Steigmeier, "Quantum confinement in Si nanocrystals," *Phys. Rev. B* **47**(3), 1397–1400 (1993).
- ³²M. V. Wolkov, J. Jorne, P. M. Fauchet, G. Allan, and C. Delerue, "Electronic states and luminescence in porous silicon quantum dots: The role of oxygen," *Phys. Rev. Lett.* **82**(1), 197–200 (1999).
- ³³V. Svrcek, T. Sasaki, and Y. Shimizu, "Aggregation of silicon nanocrystals prepared by laser ablation in deionized water," *J. Micro/Nanoeng.* **2**, 15–19 (2007).
- ³⁴M. H. Mahdiah and A. Momeni, "From single pulse to double pulse ns laser ablation of silicon in water: Photoluminescence enhancement of silicon nanocrystals," *Laser Phys.* **25**(1), 015901 (2015).
- ³⁵V. Svrcek, T. Sasaki, Y. Shimizu, and N. Koshizaki, "Blue luminescent silicon nanocrystals prepared by ns pulsed laser ablation in water," *Appl. Phys. Lett.* **89**(21), 213113 (2006).
- ³⁶V. Svrcek, T. Sasaki, R. Katoh, Y. Shimizu, and N. Koshizaki, "Aging effect on blue luminescent silicon nanocrystals prepared by pulsed laser ablation of silicon wafer in de-ionized water," *Appl. Phys. B* **94**(1), 133 (2009).
- ³⁷D. M. Popovic, J. S. Chai, A. A. Zekic, M. Trtica, J. Stasic, and M. Z. Sarvan, "The Influence of applying the additional continuous laser on the synthesis of silicon-based nanoparticles by picosecond laser ablation in liquid," *Laser Phys. Lett.* **11**(11), 116101 (2014).
- ³⁸F. Friedrich, C. Boehme, and K. Lips, "Triplet recombination at Pb centers and its implications for capture cross sections," *J. Appl. Phys.* **97**(5), 056101 (2005).
- ³⁹G. J. Gerardi, E. H. Poindexter, P. J. Caplan, and N. M. Johnson, "Interface traps and Pb centers in oxidized (100) silicon wafers," *Appl. Phys. Lett.* **49**(6), 348–350 (1986).
- ⁴⁰A. Sa'ar, Y. Reichman, M. Dovrat, D. Krapf, J. Jedrzejewski, and I. Balberg, "Resonant coupling between surface vibrations and electronic states in silicon nanocrystals at the strong confinement regime," *Nano Lett.* **5**(12), 2443–2447 (2005).
- ⁴¹S. Yang, W. Li, B. Cao, H. Zeng, and W. Cai, "Origin of blue emission from silicon nanoparticles: Direct transition and interface recombination," *J. Phys. Chem. C* **115**(43), 21056–21062 (2011).
- ⁴²L. Skuja, "Optically active oxygen-deficiency-related centers in amorphous silicon dioxide," *J. Non-Cryst. Solids* **239**(1–3), 16–48 (1998).
- ⁴³V. N. Bagratashvili, S. I. Tsygina, V. A. Radtsig, A. O. Rybaltovskii, P. V. Chernov, S. S. Alimpiev, and Y. O. Simanovskii, "Inhomogeneous nature of UV absorption bands of bulk and surface oxygen-deficient centers in silica glasses," *J. Non-Cryst. Solids* **180**(2), 221–229 (1995).
- ⁴⁴R. Boscaino, M. Cannas, F. M. Gelardi, and M. Leone, "Spectral and kinetic properties of the 4.4-eV photoluminescence band in a-SiO₂: Effects of γ irradiation," *Phys. Rev. B* **54**(9), 6194–6199 (1996).
- ⁴⁵L. Vaccaro, L. Sciortino, F. Messina, G. Buscarino, S. Agnello, and M. Cannas, "Luminescent silicon nanocrystals produced by near-infrared nanosecond pulsed laser ablation in water," *Appl. Surf. Sci.* **302**, 62–65 (2014).
- ⁴⁶L. Skuja and B. Güttler, "Detection of interstitial oxygen molecules in SiO₂ glass by a direct photoexcitation of the infrared luminescence of singlet O₂," *Phys. Rev. Lett.* **77**(10), 2093–2096 (1996).
- ⁴⁷G. Vaccaro, S. Agnello, G. Buscarino, M. Cannas, and L. Vaccaro, "Structural and luminescence properties of amorphous SiO₂ nanoparticles," *J. Non-Cryst. Solids* **357**(8–9), 1941–1944 (2011).
- ⁴⁸D. M. Cary and G. M. Korenowski, "Measurement of the Raman spectrum of liquid water," *J. Chem. Phys.* **108**(7), 2669–2675 (1998).
- ⁴⁹K. Dohnalová, A. N. Poddubny, A. A. Prokofiev, W. D. de Boer, C. P. Umesh, J. M. Paulusse, H. Zuilhof, and T. Gregorkiewicz, "Surface brightens up Si quantum dots: Direct bandgap-like size-tunable emission," *Light Sci. Appl.* **2**(1), e47 (2013).
- ⁵⁰L. Vaccaro, G. Vaccaro, S. Agnello, G. Buscarino, and M. Cannas, "Wide range excitation of visible luminescence in nanosilica," *Solid State Commun.* **150**(45–46), 2278–2280 (2010).
- ⁵¹J. Xiao, P. Liu, L. Li, and G. Yang, "Fluorescence origin of nanodiamonds," *J. Phys. Chem. C* **119**(4), 2239–2248 (2015).
- ⁵²J. Xiao, P. Liu, C. X. Wang, and G. W. Yang, "External field-assisted laser ablation in liquid: An efficient strategy for nanocrystal synthesis and nanostructure assembly," *Prog. Mater. Sci.* **87**, 140–220 (2017).
- ⁵³A. De Giacomo, M. Dell'Aglia, A. Santagata, R. Gaudiuso, O. De Pascale, P. Wagnier, G. C. Messina, G. Compagnini, and S. Barcikowski, "Cavitation dynamics of laser ablation of bulk and wire-shaped metals in water during nanoparticles production," *Phys. Chem. Chem. Phys.* **15**(9), 3083–3092 (2013).
- ⁵⁴M. Dell'Aglia, R. Gaudiuso, O. D. Pascale, and A. De Giacomo, "Mechanisms and processes of pulsed laser ablation in liquids during nanoparticle production," *Appl. Surf. Sci.* **348**, 4–9 (2015).
- ⁵⁵D. Zhang, B. Gokce, and S. Barcikowski, "Laser synthesis and processing of colloids: Fundamentals and applications," *Chem. Rev.* **117**(5), 3990–4103 (2017).
- ⁵⁶S. Preuss, A. Demchuk, and M. Stuke, "Sub-picosecond UV laser ablation of metals," *Appl. Phys. A: Mater. Sci. Process.* **61**(1), 33–37 (1995).
- ⁵⁷S. Barcikowski, A. Menéndez-Manjón, B. Chichkov, M. Brikas, and G. Račiukaitis, "Generation of nanoparticle colloids by picosecond and femtosecond laser ablations in liquid flow," *Appl. Phys. Lett.* **91**(8), 083113 (2007).
- ⁵⁸R. Streubel, G. Bendt, and B. Gokce, "Pilot-scale synthesis of metal nanoparticles by high-speed pulsed laser ablation in liquids," *Nanotechnology* **27**(20), 205602 (2016).
- ⁵⁹R. Streubel, S. Barcikowski, and B. Gokce, "Continuous multigram nanoparticle synthesis by high-power, high-repetition-rate ultrafast laser ablation in liquids," *Opt. Lett.* **41**(7), 1486–1489 (2016).
- ⁶⁰D. Perez and L. J. Lewis, "Thermodynamic evolution of materials during laser ablation under pico and femtosecond pulses," *Appl. Phys. A* **79**(4–6), 987–990 (2004).
- ⁶¹P. Lorazo, L. J. Lewis, and M. Meunier, "Short-pulse laser ablation of solids: From phase explosion to fragmentation," *Phys. Rev. Lett.* **91**(22), 225502 (2003).
- ⁶²R. Kelly and A. Miotello, "Contribution of vaporization and boiling to thermal-spike sputtering by ions or laser pulses," *Phys. Rev. E* **60**(3), 2616–2625 (1999).
- ⁶³R. K. Jain and M. B. Klein, "Degenerate four-wave mixing near the band gap of semiconductors," *Appl. Phys. Lett.* **35**(6), 454–456 (1979).
- ⁶⁴W. B. Gauster and J. C. Bushnell, "Laser-induced infrared absorption in silicon," *J. Appl. Phys.* **41**(9), 3850–3853 (1970).
- ⁶⁵J. M. Moison, F. Barthe, and M. Bensoussan, "Laser-induced nonlinear absorption in silicon: Free-carrier absorption versus thermal effects," *Phys. Rev. B* **27**(6), 3611–3619 (1983).
- ⁶⁶B. K. Ridley, *Quantum Processes in Semiconductors* (OUP Oxford, 1999).
- ⁶⁷H. Nabeshi, T. Yoshikawa, A. Arimori, T. Yoshida, S. Tochigi, T. Hirai, T. Akase, K. Nagano, Y. Abe, H. Kamada *et al.*, "Effect of surface properties of silica nanoparticles on their cytotoxicity and cellular distribution in murine macrophages," *Nanoscale Res. Lett.* **6**(1), 93 (2011).



Short communication

Galvanoluminescence of oxide films during the anodization of titanium

S. Stojadinović^{a,*}, R. Vasilic^b, M. Petković^a, I. Belča^a, B. Kasalica^a, Lj. Zeković^a^a Faculty of Physics, University of Belgrade, Studentski trg 12-16, Belgrade, Serbia^b Faculty of Environmental Governance and Corporate Responsibility, Educons University, Vojvode Putnika 87, Sremska Kamenica, Serbia

ARTICLE INFO

Article history:

Received 26 June 2013

Received in revised form 11 July 2013

Accepted 23 July 2013

Available online 31 July 2013

Keywords:

Titanium

Anodization

Galvanoluminescence

Breakdown

ABSTRACT

In this paper, we have presented the results of our investigation of galvanoluminescence (GL) originating from oxide films obtained by anodization of titanium in alkaline solutions. For the first time we have measured weak GL during the anodization of titanium and found strong influence of sample's surface pretreatment, as well as anodizing conditions (current density and electrolyte temperature). GL is more intense for rougher titanium samples, higher current density, and higher temperature of electrolyte. Spectral characterization of GL showed that there are wide GL bands present mostly in the visible and near infrared spectral region. As the potential of anodization approaches the breakdown voltage, a numerous transient sparks appear superimposed on the GL.

© 2013 Elsevier B.V. All rights reserved.

1. Introduction

Titanium is one of the most widely used metals due to its low-density, high melting point, nontoxic and biologically compatible with human tissues and bones, high strength, stiffness, good toughness, and good corrosion resistance. These properties make titanium valuable in a number of applications including the aerospace, chemical and petrochemical industries, military and biomedicine [1]. The technique of titanium anodization has been used for many years to improve the surface properties. In recent years, anodic titanium oxides have found new areas of applications in sensors, photocatalysis, photovoltaic devices, solar cells, and biomaterials [2,3].

The aim of this work is to investigate galvanoluminescence (GL) during titanium anodization in alkaline solutions. The GL is a common name for light appearing at one of the electrodes in an electrolyte solution during anodization [4]. Despite numerous articles considering GL, especially on aluminum, there is no data on GL during titanium anodization. Most probable reason for this is very low, almost immeasurable GL intensity, which depends on many factors, such as surface pretreatment, anodic conditions, and wavelength of light emission. Our investigations of the GL during aluminum anodization have showed that the nature and GL intensity depend on the type of the electrolyte, surface pretreatment, and anodizing conditions [5–13]. Concentration of impurities and surface pretreatment are factors which strongly affect the GL intensity in inorganic electrolytes [5–8]. In the case of organic electrolytes GL is agitated by collision of electrons, injected into the oxide film at the electrolyte-oxide interface and accelerated by high electric field (nearly 10^7 V/cm), with GL centers (carboxylate ions)

inside the oxide film [10,11]. In the case of some other valve metals (magnesium, zirconium) GL is correlated to the existence of flaws in oxide films generated by surface impurities [14,15].

2. Experimental

Titanium samples (99.5% purity, Alfa Aesar) were used as the starting material. Before the anodization, samples were degreased in acetone using ultrasonic cleaner. The anodization process was carried out in an electrolytic cell with flat glass windows [11]. Two platinum wires (5 cm long and 1 mm in diameter) were used as cathodes. During the anodization, the electrolyte circulated through the chamber–reservoir system and temperature of the electrolyte was maintained constant within 0.1 °C [11].

Titanium samples were anodized in water solution of 10 g/L $\text{Na}_3\text{PO}_4 \cdot 12\text{H}_2\text{O}$. Anodizing was carried out at different current densities in the 50–150 mA/cm² range and different temperatures in the 14–34 °C range. Experimental setup used for luminescence measurements was described in [15]. The roughness of titanium samples was analyzed using an atomic force microscope.

3. Results and discussion

Fig. 1a shows typical potential of anodization vs. time and luminescence intensity vs. time characteristics during the titanium anodization. From the beginning of anodization, potential of anodization increases linearly with time to about 245 V, resulting in the constant rate of increase of the barrier oxide film thickness (stage I). Simultaneously, low GL is observed. This stage of anodization is followed by apparent deflection from linearity in potential of anodization–time curve, starting from so-called breakdown voltage (stage II). After the breakdown,

* Corresponding author. Tel.: +381 11 7158161; fax: +381 11 3282619.
E-mail address: sstevan@ff.bg.ac.rs (S. Stojadinović).

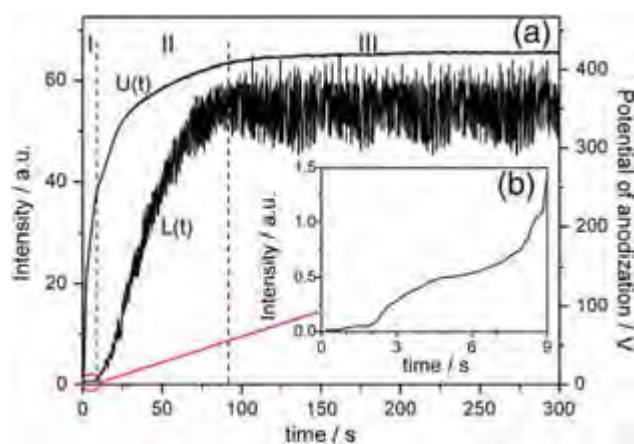


Fig. 1. Time variation during galvanostatic anodization of titanium: (a) anodization potential and luminescence intensity; and (b) GL intensity ($j = 150 \text{ mA/cm}^2$, $t_{\text{el}} = 20^\circ\text{C}$, $\lambda = 600 \text{ nm}$).

potential of anodization continually increases, but the slope of the curve decreases and a large number of small sized sparks appear, evenly distributed over the whole sample surface. Sparking luminescence combines with the GL and, as a result, the total luminescence intensity increases. Further anodization results in relatively stable value of the potential of anodization and luminescence intensity (stage III).

Fig. 1b shows GL intensity vs. time characteristic during the anodization of titanium (stage I in Fig. 1a). GL intensity quasi-exponentially increases with time, or potential of anodization. Based on previous research of GL, very low GL intensity indicates that the flaws (microfissures, cracks, local region of different compositions) in oxide films are main generators of luminescence. These impurities act as preferable places for radiative recombination of electrons injected into conducting band of the oxide films and multiplied in avalanching process [16].

To confirm our assumption that GL is caused by the flaws in oxide films formed by anodization of titanium, we roughened the surface of samples with P220 SiC paper. Average surface roughness ranged from about 200 nm for as received samples (Fig. 2a) to about 800 nm for additionally roughened samples (Fig. 2b). Fig. 2c shows that roughened samples have higher GL intensity. Increased GL intensity is related to the fact that energy gap between the conduction and valence bands in titanium oxide is about 3.2 eV [17] and therefore there are no electrons present in conduction band. The electrons, which take part in GL are injected into the conduction band from the electrolyte/oxide interface and accelerated by the electric field during the anodization [16]. Some of electrons may fall from the conduction band to impurity levels in band gap emitting GL. That is why we have observed strong influence of the concentration of flaws on GL intensity. Consequently, GL intensity might be an indicator of state of titanium sample's surface, as well as of roughness caused by the pretreatment procedures of titanium films. Surface roughness of titanium is one of the important parameters for formatting oxide films by anodization with good corrosion and wear resistance properties as well as optimal biological response [18].

The influence of anodization conditions on GL intensity is shown in Fig. 3. GL is more intense for higher current density and higher electrolyte temperature. It is well known that GL intensity is proportional to current density for constant thickness (thickness of a barrier part is determined by potential of anodization [19]) and that is in agreement with our results. Also, electronic component of anodization current which is responsible for GL, is higher for higher electrolyte temperature at the same voltage [20], resulting in higher GL intensity.

The exponential dependence of GL intensity with time under galvanostatic conditions prevents measuring of GL spectra by measuring of GL intensities on wide range of wavelengths. This obstacle can be overcome by working under potentiostatic conditions. Fig. 4a presents anodization current density and GL intensity vs. time curves for

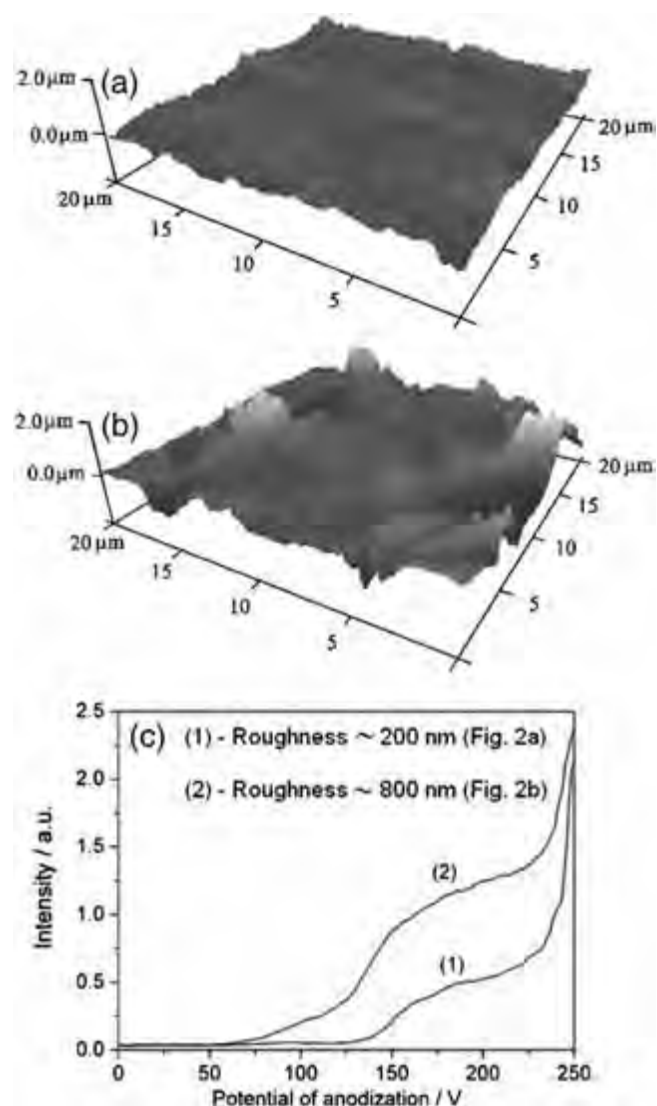


Fig. 2. (a) AFM image of as received titanium; (b) AFM image of roughened titanium; (c) effect of surface roughness of titanium on GL intensity.

constant potential of anodization. Clearly, right after applying a constant voltage, barrier oxide film begins to grow and anodization current density sharply increases to a certain maximum. During this stage of

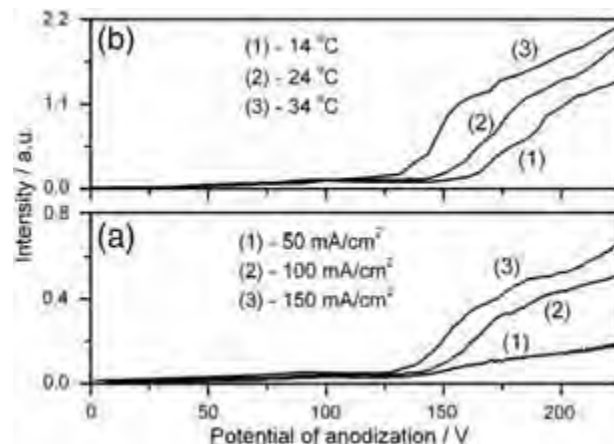


Fig. 3. Effect of anodizing conditions on GL intensity: (a) influence of current density ($t_{\text{el}} = 20^\circ\text{C}$, $\lambda = 600 \text{ nm}$); and (b) influence of electrolyte temperature ($j = 150 \text{ mA/cm}^2$, $\lambda = 600 \text{ nm}$).

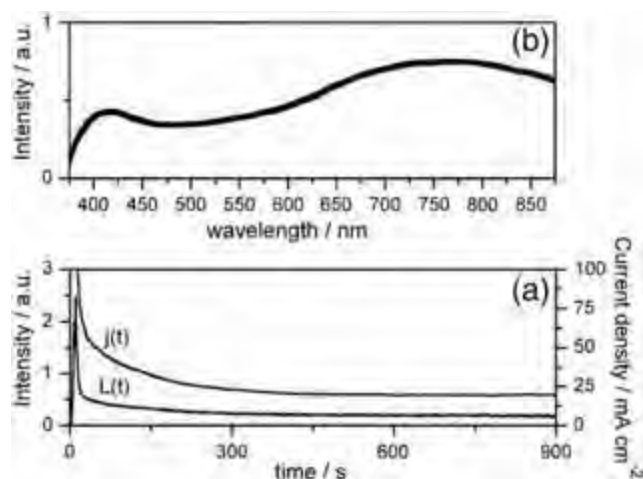


Fig. 4. (a) Time variation of current density and GL intensity during potentiostatic anodization of titanium; (b) GL spectrum ($U = 200$ V, $t_{el} = 20$ °C).

anodization, anodic current mainly consists of ionic current that forms oxide film. Upon reaching certain oxide film thickness (corresponding voltage of anodization), anodization current density begins to decrease. After some time from the beginning of anodization, oxide film ceases to grow significantly, which corresponds to lower values of anodization current density. This, lower, current density is predominantly electronic current that has no influence on oxide film thickening, but influences

GL. Constant values of GL intensity and current density allow measurement of GL spectra in steady-state regime by simple measurement of GL intensity at various wavelengths. Fig. 4b shows a typical shape of the spectrum. Wide GL bands are presented in 375–875 nm range, with two spectral maxima around 420 nm and 760 nm.

Luminescence spectrum under breakdown conditions (stages II and III in Fig. 1a) is shown in Fig. 5a. The strongest lines originate from electrolyte and belong to NaI at 588.99 nm and 589.59 nm, Balmer line H_{α} (656.28 nm), OI at 777.19 nm, 777.42 nm, and 777.54 nm, NaI at 818.33 nm and 819.47 nm, and OI at 844.64 nm. We also detected the following relatively strong lines: Balmer line H_{β} (486.13 nm), OI at 715.67 nm, and three lines of OI at 794.75 nm, 795.08 nm, and 795.22 nm. In order to identify weaker emission lines at lower wavelengths we thoroughly investigated the spectral region from 375 nm to 525 nm (Fig. 5b). Many lines of OII, Balmer line H_{γ} (434.05 nm), which originate from electrolyte as well as TiI and TiII lines from substrate are identified. The notations I and II refer to neutral and singly ionized atoms, respectively. The continuum emission between 375 nm and 850 nm results from collision-radiative recombination of electrons.

4. Conclusions

We have demonstrated that the anodization of titanium in alkaline solutions is followed by weak galvanoluminescence (GL). Wide GL bands are presented in the range from 375 nm to 875 nm, with two spectral maxima around 420 nm and 760 nm. GL is correlated to the existence of flaws in oxide films generated by surface impurities. These impurities act as preferable places for radiative recombination of electrons injected into conducting band of oxide and multiplied in avalanching process. GL intensity is significantly determined by anodizing conditions. GL is more intense for higher current density and higher temperature of electrolyte. Therefore, GL intensity can be used as a tool to determine titanium surface quality.

Under breakdown conditions of titanium anodization sparking luminescence combines with the GL and the total luminescence intensity increases significantly. Luminescence spectrum under breakdown have intensive emission band peaks which originated from titanium electrode and electrolyte.

Acknowledgment

This work is supported by the Ministry of Education, Science and Technological Development of the Republic of Serbia under project No. 171035.

References

- [1] C. Leyens, M. Peters, Titanium and Titanium Alloys: Fundamentals and Applications, Wiley-VCH, Weinheim, Germany, 2003.
- [2] A. Mazzarolo, K. Lee, A. Vicenzo, P. Schmuki, Electrochemistry Communications 22 (2012) 162.
- [3] C. Moseke, F. Hage, E. Vorndran, U. Gbureck, Applied Surface Science 258 (2012) 5399.
- [4] S. Ikonopisov, Electrochimica Acta 20 (1975) 783.
- [5] S. Stojadinovic, Lj. Zekovic, I. Belca, B. Kasalica, Electrochemistry Communications 6 (2004) 427.
- [6] S. Stojadinovic, Lj. Zekovic, I. Belca, B. Kasalica, D. Nikolic, Electrochemistry Communications 6 (2004) 708.
- [7] S. Stojadinovic, I. Belca, Lj. Zekovic, B. Kasalica, D. Nikolic, Electrochemistry Communications 6 (2005) 1016.
- [8] B. Kasalica, S. Stojadinovic, Lj. Zekovic, I. Belca, D. Nikolic, Electrochemistry Communications 6 (2005) 735.
- [9] S. Stojadinovic, I. Belca, B. Kasalica, Lj. Zekovic, M. Tadic, Electrochemistry Communications 8 (2006) 1621.
- [10] S. Stojadinović, M. Tadić, I. Belča, B. Kasalica, Lj. Zeković, Electrochimica Acta 52 (2007) 7166.
- [11] S. Stojadinovic, I. Belca, M. Tadic, B. Kasalica, Z. Nedic, Lj. Zekovic, Journal of Electroanalytical Chemistry 125 (2008) 619–620.
- [12] S. Stojadinovic, R. Vasilic, M. Petkovic, Z. Nedic, B. Kasalica, I. Belca, Lj. Zekovic, Electrochimica Acta 55 (2010) 3857.
- [13] M. Sarvan, S. Stojadinovic, B. Kasalica, I. Belca, Lj. Zekovic, Electrochimica Acta 53 (2008) 2183.

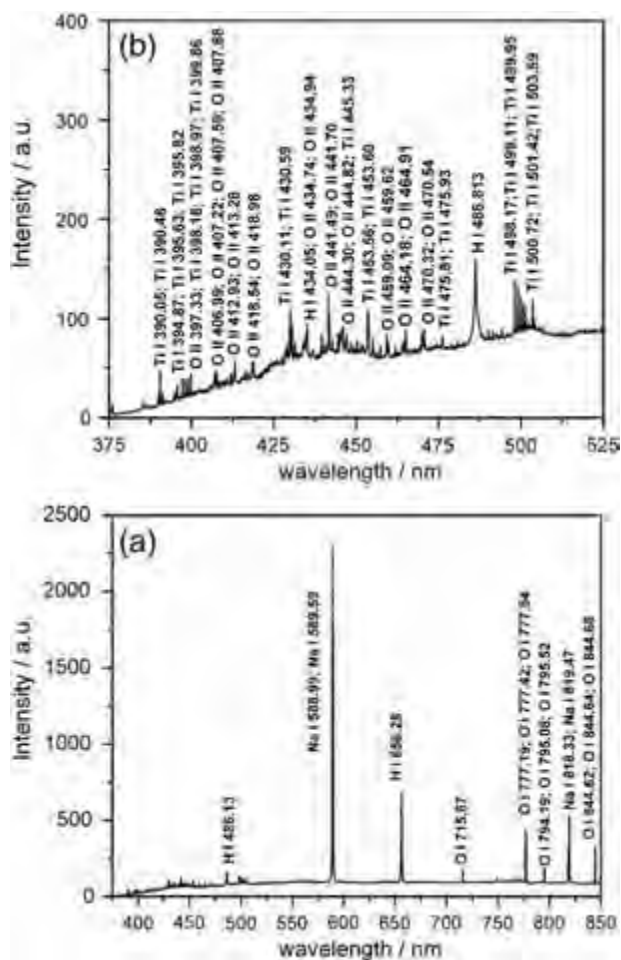


Fig. 5. Luminescence spectrum recorded under breakdown conditions in the range: (a) 375–850 nm; and (b) 375–525 nm.

- [14] S. Stojadinović, R. Vasilić, M. Petković, I. Belča, B. Kasalica, M. Perić, Lj. Zeković, *Electrochimica Acta* 59 (2012) 354.
- [15] S. Stojadinović, R. Vasilić, M. Petković, I. Belča, B. Kasalica, M. Perić, Lj. Zeković, *Electrochimica Acta* 79 (2012) 133.
- [16] S. Ikonopisov, A. Girginov, M. Machkova, *Electrochimica Acta* 24 (1979) 451.
- [17] K. Kaur, C.V. Singh, *Energy Procedia* 29 (2012) 291.
- [18] D.D. Deligianni, N. Katsala, S. Ladas, D. Sotiropoulou, J. Amedee, Y.F. Missirlis, *Biomaterials* 22 (2001) 1241.
- [19] W. Ch, C.A. van Geel, B.C. Bouma Pistorius, *Philips Research Reports* 12 (1957) 465.
- [20] A. Charlesby, *Proceedings of the Physical Society LXVI* 7-B (1953) 533.



CrossMark

Investigation of long-duration plasma electrolytic oxidation of aluminum by means of optical spectroscopy

M. Sarvan^a, J. Radić-Perić^b, B. Kasalica^{a,*}, I. Belča^a, S. Stojadinović^a, M. Perić^b

^a Faculty of Physics, University of Belgrade, Studentski trg 12-16, 11000 Belgrade, Serbia

^b Faculty of Physical Chemistry, University of Belgrade, Studentski trg 12-16, 11000 Belgrade, Serbia

ARTICLE INFO

Article history:

Received 9 April 2014

Accepted in revised form 15 June 2014

Available online 22 June 2014

Keywords:

Aluminum

Plasma electrolytic oxidation

Emission spectrum

Temperature

ABSTRACT

The process of plasma electrolytic oxidation of aluminum was investigated by means of optical spectroscopy at a very long time interval. The change of morphology of obtained oxide coatings in the course of time was studied. Several hundreds of low-resolution emission optical spectra in the wavelength region between 250 nm and 850 nm, and higher-resolution spectra in the region from 230 nm to 290 nm were taken at the time interval up to 300 min from the beginning of the anodization. The spectra consisted of spectral lines and bands originating both from the anode material (Al, i.e. AlO) and the electrolyte (water solution of the boric acid and sodium tetraborate). Three pairs of spectral lines of aluminum were used to estimate the plasma temperature. It was found to be about 8000 K at the beginning of the process and as low as 3000–4000 K after roughly 1 h. The composition of the plasma containing aluminum, oxygen, hydrogen, and sodium was calculated in the temperature range up to 11,000 K under assumption of local thermal equilibrium, in order to explain the appearance of the observed spectral features.

© 2014 Elsevier B.V. All rights reserved.

1. Introduction

In the present study we continue our investigation of the process of plasma electrolytic oxidation (PEO) of lightweight metals, particularly of aluminum [1–10]. In PEO, in contrast to conventional anodic oxidations, voltages above the dielectric breakdown potential are utilized. The main practical benefit of PEO is protection of these metals from corrosion through the forming of relatively thick coating layers on their surface. A comprehensive overview of the development in this research field until the end of the preceding century was presented e.g. by Yerokhin et al. [11].

PEO of aluminum is a complex electrochemical process consisting of several consecutive and parallel steps, involving oxide layer formation, gas (hydrogen and oxygen) evolution, dielectric breakdown, formation of microdischarge plasma zones on the electrode surface, and plasma chemical reactions in them, accompanied by light emission. It starts with the formation of a thin barrier oxide layer on the metal surface. In the case of PEO, the electrode processes cannot be understood based on a simple two-phase model electrode–electrolyte, like in conventional electrochemistry [11]. Due to high electric field (order of magnitude 10^7 V/cm) in the regime of (and above) the dielectric breakdown voltage, thicker (up to several hundred nm) amorphous barrier oxide layers are produced at both the aluminum/oxide and oxide/electrolyte interfaces, as a result of migration of the O_2^-/OH^- and Al^{3+}

ions across the oxide. The process begins with formation of a number of separated discharge channels in the oxide layer. This region is heated by electron avalanches up to temperatures of 10^4 K. The strong electric field causes the migration of anions from the electrolyte into the channels and melting of aluminum that in this form enters the channels, where it becomes oxidized. The pressure inside the channels is highly increased (up to $\sim 10^2$ MPa [11]) and various plasma-chemical reactions involving the species from the electrolyte and substrate take place in them. In the last phase of the process, the cations are pushed from the channels into the electrolyte and the oxidized metal is ejected from the channels into the coating surface in contact with the electrolyte, forming in this way the coatings of increased thickness. Finally, the discharge channels cool, with the reaction products being deposited onto their walls. The results of previous investigations have led to the conclusion that the discharge plasma consists of a central core with the temperature at roughly 7000 K [12–14], surrounded by lower-temperature (about 3500 K) regions. Dunleavy et al. [15] organized special experimental conditions, which allowed them to isolate a single discharge, and concluded that the local thermal equilibrium (LTE) conditions were fulfilled in the plasma core, while the colder peripheral region was found to be in partial LTE.

The most widely applied technique for characterization of microdischarges has been optical emission spectroscopy (OES) in the visible and near UV spectral region. It serves to identify the species present in the systems investigated, and to determine important parameters of these systems, like temperature, electron density, and total pressure [5,6,8,9,12,15–24]. Assuming the existence of LTE, in several studies the electron temperature has been determined based on the relative

* Corresponding author. Tel.: +381 11 7158161; fax: +381 11 3282619.
E-mail address: kasalica@ff.bg.ac.rs (B. Kasalica).

intensity of spectral lines of atoms originating both from substrate and the electrolyte [5,9,12,16–18]. The shape of spectral lines, particularly those of the hydrogen Balmer series, has been used for estimation of the electron density in plasma [5,9,15,18]. The molecular vibrational temperature was determined from the $B^2\Sigma^+-X^2\Sigma^+$ emission transition of AlO [8] and $B^1\Sigma^+-X^1\Sigma^+$ transition of MgO [24]. The plasma temperature was also estimated by means of the unresolved rotational structure of the $A^2\Sigma^+ (\nu' = 0)-X^2\Pi (\nu'' = 0)$ emission spectrum of OH [15,24].

2. Experimental

As anode we used high-purity cold-rolled aluminum (99.999%, produced by Goodfellow) samples of $25\text{ mm} \times 7\text{ mm} \times 0.12\text{ mm}$. The aluminum surface was degreased in ethanol by means of an ultrasonic cleaner and dried in a warm air stream. Platinum wires were used as cathodes. The anodic oxidation process took place in a 100 ml volume electrolytic cell with flat quartz glass windows. The electrolyte was water solution involving 0.1 mole of boric acid (H_3BO_3) and 0.05 mole sodium tetraborate ($Na_2B_4O_7 \cdot 10H_2O$), prepared by double distilled deionized water and PA grade chemical compounds. This buffer ensures the pH value of the electrolyte of about 8. During the anodization, the electrolyte circulated through the chamber-reservoir system, and the temperature of the electrolyte was kept at 20°C . The PEO process took place at the constant current density of 10 mA/cm^2 achieved by a highly stabilized power supply.

Scanning electron microscope (SEM) JEOL 840A equipped with energy dispersive X-ray spectroscopy (EDX) was used to characterize morphology and chemical composition of formed oxide coatings.

Spectroscopic measurements were performed utilizing two different spectrometer systems. Fiber optic spectrometer USB4000 UV/VIS manufactured by Ocean Optics was used for spectral measurement in segment from 250 nm to 850 nm. The spectrometer detector consisted of a 3648-element linear CCD array with a grating of 600 lines/mm blazed at 300 nm. The entrance slit of spectrometer was fixed at $25\text{ }\mu\text{m}$ in width. Spectral resolution of spectrometer was 1.5 nm (Full Width at Half-Maximum). The light emitted during PEO was transmitted from Ocean Optic QP400-2-UV/BX, on the spectrometer slit. Optical fiber had a core diameter of $400\text{ }\mu\text{m}$, spectral range from 300 nm to 1100 nm, and a numerical aperture of 0.22.

Spectral measurement with better resolution during PEO were taken on a spectrometer system consisting of a quartz objective, Czerny-Turner spectrometer, and thermoelectrically cooled (-10°C) CCD detector (2048×506 pixels, each approximately $12\text{ }\mu\text{m} \times 12\text{ }\mu\text{m}$) manufactured by Hamamatsu. This system was used for spectral measurement in the segment of 60 nm and resolution of 0.2 nm.

3. Results and discussion

3.1. Time dependence of the anodization potential

Potential of anodization versus time curve is shown in Fig. 1. This topic is discussed in more detail e.g. in our recent study on PEO of Mg [23] and we present here only a brief summary.

The time dependence of the voltage can be separated into three regions reflecting the processes described in the Introduction. At the beginning of anodization, the voltage increases approximately linearly with time up to about 400 V (breakdown voltage), resulting in the constant rate of increase of the oxide film thickness (stage I). Simultaneously, low anodic light emission is observed, caused by radiative recombination of electrons at flaws in the oxide film. The stage of anodization in which avalanche multiplication of electrons takes place corresponds to apparent deflection from linearity of the voltage–time curve (stage II). After the breakdown, voltage continually increases, but the voltage–time slope decreases. Sparking emission combines with the anodic emission and, as a result, the total emission intensity

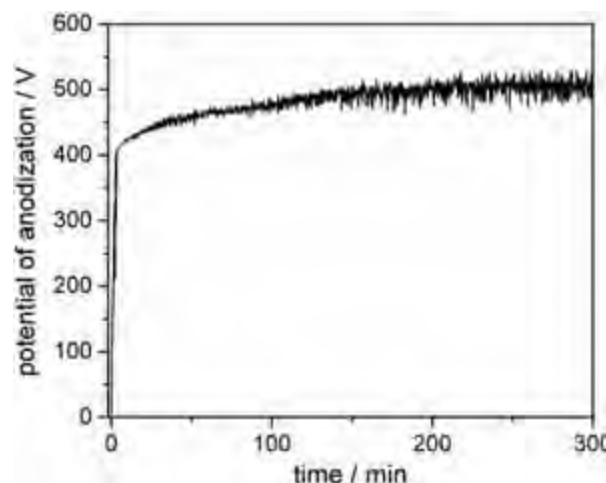


Fig. 1. Time variation of potential of anodization during PEO of aluminum.

increases. Further anodization (after about 1 h) results in a nearly constant value of the voltage of anodization (stage III).

During anodization the total current density is the sum of ionic current density and of electron current density. In the stage I the ionic current is two to three orders of magnitude larger than the electronic component. In the stage II a relatively low voltage increase (compared with the stage I) is required to maintain the same total current density, due to the independence of the electron current density of the anodic oxide film thickness. In the stage III, the fraction of electron current density becomes dominant.

3.2. Morphology of oxide coatings

In Fig. 2a we show a SEM micrograph of the anode surface taken before the dielectric breakdown. The surface is relatively smooth and homogenous. The Al substrate is covered with a thin layer of Al_2O_3 . The SEM micrograph of the anode surface 1 h after beginning the PEO process is presented in Fig. 2b. The surface is much rougher than that shown in Fig. 2a. It is characterized by numerous, predominantly small and medium-size, pores and channels. The EDX spectrum taken at the surface of the anode involves Al and O peaks, whereas in that corresponding to the inner part of the electrode only the Al signal appears. Three hours after beginning of the PEO process the surface of the electrode has the shape presented in Fig. 2c. The surface is extremely rough and damaged; the number of cracks is smaller than in Fig. 2b, but they are much larger (and particularly deeper, reaching in a number of cases the metal substrate). Also in this case the EDX spectrum contains Al and O signals. The above findings concerning the morphology of the Al electrode are similar to those by Hussein et al. [17], who discussed this topic in terms of “A, B, and C” positions on the surface.

3.3. Spectroscopy of PEO process

The spectra were recorded up to 300 min from the beginning of the discharge process. This time interval is much larger than that chosen, for example, by Hussein et al. (up to 60 min) [17]. The first series of measurements were carried out at low resolution in the spectral region between 250 nm and 850 nm. A typical spectrum, recorded 150 min after beginning of the PEO process, is presented in Fig. 3. These spectra are dominated by four, in general strong spectral lines, H_α at 656.29 nm, the Na doublet lines at 588.995 nm and 589.592 nm, and the Al I lines at 309 nm and 396 nm. Besides, we detected several bands of AlO, OH, and possibly AlH. The H_β (486.135 nm) hydrogen line is in the most recordings of weak intensity.

Hussein et al. [17] used the Al lines at 309 and 396 nm to determine the plasma temperature. We refrained from them for the following

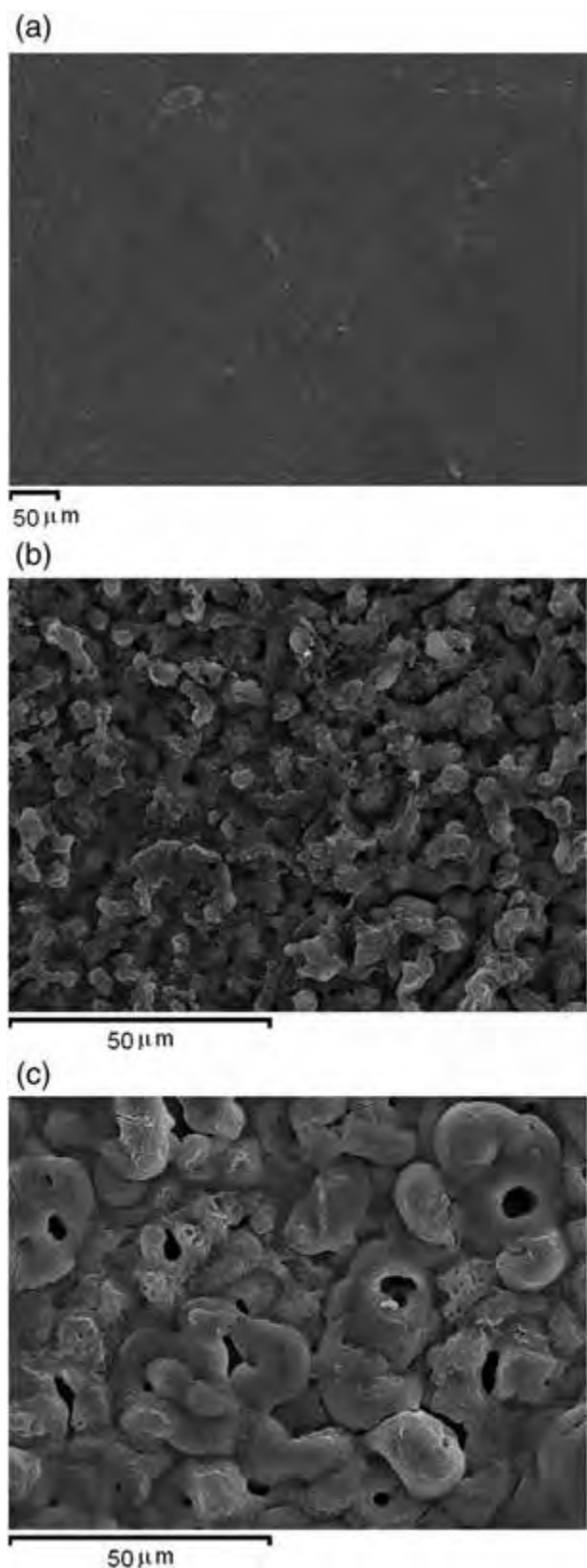


Fig. 2. SEM micrographs of oxide coating surface formed: (a) before dielectric breakdown; (b) 60 min after beginning of the PEO process; and (c) 300 min after beginning of the PEO process.

reasons: The first of these species is composed of three closely lying lines (308.21 nm, 309.27 nm, and 309.28 nm) corresponding to the transitions from the $J = 3/2$ and $J = 5/2$ spin components of the excited

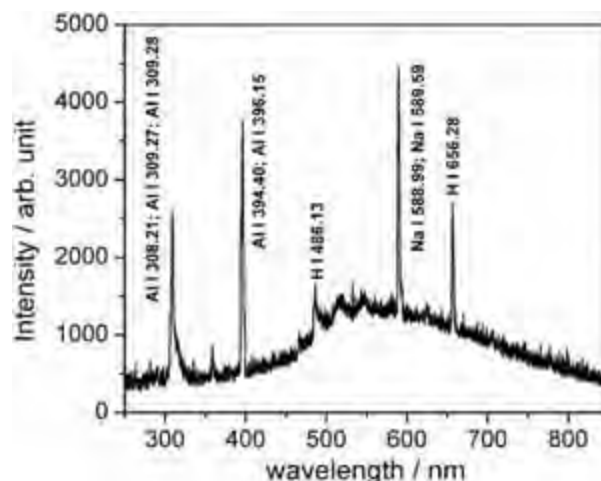


Fig. 3. Low-resolution emission spectrum recorded 150 min after beginning of the PEO process.

2D ($3s^23d$) state to the $J = 1/2$ and $J = 3/2$ levels of the ground 2P ($3s^23p$) state [25]. These three lines are not clearly resolved in our spectra. Further, they are overlapped with the parts of the $C^2\Pi-X^2\Sigma$ band system of AlO [main band heads at 311.26 (0,1), 302.16 (0,0), and 295.57 (1,0) nm], and with the bands of the $A^2\Sigma^+-X^2\Pi$ system of OH (a number of bands around 306.4 nm) [26]. The 396 nm species is composed of two spectral lines corresponding to the transitions 2S ($3s^24s$) \rightarrow $^2P_{1/2}$ ($3s^23p$) at 394.40 nm, and 2S ($3s^24s$) \rightarrow $^2P_{3/2}$ ($3s^23p$) at 396.15 nm, poorly resolved in our spectra. Finally, the Al lines at 309 and 396 nm are quite far from one another and also for this reason they are not ideal for estimating the temperature.

Random distribution of absolute intensities of spectral lines from one record to another, relatively large background intensities, difficulties in distinguishing the continuum radiation from some parts of spectral band systems, wavelength dependence of the recording sensitivity, etc. signalize that one has to be very careful when drawing conclusions concerning the evolution of the spectral line/band intensities. Thus, we summarize here only general trends. The intensity of both Al lines (more precisely, two groups of lines) decreases in the course of time. The decrease of the 396 nm species is apparently more pronounced, but one should keep in mind that the 309 nm line is heavily overlapped with the OH and AlO bands. The H_α line shows relatively small variation with time. On the other hand, the Na spectral lines are at the beginning of the process weak but their intensity continuously increases, this increase being much more pronounced than the decrease of the Al lines.

Another series of recordings were carried out under higher resolution in the spectral region between 230 nm and 290 nm (Fig. 4). Interestingly, Hussein et al. [17] had claimed that they had not obtained signals below 285 nm “probably due to self-absorption by the electrolyte”. Note that these authors used as electrolyte Na_2SiO_3 mixed with KOH. We recorded, however, a number of spectral lines and bands originating both from the Al sample and the electrolyte. This is in accordance with the results of our above cited previous studies, where we had registered several bands of diatomic molecules/radicals involving Al, O, and H.

In the present case we recorded the Al I spectral lines around 237 nm and 257 nm, and at 265.25 nm and 266.04 nm. The first two species consist actually of two groups of poorly resolved lines. The 237 nm group involves the lines with the wavelengths of 236.71 nm, 237.21 nm, 237.31 nm, 237.33 nm, and 237.84 nm, corresponding to the transitions from $J = 3/2$ and $J = 5/2$ spin components of the excited 2D ($3s^23p$) state, and from the 2S ($2s^26s$) state ($J = 1/2$), to the $J = 1/2$ and $J = 3/2$ levels of the ground 2P ($3s^23p$) state [25]. The 257 nm feature is composed of three lines involving the upper state assigned to y^2D [$3s^2(1S)nd$] ($J = 5/2, J = 3/2$) and the $J = 1/2$ and $J = 3/2$ component

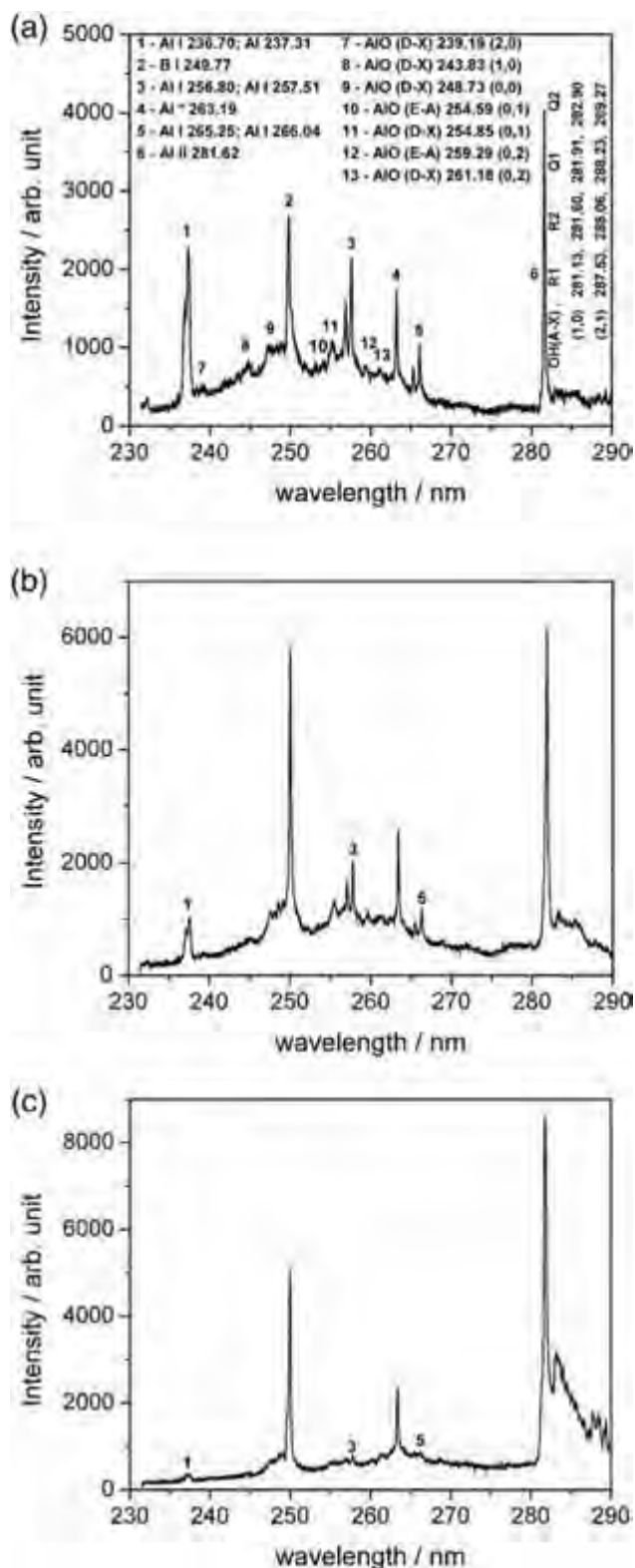


Fig. 4. Higher-resolution emission spectra in the range from 230 nm to 290 nm recorded: (a) 16 min after beginning of the PEO process; (b) 150 min after beginning of the PEO process; and (c) 298 min after beginning of the PEO process.

of the ground 2P state. In this case we obtained in our spectrum two resolved peaks, the first one corresponding to 256.80 nm, and the second involving the mutually overlapped 257.51 nm and 257.44 nm lines. The lines at 265.25 nm and 266.04 nm have as the upper state a 2S species ($3s^25s$) and therefore they are single. The difference in their

wavelengths is only caused by the spin-splitting of the ground 2P state. Thus, the ratio of intensities of these two lines (theoretically it should be two) cannot be used for estimation of the temperature, but it can be utilized for checking whether the conditions for determination of the temperature based on Al line intensities [existence of the partial local thermal equilibrium (partial LTE), linear response of the detection system, correct handling of the background emission, etc.] are fulfilled. Additionally, they are in general of low intensity and thus not quite convenient for combinations with other Al I spectral lines. For this reason we determined the plasma temperature by comparing the intensities of the lines Al I 237 nm, 257.51 nm, and the stronger (266.04 nm) of the above mentioned ones.

At the first sight, the apparently strong spectral line recorded slightly below 282 nm (see Fig. 4) should be unambiguously assigned to the 281.65 nm species of Al II, being the only ionic species of Al expected to be seen in the wavelength region in question. However, this line is overlapped with the bands of the $A^2\Sigma^+-X^2\Pi$ system of OH (R_1 , R_2 heads at 281.13 nm, 281.60 nm, degraded to red, of the relatively strong (1,0) transition [26]) and thus it would be very risky to use it for estimation of the electron density. As will be shown below, the change of the intensity of the 282 nm line in the course of time resembles that of the species originating from the electrolyte, and is not such as would be expected from an Al ionic line.

We also recorded two strong lines around 249.7 nm and 262.2 nm. The first one is assigned to the 249.68 nm species of B I. Of all the elements which could be found in the systems like the present one, only atomic silicon has a spectral line (263.13 nm) that corresponds to the feature observed at 262.2 nm. We carefully investigated the possibility that the appearance of the 262.2 nm line could be a consequence of Si-impurities either in the Al sample or in the electrolyte but came to the conclusion that this was not the case. We discovered then that this feature had already been assigned to Al II directly excited by charge transfer [27].

Several band systems also appear in our spectra. The most clearly pronounced are those of the $A^2\Sigma-X^2\Pi$ transition of OH (beside the above mentioned R_1 , R_2 heads of the (1,0) transition, there are Q_1 and Q_2 heads of the same vibrational transition, appearing at 281.91 nm and 282.90 nm [26]). Several broad weak peaks are assigned to various vibrational transitions within the $D^2\Sigma-X^2\Sigma$ (e.g. that at 254.85 nm) and/or $E^2\Delta-A^2\Pi$ (e.g. at 259.29 nm) band systems of AlO [26].

The general trends of the absolute intensity variations with time for the spectra between 230 nm and 290 nm (Fig. 4a–c) are the same as those for the 250–850 nm region: The intensities of Al I lines do not change dramatically (if large random fluctuations from one recording to the other are ignored) in the first phase of the process (between 0 and 60 min). They decrease later, first quite significantly (between $t = 60$ and $t = 150$ min), and after 150 much more slowly. They practically disappear at the end of the time interval considered (300 min). The intensities of the species originating from the electrolyte and/or being combinations of the substrate and electrolyte elements (B, AlO) first increase, and later gradually decrease. Only the intensity of OH bands (like that of the Na lines, appearing in low-resolution spectra, as that presented in Fig. 3) does not decrease even after very long duration of the PEO process.

More reliable and interesting information can be drawn if we consider relative, instead of absolute intensities. Let us choose the Al I line(s) around 237 nm as the reference. It is then found that the relative intensities of the electrolyte species, but also that of the 282 nm line, continuously increase with time, whereas the change of intensities of the other Al lines and of the AlO bands is much less pronounced. It can be noticed, however, that all three other Al I lines (257.51 nm, 265.25 nm, and 266.04 nm) increase (with respect to the 237 nm line) in the course of the PEO process. Having in mind that these lines correspond to lower excitation energies than the 237 nm line(s) it can be concluded that the temperature gradually decreases during the discharging process. This is also consistent with the general decrease of absolute

intensities of all species, except of Na I and OH. The dependence of the logarithm of Al I intensity ratios, 257.51/237.31, 266.04/237.31, and 266.04/257.51 on the duration of the PEO process is presented in Fig. 5. We excluded from consideration several recordings with extremely high- and low-intensity spectra. The spectral line intensities were corrected to continuum background. Assuming the existence of the partial LTE, we can use this data to estimate the dependence of the plasma temperature on time. Because of the above mentioned problems caused by the fact that the lines we used are composed of several poorly resolved components, the determination of absolute temperature values based on the data shown in Fig. 5 conjugated with the Einstein transition probabilities published in Ref. [25] was somewhat risky. However, we found that it was at the beginning the PEO process very similar to that determined in our previous study on Al, $T = 8000 \pm 2000$ K, obtained by measuring the intensity distribution within the $v' - v'' = -1$ and -2 band sequences of the $B^2\Sigma^+ - X^2\Sigma^+$ emission transition of AlO [8].

While the determination of absolute temperature values by means of the intensity ratios 257.51/237.31, 266.04/237.31, and 266.04/257.51 is somewhat questionable, as stated above, the change of these ratios gives reliable information about the change of the temperature. Let us consider the first pair of lines. The ratio of their intensities is given simply by

$$\frac{I_{257.51}}{I_{237.31}} = C_{257.51,237.31} \cdot \exp\left(-\frac{E_{257.51} - E_{237.31}}{kT}\right) \quad (1)$$

where $E_{257.51}$ and $E_{237.31}$ are the excitation energies and $C_{257.51,237.31}$ is a constant whose value is determined such that it fulfills the condition

$$\ln C_{257.51,237.31} = \ln\left(\frac{I_{257.51}}{I_{237.31}}\right)_{t=0} - \left(-\frac{E_{257.51} - E_{237.31}}{k \times 8000K}\right). \quad (2)$$

$(I_{257.51}/I_{237.31})_{t=0}$ is the measured intensity ratio at the beginning of the PEO process, when the plasma (electron) temperature is, as above stated about 8000 K. After determining C , the temperature at any moment t can be calculated by means of the formula

$$T = -\frac{E_{257.51} - E_{237.31}}{k \left[\ln\left(\frac{I_{257.51}}{I_{237.31}}\right)_t - \ln C_{257.51,237.31} \right]} \quad (3)$$

The same procedure is applied to the remaining two pairs of lines. Thus we have three formulae, which should produce the same results provided that the partial LTE does exist. In Fig. 6 we present the temperature obtained by means of three formulae of the type (3). In spite of quite large dissipation of individual points, all three sets of points in Fig. 6 clearly indicate that the plasma temperature becomes already after roughly 1 h from the beginning of the process as low as

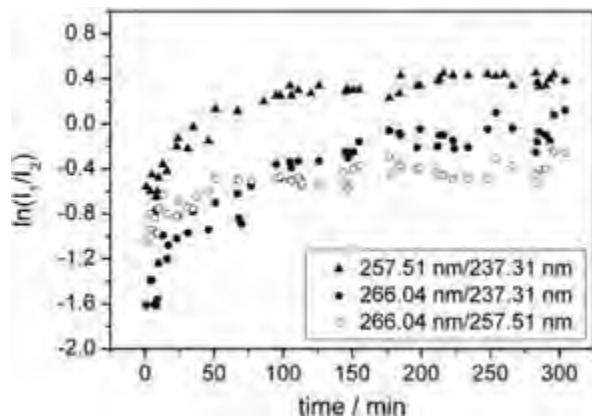


Fig. 5. Logarithm of intensity ratios of Al I spectral lines at 237.31 nm, 257.51 nm, and 266.04 nm as a function of time.

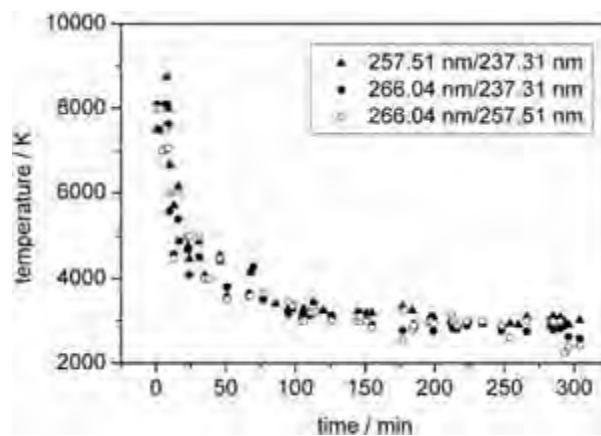


Fig. 6. Time dependence of plasma temperature as determined on by means of intensity ratios of Al I spectral lines at 237.31 nm, 257.51 nm, and 266.04 nm.

3000–4000 K. Note that Hussein et al. [17] did not report on any temperature lowering in the course of the PEO process. Indeed, as mentioned above the time interval considered in Ref. [17] (60 min) is much shorter than that of the present study. The agreement between three sets of results presented in Fig. 6 supports the reliability of the assumption of partial LTE as well as of the value of $T \approx 8000$ at the beginning of the PEO process. Moreover, it indicates that the LTE concept might be extended to different degrees of freedom.

Encouraged by the last conclusion we calculated the equilibrium composition of the plasma containing Al and H, O, and Na with the goal to explain the exceptional behavior of the Na I lines and unexpected intensity evolution of the “Al II line” at 281.65 nm. The approach developed by White et al. [28] and adapted in Ref. [29] to make possible handling charged species was used. The thermochemical data were taken from JANAF Tables [30].

Not knowing the quantitative composition of our plasma, we made the calculations for temperatures between 1000 and 11,000 K at the total pressure of $P_0 = 10^5$ Pa and for the relative contents of Al, H, O, and Na of 1: 1: 0.5: 0.01. These numbers are, of course, arbitrary; we do not include into consideration boron, and the pressure in such systems is believed to be much higher [11]. We will, however, only draw some qualitative conclusions and, based on the experience gathered in our previous studies [8,24], we are confident that they would not be substantially changed if we assumed much more complex plasma models, and particularly if we varied the relative contents of Al, H, O, and Na. The results of calculations for all species whose partial pressures are not negligible in the temperature region considered are presented in Fig. 7.

The partial pressure of Al^+ continuously increases, but even up to $T = 9000$ K the most abundant of the Al-containing species is atomic Al. The partial pressure of AlO is maximal in the temperature range about 4000 K. On the other hand, at high temperatures Na is almost completely present in the form of Na^+ ions. This is the explanation for low intensity of Na I atomic lines at the beginning of the PEO process. On the other hand, the ionic Na lines have excitation energies too high to be observable. If the concentration of sodium in the plasma is relatively high, this has as a consequence an increase of the electron density, which suppresses the ionization of other plasma constituents, in particular of Al atoms.

In Fig. 8 we present the temperature dependence of the quantity $p_i \cdot \exp(-E_i/kT)$, where p_i is the partial pressure of the species i , and E_i is the energy of the upper electronic state for particular emission lines and bands. This quantity should serve for estimation of optimal temperature regions for observing of spectral features in question. It is seen that the intensity of Al I lines decreases with decreasing temperature, while the AlO and OH bands prefer lower-temperature regions (between 3000 K and 5000 K). The continuous increase of the Na lines

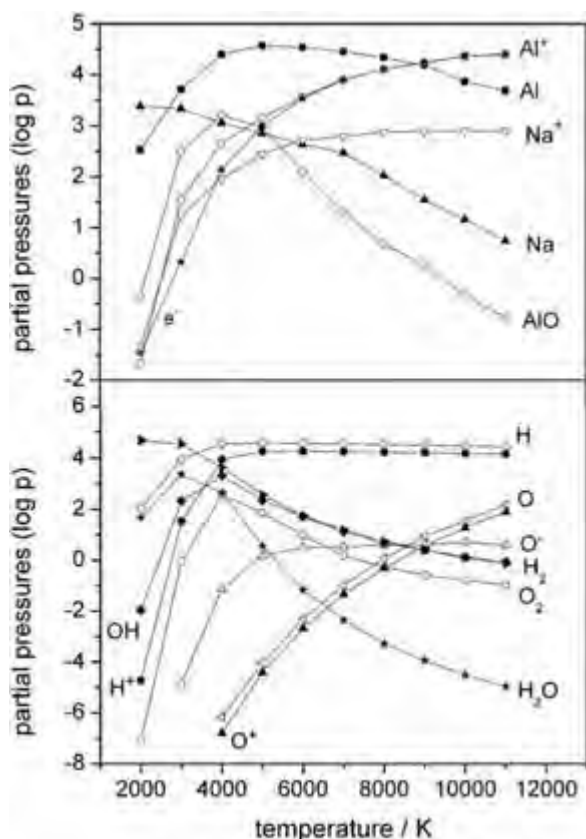


Fig. 7. Equilibrium composition of plasma containing a mixture of aluminum, oxygen, hydrogen and sodium in mole ratio Al, H, O, and Na of 1: 1: 0.5: 0.01 at total pressure of $P_0 = 10^5$ Pa. Top: species involving Al and Na (+ electrons). Bottom: species only involving O and H.

in the course of time can be explained by two facts: The first one is obvious. The partial pressure of the atomic sodium is relatively low at high temperatures and it continuously increases with decreasing temperature (Fig. 7). The function $p_{NaI} \cdot \exp(-E_{NaI}/kT)$ reaches a broad maximum in the lower temperature region (3000–6000 K). The other reason could be increasing amount of all species originating from the solution in the plasma, in course of the anodization process.

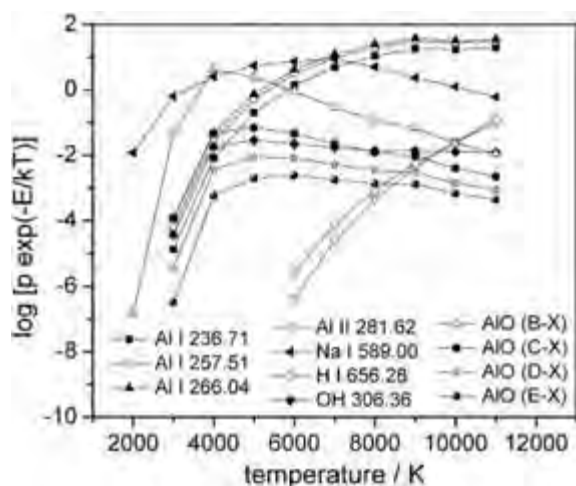


Fig. 8. Computed dependence of function $p_i \cdot \exp(-E_i/kT)$, where E_i is the energy of the upper electronic state for the i th species, of plasma containing a mixture of aluminum, oxygen, hydrogen and sodium in mole ratio Al, H, O, and Na of 1: 1: 0.5: 0.01 at total pressure of $P_0 = 10^5$ Pa.

Particularly interesting is the dependence of the “Al II line” measured at 282 nm and the H_{α} line intensities on time. If we look at Fig. 8, we see that the intensity of the 281.65 nm Al II line should drastically decrease with decreasing temperature. However, our experimental results are not in accordance with this expectation. Thus we conclude that the intensity of the “Al II line measured at 282 nm” is significantly contributed by the surrounding unresolved OH bands making it apparently much stronger than it really is.

A possible explanation for relative lowering of intensity of the Al spectral lines with respect to the features originating from the electrolyte (particularly of the Na lines and OH bands) and estimated decrease of the electron temperature measured by means of the intensity ratios of the Al lines in the late phase of the PEO process is the following one. At thick Al_2O_3 layers with deep channels reaching the surface of the elemental Al, the strength of the electric field in the channels of the Al_2O_3 layer is lowered. A consequence thereof is that in the coating area close to the electrode/electrolyte boundary the electrons have relatively small energy, i.e. the electron temperature is relatively low, favoring the appearance of the Na lines and the OH bands, and having opposite effect on the Al spectral lines (see Figs. 7 and 8). The electrons reach high energy only in the inner parts of the channels, far from the electrode/electrolyte boundary and the intensity of the emission originating from these areas is considerably quenched.

4. Conclusions

The investigations of the morphology and composition of the substrate and the emission spectra recorded during the PEO process at a long-time interval lead to the following conclusions: The complete process may be divided into three phases. In the first phase, before the breakdown, the thickness of the Al_2O_3 layer at the surfaces of the anode is small but it continuously increases with time. The surface is smooth and in the EDS spectrum aluminum is clearly dominating species. In the second phase, lasting much longer (typically one hour) the Al_2O_3 layer becomes relatively thick and a number of small- and middle-size microdischarges cover the coating surface producing on it flat micropores and channels, making the surface in this way less smooth. The EDS spectra taken at different places along the cross section of the anode clearly show the appearance of aluminum in deep layers of the electrode and both aluminum and oxygen in the coating layer. At the beginning of the second phase of the PEO process the emission spectrum is dominated by Al I lines. In the course of time, besides aluminum atomic lines the species originating from the electrolyte, like Na I and H I atomic lines and OH and AIO bands become intense. The microdischarges become gradually larger and they produce deeper and more lasting cracks on the electrode surface. In the third phase of the PEO process (few hours after its beginning) these cracks/channels reach the metal substrate and cause thus irreparable defects of the coating surface.

The optical spectra taken during this phase are characterized by relative lowering of the intensity of aluminum spectral lines and increase of some features originating from electrolyte, like Na and H lines and OH bands. The temperature, as measured by using three pairs of Al I spectral lines, gradually diminishes reaching in the last phase the values typical for the outer-plasma zones (3000–4000 K) according to Klappik's model [13,14].

Acknowledgment

This work is supported by the Ministry of Education and Science of the Republic Serbia under Projects No. 171035 and 172040.

References

- [1] B. Kasalica, I. Belča, S. Stojadinović, M. Sarvan, M. Perić, J. Phys. Chem. C 111 (2007) 12315.
- [2] B. Kasalica, M. Petkovic, I. Belča, S. Stojadinovic, Lj Zekovic, Surf. Coat. Technol. 203 (2009) 3000.

- [3] S. Stojadinovic, R. Vasilic, I. Belca, M. Petkovic, B. Kasalica, Z. Nedic, Lj. Zekovic, *Corros. Sci.* 52 (2010) 3258–3265.
- [4] S. Stojadinovic, R. Vasilic, M. Petkovic, Z. Nedic, B. Kasalica, I. Belca, Lj. Zekovic, *Electrochim. Acta* 55 (2010) 3857.
- [5] J. Jovović, S. Stojadinović, N.M. Šišović, N. Konjević, *Surf. Coat. Technol.* 206 (2011) 24.
- [6] M. Petković, S. Stojadinović, R. Vasilčić, I. Belča, Z. Nedić, B. Kasalica, U.B. Mioč, *Appl. Surf. Sci.* 257 (2011) 9555.
- [7] M. Sarvan, M. Perić, Lj. Zeković, S. Stojadinović, I. Belča, M. Petković, B. Kasalica, *Spectrochim. Acta A* 81 (2011) 672.
- [8] S. Stojadinović, M. Perić, M. Petković, R. Vasilčić, B. Kasalica, I. Belča, J. Radić-Perić, *Electrochim. Acta* 56 (2011) 10122.
- [9] J. Jovović, S. Stojadinović, N.M. Šišović, N. Konjević, *J. Quant. Spectrom. Radiat. Transfer* 113 (2012) 1928.
- [10] B. Kasalica, S. Stojadinović, I. Belča, M. Sarvan, Lj. Zeković, J. Radić-Perić, *J. Anal. At. Spectrom.* 28 (2013) 92.
- [11] A.L. Yerokhin, X. Nie, A. Leyland, A. Matthews, S.J. Doney, *Surf. Coat. Technol.* 122 (1999) 73.
- [12] R.O. Hussein, P. Zhang, X. Nie, Y. Xia, D.O. Northwood, *Surf. Coat. Technol.* 206 (2011) 1990.
- [13] M.D. Klapkiv, *Mater. Sci* 31 (1996) 494.
- [14] M.D. Klapkiv, *Mater. Sci.* 31 (1999) 279.
- [15] C.S. Dunleavy, I.O. Golosnoy IO, J.A. Curran, T.W. Clyne, *Surf. Coat. Technol.* 203 (2009) 3410.
- [16] M.D. Klapkiv, H.M. Nykyforchyn, V.M. Posuvailo, *Mater. Sci.* 30 (1994) 333.
- [17] R.O. Hussein, X. Nie, D.O. Northwood, A. Yerokhin, A. Matthews, *J. Phys. D: Appl. Phys.* 43 (2010) 105203.
- [18] R.O. Hussein, X. Nie, D.O. Northwood, *Mater. Chem. Phys.* 134 (2012) 484.
- [19] M. Petković, S. Stojadinović, R. Vasilčić, Lj. Zeković, *Appl. Surf. Sci.* 257 (2011) 10590.
- [20] S. Stojadinović, J. Jovović, M. Petković, R. Vasilčić, N. Konjević, *Surf. Coat. Technol.* 205 (2011) 5406.
- [21] S. Stojadinović, R. Vasilčić, M. Petković, Lj. Zeković, *Surf. Coat. Technol.* 206 (2011) 575.
- [22] S. Stojadinović, R. Vasilčić, M. Petković, I. Belča, B. Kasalica, M. Perić, Lj. Zeković, *Electrochim. Acta* 79 (2012) 133.
- [23] S. Stojadinović, R. Vasilčić, M. Petković, I. Belča, B. Kasalica, M. Perić, Lj. Zeković, *Electrochim. Acta* 59 (2012) 354.
- [24] S. Stojadinović, M. Perić, J. Radić-Perić, R. Vasilčić, M. Petković, Lj. Zeković, *Surf. Coat. Technol.* 206 (2012) 2905.
- [25] Y. Ralchenko, A.E. Kramida, J. Reader, NIST ASD Team, National Institute of Standards and Technology, Gaithersburg, MD, 2011, [Online].
- [26] E.W.B. Pearse, A.G. Gaydon, *The Identification of Molecular Spectra*, Chapman and Hall, London, 1976.
- [27] M. Outred, M.H. Rummeli, E.N.M. Steers, *J. Anal. At. Spectrom.* 9 (1994) 381–384.
- [28] W.B. White, S.M. Johnson, G.B. Dantzig, *J. Chem. Phys.* 28 (1958) 751–755.
- [29] J. Radić-Perić, M. Perić, *Spectrochim. Acta B* 35 (1980) 297–305.
- [30] JANAF, *J. Phys. Chem. Ref.* 27 (1971) (NIST–JANAF Thermochemical Tables).

RESEARCH

Open Access



LED-based Vis-NIR spectrally tunable light source - the optimization algorithm

M. Lukovic^{1*} , V. Lukovic¹, I. Belca², B. Kasalica², I. Stanimirovic³ and M. Vivic²

Abstract

Background: A novel numerical method for calculating the contributions of individual diodes in a set of light emitting diodes (LEDs), aimed at simulating a blackbody radiation source, is examined. The intended purpose of the light source is to enable calibration of various types of optical sensors, particularly optical radiation pyrometers in the spectral range from 700 nm to 1070 nm.

Results: This numerical method is used to determine and optimize the intensity coefficients of individual LEDs that contribute to the overall spectral distribution. The method was proven for known spectral distributions: "flat" spectrum, International Commission on Illumination (CIE) standard daylight illuminant D65 spectrum, Hydrargyrum Medium-arc Iodide (HMI) High Intensity Discharge (HID) lamp, and finally blackbody radiation spectra at various temperatures.

Conclusions: The method enables achieving a broad range of continuous spectral distributions and compares favorably with other methods proposed in the literature.

Keywords: Algorithmic solution, LEDs, Calibration source, Blackbody, Optical pyrometers

Background

Numerous variants of spectral light sources based on combined radiation of individual LEDs have been reported in the past 15 years [1–4]. Each LED has its own spectral characteristic and contributes to the overall output spectrum in a relatively narrow range. As the number of newly-developed semiconductor light sources increases, covering wider and wider spectral range, this kind of construction becomes increasingly popular [5–7]. This approach allows for the generating a broad range of different output spectral distributions of almost arbitrary shape. This in turn, enables various applications such as calibration of light-measuring instruments, ambient lighting, applications in forensic science, fluorescence applications [8–10], etc.

Special case of light sources based on combined emission from a set of LEDs (where each individual LED has its own spectral distribution) are calibration sources [11–17]. Such instruments often allow for the generation of arbitrary shaped output spectrum. For example, reference [9] describes a LED-based calibration source for an ultra-sensitive spectrometry system used for electro- and

photo-luminescent measurements. However, extensive search through available literature produced only a few readily implementable prescriptions for synthesizing the output spectrum of a LED-based tunable source [15, 17]. The objective of this paper is to explore the possibilities for improving spectrum synthesis methods.

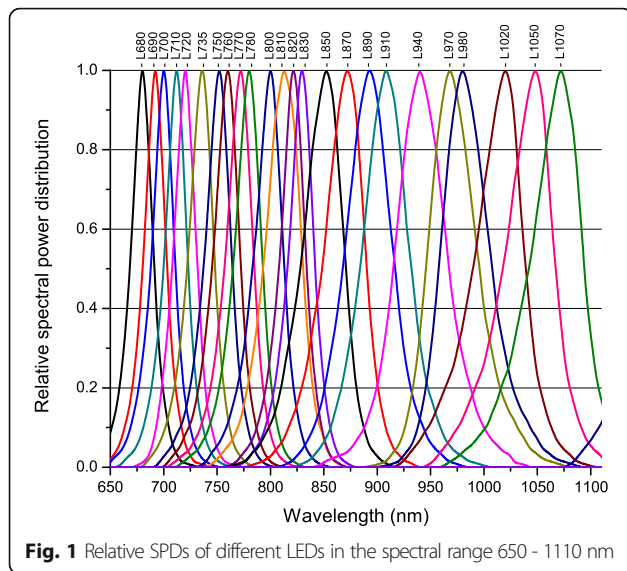
We explore the possibilities of generating various spectral shapes in the very near infrared region (VNIR) using a relatively large number of individual LEDs. It is our belief that the results of this work might be useful to other researchers in this field.

Special emphasis will be placed on generating a simulated "flat" spectrum and blackbody radiation spectra in the 700 - 1070 nm range for the 800 - 1300 °C temperature interval. However, the proposed methodology should be readily applicable to other spectral ranges and/or temperatures [18].

The basic problem of synthesizing the shape of a given spectral profile is determining the intensity of each individual LED that contributes to the overall spectrum. Each LED has a relatively narrow spectral distribution as illustrated in Fig. 1 [19]. In the first approximation, the spectral distribution of a single LED will be assumed to be Gaussian. The synthesized output spectrum is a sum of the contributions from each individual LED's

* Correspondence: milentije.lukovic@ftn.kg.ac.rs

¹University of Kragujevac, Faculty of Technical Sciences, Cacak 32000, Serbia
Full list of author information is available at the end of the article



normalized spectral power distribution (SPD) weighted by a certain factor. This factor in fact corresponds to the current that drives the particular LED, in order to get unity intensity at Gaussian center.

For a given target output spectral profile, it is therefore necessary to mathematically find the combination of values of the coefficients (driving current intensities) that best iterate the target spectrum. An algorithmic solution was developed to achieve this.

The algorithm was initially applied for the synthesis of a flat spectrum, i.e. for producing an output spectrum that has a constant intensity with respect to the wavelength in the given wavelength interval. The “flat” spectrum can be an excellent tool for direct measurements and evaluation of the responsivity function of optical sensors and systems like low-signal intensity measuring spectrometers, photo-multipliers, etc., where standard lamps and black bodies introduce large relative errors due to a great intensity variation (almost two orders of magnitude).

A further refinement of the algorithm was used to synthesize arbitrarily shaped spectrum profiles and in particular to simulate blackbody radiation. Deviation of the synthesized blackbody spectra from the theoretical curve was analyzed in detail. This was done in order to estimate the temperature reading errors when the LED-based source is used as a calibration source for optical pyrometers. A LED-based system that simulates blackbody radiation would be a handy and practical solution for calibrating pyrometers in industrial installations, opposite to large blackbody furnaces.

Methods

As already mentioned, the main purpose of the proposed algorithm for a given number of LEDs is to find the coefficients (weight factors) that multiply the driving

currents of a LED in such way that the summary output spectral profile represents the best possible approximation of the desired output spectral profile.

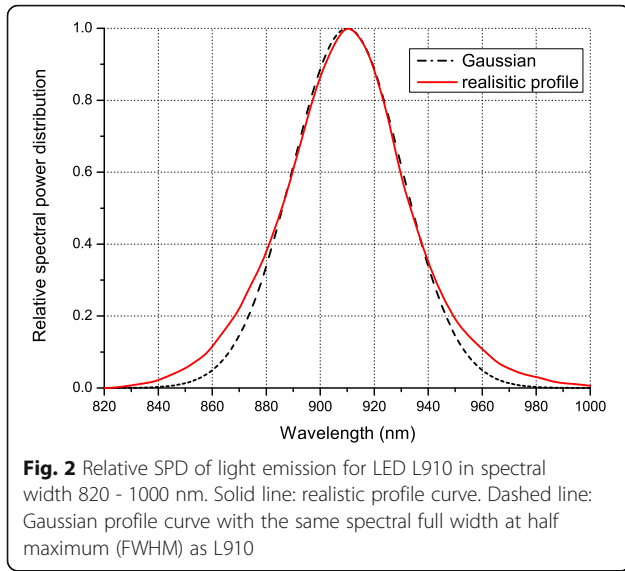
In order to simplify calculations, we assumed that the SPDs of individual LEDs are normalized. In other words, the output intensity for the emission peak of each LED has a unity value. One has to bear in mind that in practical implementations LEDs feature different emission efficiencies. Therefore, the coefficients obtained through simulation need to be multiplied by an appropriate factor that accounts for different LED efficiencies.

Table 1 shows the relative light intensity emitted by individual LEDs per unit current (i.e. emission gain) in the wavelength interval 632-1548 nm. The LEDs used were: L680, L690, L700, L710, L720, L735, L750, L760, L770, L780, L800, L810, L820, L830, L850, L870, L890, L910, L940, L970, L980, L1020, L1050, L1070, L1200, L1300, L1450 and L1550. The labels and the intensity data were adopted from [19]. Figure 2 illustrates the typical SPD of a diode from the set (L910 in this example).

Determining the values of the sought coefficients in linear algebra comes down to solving m equations with n unknown coefficients a_j ($j = 1, \dots, n$) according to (1),

Table 1 Matrix M of relative LED SPDs in the spectral range from 632 nm to 1548 nm with an increment of 4 nm. LEDs: L680, L690, ..., L1550

Wavelength (nm)	LED					
	L680	L690	L700	...	L1450	L1550
632	0.006757	0	0	...	0	0
636	0.013514	0	0	...	0	0
640	0.027027	0	0	...	0	0
644	0.041892	0.006757	0	...	0	0
648	0.067568	0.013514	0.006757	...	0	0
652	0.108108	0.027027	0.02027	...	0	0
656	0.151351	0.041892	0.02973	...	0	0
660	0.22973	0.067568	0.040541	...	0	0
664	0.337838	0.108108	0.060811	...	0	0
668	0.486486	0.151351	0.090541	...	0	0
672	0.689189	0.22973	0.135135	...	0	0
676	0.891892	0.337838	0.189189	...	0	0
680	1	0.486486	0.27027	...	0	0
684	0.891892	0.689189	0.364865	...	0	0
688	0.689189	0.891892	0.5	...	0	0
692	0.445946	1	0.702703	...	0	0
696	0.27027	0.891892	0.905405	...	0	0
700	0.175676	0.689189	1	...	0	0
...
1544	0	0	0	...	0.040541	0.986486
1548	0	0	0	...	0.033784	1



where \mathbf{M} represents the matrix of relative SPDs derived from Table 1, depending on the number of chosen diodes n and the selected spectral bandwidth m .

$$\begin{aligned} a_1 M_{11} + a_2 M_{12} + \dots + a_n M_{1n} &= I_1 \\ a_1 M_{21} + a_2 M_{22} + \dots + a_n M_{2n} &= I_2 \\ &\dots \\ a_1 M_{m1} + a_2 M_{m2} + \dots + a_n M_{mn} &= I_m \end{aligned} \quad (1)$$

The matrix form of (1) is given in (2) and (3), where \mathbf{A} represents a matrix of unknown LED coefficients and \mathbf{I} represent a matrix of targeted intensities. The element M_{ij} of the matrix \mathbf{M} represents the spectral contribution on the i -th wavelength of the j -th LED. The matrix \mathbf{M} has the dimensions $m \times n$ with non-zero elements mainly concentrated along its diagonal. Owing to the fact that $m > n$, mathematical problem (1) is actually an overdetermined system.

$$\begin{bmatrix} M_{11} & M_{12} & \dots & M_{1n} \\ M_{21} & M_{22} & \dots & M_{2n} \\ \dots & \dots & \dots & \dots \\ M_{m1} & M_{m2} & \dots & M_{mn} \end{bmatrix} \cdot \begin{bmatrix} a_1 \\ a_2 \\ \dots \\ a_n \end{bmatrix} = \begin{bmatrix} I_1 \\ I_2 \\ \dots \\ I_m \end{bmatrix} \quad (2)$$

$$\mathbf{M} = \begin{bmatrix} M_{11} & M_{12} & \dots & M_{1n} \\ M_{21} & M_{22} & \dots & M_{2n} \\ \dots & \dots & \dots & \dots \\ M_{m1} & M_{m2} & \dots & M_{mn} \end{bmatrix}; \quad \mathbf{A} = \begin{bmatrix} a_1 \\ a_2 \\ \dots \\ a_n \end{bmatrix}; \quad \mathbf{I} = \begin{bmatrix} I_1 \\ I_2 \\ \dots \\ I_m \end{bmatrix} \quad (3)$$

The optimal solution to this kind of problem can be sought by several different methods (e.g. see [20–24]).

We proposed yet another innovative approach, starting from the following assumptions:

- The target spectral profile is well-defined.
- The interval of the simulated wavelengths is covered by n LED sources.
- Each LED's SPD can be initially approximated by a Gaussian, to accelerate calculations. However, final calculations are performed using real SPDs.
- The contribution of each LED to the summary spectrum is determined by a coefficient a_j ($j = 1, \dots, n$), which is proportional to the driving current of that LED.
- All coefficients a_j must be in the interval $lb_a < a_j < ub_a$. The values of the lower lb_a and the upper ub_a interval boundary depend on the shape of the target.

The system of Eq. (1) in the new approach is solved by allowing for the summed intensities I_1, I_2, \dots, I_m to slightly deviate from the prescribed values of the target intensities $I_{T1}, I_{T2}, \dots, I_{Tm}$. The coefficients a_1, a_2, \dots, a_n are varied within their expected range and for each variation a standard deviation from the target intensities $I_{T1}, I_{T2}, \dots, I_{Tm}$ is calculated and stored. This procedure enables finding of the variation of coefficients a_1, a_2, \dots, a_n that yields the minimum deviation of the combined LEDs spectral distribution from the target SPD. The outline of the proposed optimization algorithm is presented in the flowchart shown in Fig. 3.

Each coefficient a_j is determined with resolution res , which gives a number of possible values for each a_j as:

$$N = (ub_a - lb_a) / res \quad (4)$$

Under these assumptions, it is possible to generate Vr different spectra (variations with repetition):

$$Vr = N^n \quad (5)$$

The criterion for selecting the best variation is minimal standard deviation from the target SPD. Taking into account the spectral range in which optical pyrometers would operate and the purpose for which it would be used, the spectral interval of interest in our research was 700 - 1070 nm. Choosing of the best values for the coefficients a_1, a_2, \dots, a_n by finding the variation that produces the minimum deviation of the synthesized spectrum in mentioned spectral region, was limited by the availability of LEDs on the market. Due to this constraint, we covered the interval by $n = 24$ LED models: L680, L690, L700, L710, L720, L735, L750, L760, L770, L780, L800, L810, L820, L830, L850, L870, L890, L910, L940, L970, L980, L1020, L1050 and L1070. To broaden the dynamic range, a group of four identical devices were used for each diode model. Since we wished to determine the

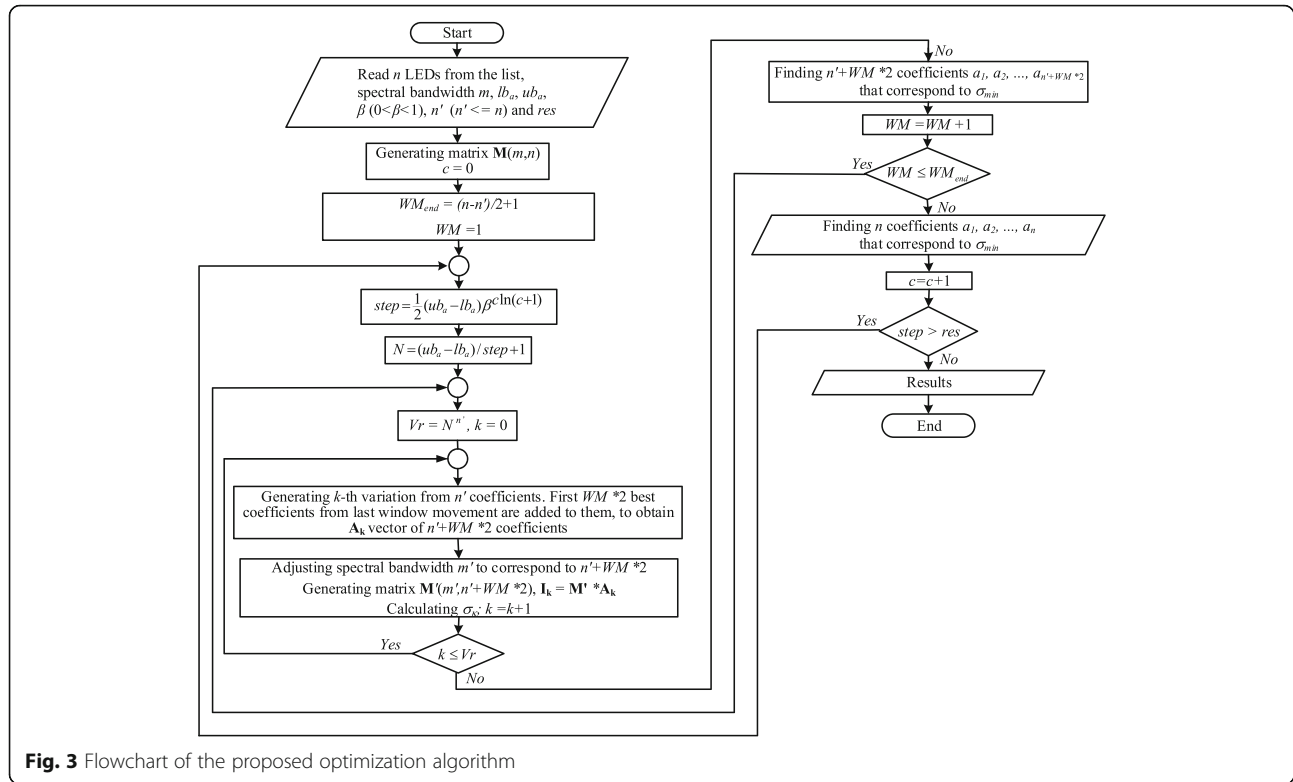


Fig. 3 Flowchart of the proposed optimization algorithm

coefficients accurately to the third decimal place ($res = 0.001$), according to (4) it followed that $N = 4000$. Based on (5), for 24 LED models the overall number of variations was $Vr = 4000^{24}$. The number of variations represented a formidable computing challenge and it was necessary to further reduce it. This was achieved by: (i) reducing the number of possible coefficient values and (ii) reducing the number of diodes that were simultaneously active during the optimization run.

The number of possible coefficient values was reduced by an iterative procedure, where $N = 3$ was kept fixed, while the interval and the resolution were simultaneously decremented.

The reduction in the number of active diodes during optimization was effectively achieved by shortening the wavelength interval for the optimization search. This

procedure started by taking the first n' diodes (arranged by increasing wavelength). The number n' was chosen so that computer optimization over the shortened wavelength interval could be carried out in a reasonable time. The next step involved shifting of the “optimization window” by two spaces to the right. Thus, a new set on n' diodes underwent an optimization run. The coefficients left of the current window remained as calculated in the previous run. The procedure was repeated until the optimization window reached the rightmost diode (the diode with the longest wavelength). Figure 4 is a graphical representation of the procedure.

The search for the coefficients in the optimization window was performed using the following method: three values ($N = 3$) of the coefficients were evaluated for each iteration step and each diode. In the first

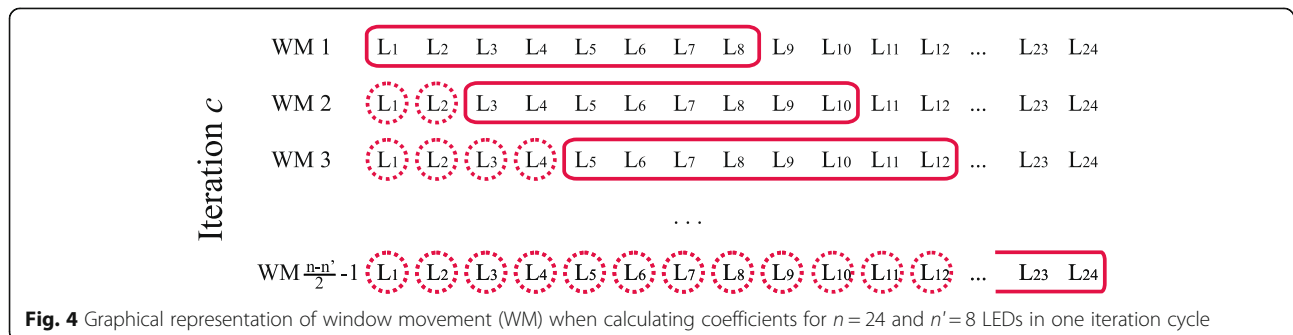


Fig. 4 Graphical representation of window movement (WM) when calculating coefficients for $n = 24$ and $n' = 8$ LEDs in one iteration cycle

iteration ($c = 0$), these values were given by (6) (brackets denote a set of elements) and represented the lower boundary (lb_a), the upper boundary (ub_a), and their arithmetic average.

$$a_{j,c=0} \in \left\{ lb_a ; \frac{ub_a - lb_a}{2} ; ub_a \right\} \quad (6)$$

The computer program evaluated all $3^{n'}$ variations of the coefficients and chose one that yielded a minimal deviation of intensities I_D, I_2, \dots, I_m from the target intensities $I_{T1}, I_{T2}, \dots, I_{Tm}$. For each evaluated coefficient variation, the criterion for minimal deviation was taken to be standard deviation σ_{min} according to (7):

$$\sigma = \sqrt{\frac{1}{m} \sum_{i=0}^m (I_i - I_{Ti})^2} \quad (7)$$

In the next iteration cycle, the value chosen from the previous cycle was surrounded by shorter interval boundaries ($step$) according to (8). The function $f(c)$ depends of the iteration number c . Selection of the $step$ is of utmost importance for convergence. If the $step$ is too narrow, the possibility exists that the real value of the coefficient will be missed. Conversely, if the $step$ is too broad, the number of iterations increases and convergence is too slow.

$$step = \frac{1}{2} (ub_a - lb_a) \cdot f(c) \quad (8)$$

Numerous functions $f(c)$ were tested to find a way to systematically decrease the interval $step$. The simplest of these functions was given by (9).

$$f(c) = \beta^c \quad (9)$$

where β is the fitting parameter, $\beta \in (0, 1)$. However, the best results were achieved with the function given by (10):

$$f(c) = \beta^{c \cdot \ln(c+1)} \quad (10)$$

Consequently, (8) became:

$$step = \frac{1}{2} (ub_a - lb_a) \cdot \beta^{c \cdot \ln(c+1)} \quad (11)$$

After the initial iteration ($c = 0$) and determination of the best variation of the coefficients, the following iterations ($c \geq 1$) were performed in an identical manner, bearing in mind that the three possible values of each coefficient $a_{j,c}$ were chosen from the set given by (12) or, alternatively written, (13). The only condition that needed to be met was that the coefficients from the previous ($c-1$)-th iteration satisfy $lb_a < a_{j,c-1} < ub_a$. If a coefficient from the ($c-1$)-th iteration satisfied $a_{j,c-1} \leq lb_a$, then $a_{j,c}$ in the c -th iteration, it assumed values given by (14).

Finally, if a coefficient from the ($c-1$)-th iteration satisfied $a_{j,c-1} \geq ub_a$, then the three possible values for the c -th iteration were given by (15).

$$a_{j,c} \in \left\{ \begin{array}{l} a_{j,c-1} - step; \\ a_{j,c-1}; \\ a_{j,c-1} + step \end{array} \right\} \quad (12)$$

$$a_{j,c} \in \left\{ \begin{array}{l} a_{j,c-1} - \frac{1}{2} (ub_a - lb_a) \beta^{c \cdot \ln(c+1)}; \\ a_{j,c-1}; \\ a_{j,c-1} + \frac{1}{2} (ub_a - lb_a) \beta^{c \cdot \ln(c+1)} \end{array} \right\} \quad (13)$$

$$a_{j,c} \in \left\{ \begin{array}{l} lb_a; \\ lb_a \left(1 - \frac{1}{2} \beta^{c \cdot \ln(c+1)} \right) + \frac{ub_a}{2} \beta^{c \cdot \ln(c+1)}; \\ lb_a \left(1 - \beta^{c \cdot \ln(c+1)} \right) + ub_a \beta^{c \cdot \ln(c+1)} \end{array} \right\} \quad (14)$$

$$a_{j,c} \in \left\{ \begin{array}{l} ub_a; \\ ub_a \left(1 - \frac{1}{2} \beta^{c \cdot \ln(c+1)} \right) + \frac{lb_a}{2} \beta^{c \cdot \ln(c+1)}; \\ ub_a \left(1 - \beta^{c \cdot \ln(c+1)} \right) + lb_a \beta^{c \cdot \ln(c+1)} \end{array} \right\} \quad (15)$$

With each subsequent iteration, the intervals from which each coefficient was sampled, decreased. The procedure was repeated until all the intervals fall below the sought resolution res . The alternative criterion for the end of simulation was when the best variation of the coefficients' c -th iteration conceded with the best variation from the previous ($c-1$)-th variation.

Among various monotonically decreasing functions that we investigated, $\beta^{c \cdot \ln(c+1)}$ (Fig. 5) proved to be one of the simplest and most efficient for the determining the decreasing step during the iterations. This function

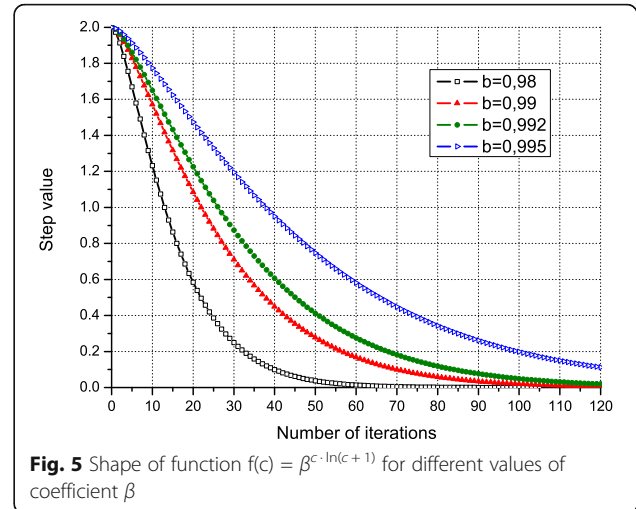


Fig. 5 Shape of function $f(c) = \beta^{c \cdot \ln(c+1)}$ for different values of coefficient β

had a single parameter β that needs to be defined prior to the simulation. The value of β determined the number of iterations. If β was small, the simulation executed quickly but was likely to miss the optimum set of coefficients. A higher value of β yielded better results at the expense of an increased number of iterations. Above certain values of β , the computing time increased with no noticeable improvement in accuracy. For most target spectral profiles, this point of diminishing returns was found to be at $\beta = 0.99$.

The logarithmic part of function (10) prevented the program from executing an unnecessarily large number of steps after a certain resolution was achieved. For example, if the currently achieved resolution is 0.01 ($lb_a = 0$, $ub_a = 4$, $\beta = 0.9$) for function (9), which has no logarithm, it takes 11 more iterations to get to the target resolution of 0.005 (Table 2). By contrast, function (10) achieves a resolution of 0.005 in only three additional steps for the same values of the coefficients (Table 3). We believe that the use of function (10) for this particular optimization problem significantly enhances the efficiency of the simulation and represents one of the most important improvements in comparison to previous algorithms.

One of the common approaches (e.g. see [15, 17]) for estimating how good the overlap is between the LED source and the target SPD is to introduce parameter p :

$$p = \frac{\sum_{380}^{780} \left| \sum_{i=1}^n k_i^{i-1} S_{LED_i}(\lambda) - S_{TARGET}(\lambda) \right|}{\sum_{380}^{780} S_{TARGET}(\lambda)} \quad (16)$$

In our research we also used parameter p along with standard deviation σ as a criterion for choosing the best variation of coefficients a_j .

Table 2 Number of iteration cycles for $res = 0.005$ and function (9)

Iteration number c	Function: $\frac{1}{2}(ub_a - lb_a) \cdot \beta^c$
40	0.014781
41	0.013303
42	0.011973
43	0.010775
44	0.009698
45	0.008728
46	0.007855
47	0.007070
48	0.006363
49	0.005726
50	0.005154

Table 3 Number of iteration cycles for $res = 0.005$ and function (10)

Iteration number c	Function: $\frac{1}{2}(ub_a - lb_a) \cdot \beta^{dn(c+1)}$
15	0.012503
16	0.008428
17	0.005645
18	0.003757

Results and discussion

Simulation results

The proposed algorithm was encoded in the C programming language. The program outputs the best coefficients, the minimum achieved standard deviation, the average value of the intensities, and the maximum deviation of intensities from target values. The values of parameter p for different search steps ($step$) (Table 4) are also contained in the program's output. The results from Table 4 suggest that standard deviation of the maximum intensity deviation rapidly falls as the values of the $step$ decrease.

A separate program written in C# used the text output of the main simulation and generated textual and graphical reports. Running of the actual program for different values of n' showed that it produced the best results for $n' = n$. However, with increasing n' , the simulation time sharply increased and the simulation quickly became infeasible. With the computer currently at our disposal (PC, CPU 3 GHz, 4GB RAM), the limit for simulations of reasonable length was set at $n' = 13$.

Figure 6 illustrates typical simulation results for the "flat" target spectrum. It also indicates the position of the maximum of intensity deviation with respect to the intensity of the targeted spectrum. This particular example of spectrum synthesis serves a dual purpose: (i) the simplicity of the spectrum shape allows for easy analysis of the errors introduced by the algorithm and (ii) a physical device with a flat output spectrum can serve as a very useful tool for calibration and characterization measurements of various types of spectrophotometers.

Table 4 Representative values of minimum standard deviation σ_{min} (7) and parameter p (16) as a function of $step$ for spectral range 700 - 1070 nm, $lb_a = 0$, $ub_a = 4$, $n' = 13$, $\beta = 0.99$

Step	σ_{min}	lav	$maxDev$ (%)	Parameter p
2.000	0.562685	1.166304	112.16	0.470257
1.520	0.369954	1.130186	67.96	0.316449
1.000	0.177625	0.997913	34.04	0.155436
0.517	0.087310	1.026825	26.60	0.068435
0.168	0.040357	1.003645	9.49	0.033639
0.015	0.021147	1.000960	5.95	0.017140
0.001	0.020861	0.999567	5.69	0.016990

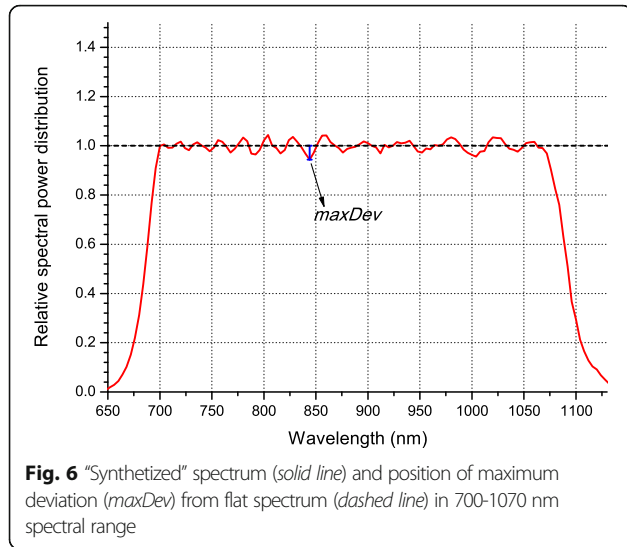
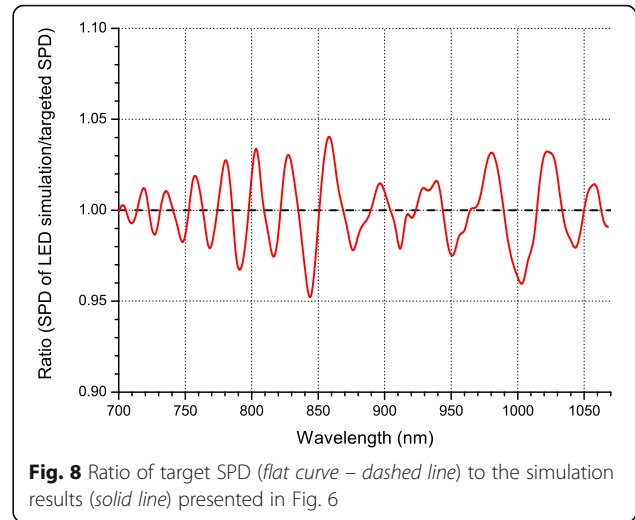
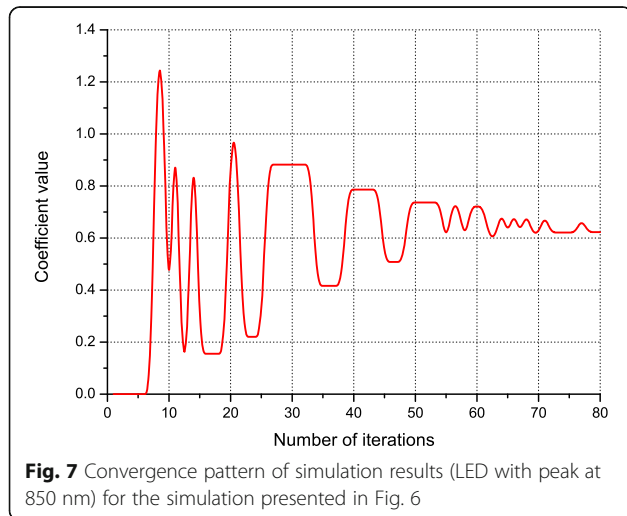


Figure 7 illustrates the typical convergence pattern of a single LED coefficient (L850 in this example), as a function of the iteration number c . Convergence of coefficients of the remaining LEDs in the array follows a similar pattern. It is readily apparent that the coefficient oscillates around the optimal value, with the amplitude of oscillations diminishing as c rises, according to the given logarithmic function (11). The iteration process is repeated until the amplitude of oscillations falls below the sought resolution.

Finally, Fig. 8 is a graphical representation of deviations from the targeted flat curve in the spectral range 700 - 1070 nm of the obtained spectrum. Due to the SPD characteristics of the LEDs used in the simulation (Figs. 1 and 2), deviations were mostly pronounced in the 840 - 860 nm spectral range (~5 %). In the rest of the spectrum they did not exceed 4 %.



Verification of the algorithm using programming package mathematica

The algorithmic solution presented in this paper was also verified with the computer algebra system MATHEMATICA, which is highly applicable to problems that involve symbolic computations. Here, similar to what we did in our algorithmic solution, we adopted that the desired intensities I_1, I_2, \dots, I_m have the same constant value, i.e. $I_1 = I_2 = \dots = I_m = 1$. Also, we added $\varepsilon_i, i = \overline{1, m}$, to the right sides of the equations from (1), where ε_i is the difference between the i -th obtained intensity I_i and the desired light-emitting intensity value I equal to 1 (17, 18). We also considered the limits (19) for the unknowns $a_j, j = \overline{1, n}$.

$$\sum_{j=1}^n a_j M_{ij} = 1 + \varepsilon_i, \quad i = \overline{1, m}, \quad (17)$$

$$-1 \leq \varepsilon_i \leq 1, \quad i = \overline{1, m}, \quad (18)$$

$$0 \leq a_j \leq 4, \quad j = \overline{1, n} \quad (19)$$

The standard deviation of the dispersion of intensities (2) obtained in this way, compared to the desired intensity values equal to 1, needed to be minimized (21):

$$\sigma = \sqrt{\frac{1}{m} \sum_{i=0}^m (I_i - 1)^2} = \sqrt{\frac{1}{m} \sum_{i=0}^m \varepsilon_i^2} \quad (20)$$

Therefore, we obtained the following single-objective optimization problem in (2), which was subjected to (17, 18, and 19).

$$\min \sqrt{\frac{1}{m} \sum_{i=0}^m \varepsilon_i^2} \quad (21)$$

The above-mentioned optimization problem is a variation of the standard linear programming problem; it contains $n + m$ unknowns and is subject to the constraints

determined by m equations and $n + m$ inequalities. There are several methods that can be applied to solve this problem (e.g. see Tikhonov's method [25–28]). The classical approach is to introduce so-called free variables, in order to transform the primal problem to its standard form, containing only equations. After that, the Simplex method is certainly the approach of choice for solving the obtained linear programming problem [29, 30].

A built-in MATHEMATICA function `NMinimize[{f, cons}, vars]` minimizes the objective function f numerically, subject to the constraints provided by the list $cons$, and variables given by the list $vars$. Therefore, the following implementation was considered:

`MinDeviation[M_List] := Module[{m, n, cons, f, vars},`

`{m, n} = Dimensions[M];`

`cons = Union[Table[$\sum_{j=1}^{24} \mathbf{M}[[i, j]] * a[j] == 1 + \text{eps}[i]$, {i, 1, m}],`
`Table[-1 ≤ $\text{eps}[i]$ ≤ 1, {i, 1, m}],`
`Table[0 ≤ $a[j]$ ≤ 4, {j, 1, n}]]];`

`vars = Union[Table[$\text{eps}[i]$, {i, 1, m}], Table[$a[j]$, {j, 1, n}]]];`

`f = Sqrt[$\frac{1}{m * \sum_{i=1}^m (\text{eps}[i]^2)}$];`

`Return[NMinimize[{f, cons}, vars]]];`

The matrix \mathbf{M} , where $\mathbf{M} = (\mathbf{M}_{ij})$, $1 \leq i \leq m$, $1 \leq j \leq n$, is an SPD matrix of the LEDs extracted from Table 1. The dimensions of the matrix are $m \times n$, where m is the selected spectral bandwidth and n is the number of selected diodes. For this matrix, the minimal standard deviation was equal to 0.019792.

Therefore, the maximal absolute declination was obtained for the coefficient $\varepsilon_{37} = 0.0565 = 5.65\%$. Notice that the constraints $-1 \leq \varepsilon_i \leq 1$, $i = \overline{1, m}$ in our mathematical model can be formulated as $-0.06 \leq \varepsilon_i \leq 0.06$, $i = \overline{1, m}$, since the maximal absolute declination never exceeded 6 % in our computations in MATHEMATICA.

The solutions obtained by means of this software showed considerable overlaps with the data received from our method (Table 5).

Comparison with an existing algorithmic solution

In order to evaluate potential merits of the newly-developed algorithm, a comparison was made with the algorithmic solution described in [15]. This previously-published algorithm solely depends on the minimization of parameter p (16). To make a meaningful comparison, the same set of assumptions were made as in [15]: individual LED spectra were taken as having a Gaussian

Table 5 LED coefficients obtained with MATHEMATICA software and our algorithmic solution for a “flat” curve in the spectral range 700 - 1070 nm

Spectral range 700 - 1070 nm			
LED	Coefficient	Mathematica	Our algorithm
L680	a_1	0.758	0.825
L690	a_2	0.020	0.002
L700	a_3	0.558	0.559
L710	a_4	0.260	0.261
L720	a_5	0.411	0.410
L735	a_6	0.560	0.560
L750	a_7	0.346	0.346
L760	a_8	0.328	0.327
L770	a_9	0.185	0.186
L780	a_{10}	0.480	0.479
L800	a_{11}	0.478	0.479
L810	a_{12}	0.401	0.401
L820	a_{13}	0	0
L830	a_{14}	0.354	0.354
L850	a_{15}	0.633	0.633
L870	a_{16}	0.240	0.240
L890	a_{17}	0.606	0.607
L910	a_{18}	0.280	0.279
L940	a_{19}	0.731	0.731
L970	a_{20}	0.012	0.012
L980	a_{21}	0.570	0.569
L1020	a_{22}	0.482	0.482
L1050	a_{23}	0.324	0.325
L1070	a_{24}	0.815	0.815
σ (standard deviation)		0.020860	0.020861
Maximum deviation (%)		5.68	5.69

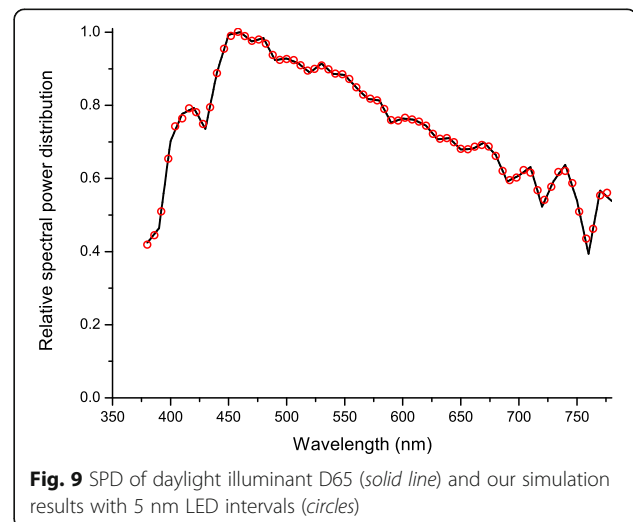
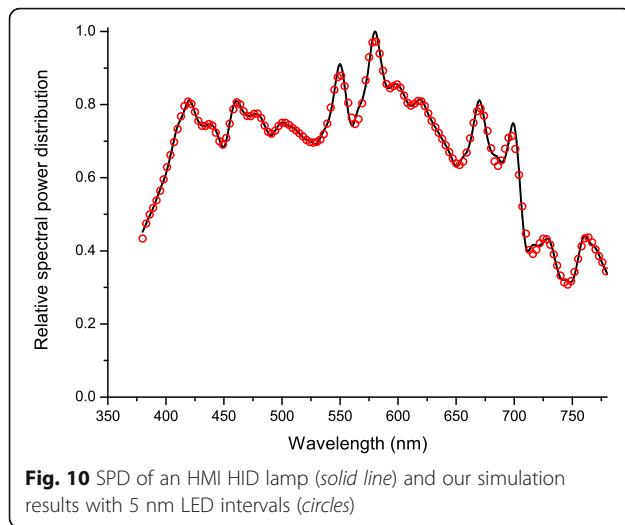


Fig. 9 SPD of daylight illuminant D65 (solid line) and our simulation results with 5 nm LED intervals (circles)



shape with 20 nm FWHM. The simulations were performed for the visible spectrum (380 - 780 nm). The peak wavelengths for a given set of LEDs were chosen to be equidistant at 20, 10 and 5 nm. This effectively means that three sets of 20, 40 and 80 LEDs, respectively, were tested.

The validity of our optimization algorithm was tested for two well-known light spectra: CIE standard daylight illuminant D65 and HMI HID lamp. The simulation results with 5 nm LED intervals for the spectral range 380 - 780 nm are presented in Figs. 9 and 10. The figures show that the proposed algorithm simulated the spectra very accurately.

Table 6 shows a comparison between the results for parameter p of the two different algorithms. It is immediately apparent that the new algorithm yielded somewhat better results (lower value of p) for the 20 nm distance between peaks. For more densely populated sets of LEDs (10 nm and 5 nm inter-peak distance), our algorithm produced the same or slightly higher values of p for the CIE D65 and HMI HID lamps.

Based on the presented comparisons, we believe that the newly-developed algorithm offers some improvements, particularly in the case of sparsely populated sets of LEDs and/or target SPDs with more pronounced peaks.

Simulation of blackbody radiation

One of the SPDs of particular interest in our research was the spectrum of blackbody radiation in VNIR (700 -

1070 nm,) corresponding to blackbody temperatures above 800 °C [31, 32]. As previously mentioned, this kind of source could be useful for the calibration of optical pyrometers that operate in the range from 700 to 1070 nm.

Synthesis of Planck's curve in the given wavelength interval and for the temperatures of interest presented an additional challenge for the algorithm described in this paper. Namely, the spectra cover a very broad dynamic range with orders-of-magnitude different intensities at the endpoints. Our algorithm is limited in the sense that ub_a determines the dynamic range of the synthesized spectrum. To address this problem, the initial values of the lower (lb_a) and upper (ub_a) boundaries for the coefficients a_j were changed. Thus, for $t = 800$ °C boundaries they were $lb_a = 0$ and $ub_a = 4$, while for $t = 1300$ °C ub_a was increased to $ub_a = 30$. It was also determined that for this kind of target SPD, the optimal value of parameter β was $\beta = 0.992$.

Using the modifications mentioned in the previous paragraph, the newly-developed algorithm was applied to a set of real LEDs (using real SPDs for each LED from the set), in order to derive the intensity coefficients a_j and simulate Planck's law curve for temperatures between 800 °C and 1300 °C. Representative results of these simulations are presented in Fig. 11. Numerical results of the simulations for three different temperatures are given in Table 7, along with the values of a_j calculated using MATHEMATICA software. The similarity of the coefficients obtained by our algorithm and MATHEMATICA was yet another verification of the validity of our approach.

In order to verify that the synthesized blackbody spectra can indeed be used for calibrating optical pyrometers, the errors introduced by this non-ideal calibration source needed to be estimated. The basic assumption was that in the 800 - 1300 °C temperature range, the most common sensors used in pyrometry are PIN diodes with typical spectral sensitivity characteristics in the spectral range 600 - 1100 nm, as illustrated in Fig. 12 [33-35].

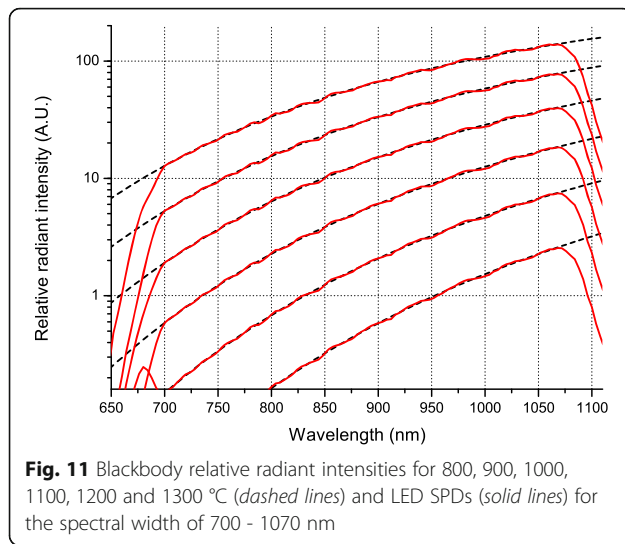
The output voltage of the PIN diode amplifier is proportional to the spectral radiance and for the spectral range (λ_1, λ_2) it depends on the blackbody temperature as:

$$U(T) = C \times \int_{\lambda_1}^{\lambda_2} N(\lambda, T) S(\lambda) d\lambda \quad (22)$$

Table 6 Parameter p for wavelength intervals over the spectral range from 380 nm to 780 nm

LED's peak wavelength intervals		Algorithm with function $\beta^{ch(c+1)}$			I. Fryc, S. W. Brown and Y. Ohno algorithm [15]		
		20 nm	10 nm	5 nm	20 nm	10 nm	5 nm
Parameter p for target light source	CIE D65	0.040	0.004	0.004	0.079	0.004	0.003
	HMI HID	0.042	0.011	0.010	0.074	0.008	0.007

The modeled LED distributions were based on normalized Gaussian functions with FWHM of 20 nm



where: C is the proportionality constant which includes amplification and optical characteristics of a sensor and optical parts of the pyrometer, and $S(\lambda)$ is the spectral responsivity of the PIN diode. The quantity $N_\lambda(\lambda, T)$ is the spectral radiance in the given temperature range and can be derived from Planck's law:

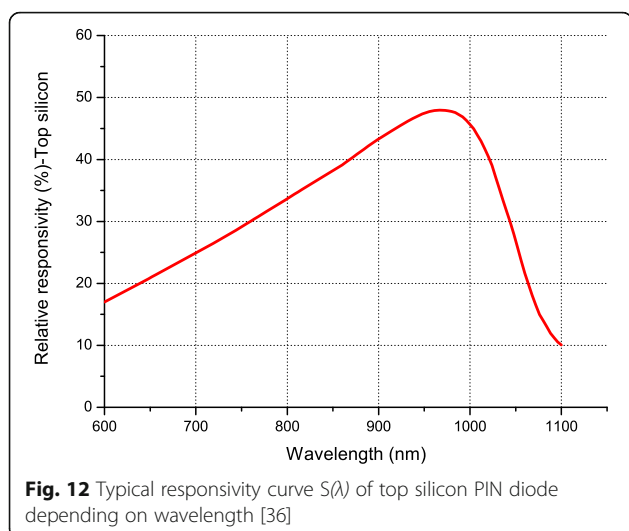
$$N_\lambda(\lambda, T) = \frac{2hc^2}{\lambda^5} \frac{1}{e^{\frac{hc}{\lambda k_B T}} - 1} \quad (23)$$

By substituting the values of the ideal blackbody spectral radiance (23) with radiance values obtained from the simulation, it is possible to calculate the difference in temperature readings between the ideal blackbody and the synthesized calibration source.

Our calculations showed that the errors in temperature readout due to the non-ideality of the LED

Table 7 LED coefficients produced by MATHEMATICA and our algorithmic solutions for different temperatures in the spectral range 700 - 1070 nm

SPD of LEDs for Planck's law in the spectral range 700 - 1070 nm							
LED	Coefficient	Temperature 800 °C		Temperature 1000 °C		Temperature 1200 °C	
		Mathematica	Our algorithm	Mathematica	Our algorithm	Mathematica	Our algorithm
L680	a_1	0.008	0.023	0.290	0.215	2.893	3.770
L690	a_2	0.004	0	0	0.012	0	0
L700	a_3	0.013	0.013	0.319	0.325	2.893	2.727
L710	a_4	0.010	0.010	0.171	0.168	1.497	1.570
L720	a_5	0.014	0.015	0.295	0.297	2.565	2.532
L735	a_6	0.031	0.030	0.542	0.542	4.407	4.417
L750	a_7	0.020	0.021	0.362	0.362	2.916	2.906
L760	a_8	0.030	0.029	0.478	0.479	3.593	3.592
L770	a_9	0.015	0.015	0.233	0.231	1.792	1.786
L780	a_{10}	0.054	0.054	0.834	0.835	6.048	6.051
L800	a_{11}	0.067	0.065	0.955	0.955	6.701	6.700
L810	a_{12}	0.074	0.074	1.008	1.008	6.753	6.754
L820	a_{13}	0	0	0	0	0	0
L830	a_{14}	0.076	0.076	1.003	1.002	6.548	6.547
L850	a_{15}	0.190	0.190	2.298	2.298	14.156	14.156
L870	a_{16}	0.072	0.072	0.930	0.930	5.803	5.804
L890	a_{17}	0.322	0.323	3.401	3.401	19.004	19.004
L910	a_{18}	0.156	0.156	1.681	1.682	9.371	9.371
L940	a_{19}	0.662	0.663	6.226	6.226	31.796	31.796
L970	a_{20}	0	0	0	0	0.029	0.029
L980	a_{21}	0.706	0.706	6.188	6.188	29.972	29.972
L1020	a_{22}	0.802	0.801	6.499	6.498	29.740	29.740
L1050	a_{23}	0.571	0.571	4.617	4.617	20.981	20.981
L1070	a_{24}	2.273	2.273	16.032	16.032	66.493	66.492
σ (standard deviation)		0.022123	0.022124	0.181485	0.181485	0.855000	0.855004
Maximum deviation (%)		4.63	4.65	4.79	4.79	5.00	5.00



source did not exceed $0.1\text{ }^{\circ}\text{C}$ in the temperature range of interest.

Conclusion

This paper examined the feasibility of using a set of LED sources whose cumulative output simulated the “flat” spectrum as well as the blackbody radiation spectrum in the 700 - 1070 nm interval and in the 800 - 1300 $^{\circ}\text{C}$ temperature range. Our research team intends to use the actual composite LED source primarily to calibrate optical pyrometers. We developed a novel algorithm that calculates the intensities of each individual LED in the composite source, in order to achieve the desired output spectral profile. Apart from the “flat” and blackbody spectra, the algorithm was tested on various other target spectral profiles. Especially the “flat” spectrum which is very important as it might enable evaluation and direct measurements of spectral responses of various types of optical sensors and systems. We demonstrated that the proposed algorithm compares favorably with other methods for shaping the output spectral profile of tunable LED light sources. It provides an efficient theoretical base for practical realization of calibration sources.

Abbreviations

CIE: International Commission on Illumination; FWHM: Full width at half maximum; HID: High intensity discharge; HMI: Hydrargyrum medium-arc iodide; LED: Light emitting diode; SPD: Spectral power distribution; VNIR: Very near infrared region

Acknowledgment

The light spectra data of the CIE standard daylight illuminant D65 and HMI HID lamp were obtained from the National Institute of Standards and Technology (NIST), courtesy of Irena Fryc, private communication – Bialystok University of Technology, Poland.

Funding

This ongoing research was funded by the Ministry of Education, Science and Technological Development under project No. 171035.

Authors' contributions

ML developed the proposed algorithm for tunable light sources and carried out all the simulations. VL programmed the algorithm in C and the graphical view of the algorithm in C#. IB proposed the specification and the initial design of the tunable light source. BK provided expert advice. IS programmed the algorithm using Mathematica software. MV coordinated the work and contributed to writing. All the authors have read and approved the final manuscript.

Competing interests

The authors declare that they have no competing interests.

Author details

¹University of Kragujevac, Faculty of Technical Sciences, Cacak 32000, Serbia. ²University of Belgrade, Faculty of Physics, Belgrade 11000, Serbia. ³University of Nis, Faculty of Science and Mathematics, Nis 18000, Serbia.

Received: 13 August 2016 Accepted: 18 October 2016

Published online: 25 October 2016

References

- Ries, H., Leike, I., Muschawek, J.: Optimized additive mixing of colored light-emitting diode sources. *Opt. Eng.* **43**, 1531–1536 (2004)
- Li, Y.-L., Shah, J.M., Leung, P.-H., Gessmann, T., Schubert, E.F.: Performance characteristics of white light sources consisting of multiple light emitting diodes. *Proc. SPIE* **5187**, 178–184 (2004)
- Shang, P. Y., Tang, C. W., Huang, B. J.: Characterizing LEDs for mixture of colored LED light sources, in 2006 Int. Conf. Electron. Mater. Packag. EMAP 2006, (IEEE, Kowloon, 2006)
- Lu, S.S.L.W., Zhang, T., He, S.M., Zhang, B., Li, N.: Light-emitting diodes for space applications. *Opt. Quant. Electron.* **41**, 883–893 (2009)
- Finlayson, G., Mackiewicz, M., Hurlbert, A., Pearce, B., Crichton, S.: On calculating metamer sets for spectrally tunable LED illuminators. *J. Opt. Soc. Am. A Opt. Image Sci. Vis.* **31**, 1577–1587 (2014)
- Hirvonen, J.M., Poikonen, T., Vaskuri, A., Kärhå, P., Ikonen, E.: Spectrally adjustable quasi-monochromatic radiance source based on LEDs and its application for measuring spectral responsivity of a luminance meter. *Meas. Sci. Technol.* **24**, 115201–115208 (2013)
- Mackiewicz, M., Crichton, S., Newsome, S., Gazerro, R., Finlayson, G. D., Hurlbert, A.: Spectrally tunable led illuminator for vision research, in Conf. Colour Graph. Imaging, Vision, CGIV 2012, (Society for Imaging Science and Technology, Amsterdam, 2012)
- Kolberg, D., Schubert, F., Lontke, N., Zwigart, A., Spinner, D.M.: Development of tunable close match LED solar simulator with extended spectral range to UV and IR. *Energy Procedia* **8**, 100–105 (2011)
- Kasalica, B.V., Belca, I.D., Stojadinovic, S.D.J., Zekovic, L.J.D., Nikolic, D.: Light-emitting-diode-based light source for calibration of an intensified charge-coupled device detection system intended for galvanoluminescence measurements. *Appl. Spectrosc.* **60**, 1090–1094 (2006)
- O'Hagan, W.J., McKenna, M., Sherrington, D.C., Rolinski, O.J., Birch, D.J.S.: MHz LED source for nanosecond fluorescence sensing. *Meas. Sci. Technol.* **13**, 84–91 (2002)
- Fryc, I., Brown, S.W., Ohno, Y.: A spectrally tunable LED sphere source enables accurate calibration of tristimulus colorimeters. *Proc. SPIE* **6158**, 61580E (2004)
- Brown, S.W., Santana, C., Eppeldauer, G.P.: Development of a tunable LED-based colorimetric source. *J. Res. Natl. Inst. Stand. Technol.* **107**, 363–371 (2002)
- Fryc, I., Brown, S.W., Eppeldauer, G.P., Ohno, Y.: LED-based spectrally tunable source for radiometric, photometric, and colorimetric applications. *Opt. Eng.* **44**, 111308–111309 (2005)
- Burgos, F. J., Perales, E., Herrera-Ramírez, J. A., Vilaseca, M., Martínez-Verdú, F. M., Pujol, J.: Reconstruction of CIE standard illuminants with an LED-based spectrally tuneable light source, in 12th Int. AIC Congr. AIC **2013**, (2013)
- Fryc, I., Brown, S.W., Ohno, Y.: Spectral matching with an LED-based spectrally tunable light source. *Proc. SPIE* **5941**(594111), 300–308 (2005)
- Brown, S.W., Rice, J.P., Neira, J.E., Johnson, B.C., Jackson, J.D.: Spectrally tunable sources for advanced radiometric applications. *J. Res. Natl. Inst. Stand. Technol.* **111**, 401–410 (2006)
- Yuan, S.J., Huimin Yan, K.: LED-based spectrally tunable light source with optimized fitting. *Chinese Opt. Lett.* **12**, 32301 (2014)

18. Hsu, C.-W., Hsu, K.-F., Hwang, J.-M.: Stepless tunable four-chip LED lighting control on a black body radiation curve using the generalized reduced gradient method. *Opt. Quant. Electron.* **48**, 1–8 (2016)
19. Lasertechnik, R.: Roithner Lasertechnik - LEDs. 2014, <<http://www.roithner-laser.com/led.html>> Accessed 9 Apr 2014
20. Van Benthem, M.H., Keenan, M.R.: Fast algorithm for the solution of large-scale non-negativity-constrained least squares problems. *J. Chemom.* **18**, 441–450 (2004)
21. Chalmers, A., Soltic, S.: Light source optimization: spectral design and simulation of four-band white-light sources. *Opt. Eng.* **51**, 044003–1 (2012)
22. Kim, H., Park, H., Eldén, L.: Non-negative tensor factorization based on alternating large-scale non-negativity-constrained least squares, in *Proc. 7th IEEE Int. Conf. Bioinforma. Bioeng.* (BIBE, Boston, 2007)
23. Bro, R., Jong, S.: A fast non-negativity-constrained least squares algorithm. *J. Chemom.* **11**, 393–401 (1997)
24. Rokhlin, V., Tygert, M.: A fast randomized algorithm for overdetermined linear least-squares regression. *Proc. Natl. Acad. Sci.* **105**, 13212–13217 (2008)
25. Lampe, J., Voss, H.: Large-scale Tikhonov regularization of total least squares. *J. Comput. Appl. Math.* **238**, 95–108 (2013)
26. Golub, G.H., Hansen, P.C., O'Leary, D.P.: Tikhonov regularization and total least squares. *Siam J. Matrix Anal. Appl.* **21**, 185–194 (1999)
27. Wei, Y., Zhang, N., Ng, M.K., Xu, W.: Tikhonov regularization for weighted total least squares problems. *Appl. Math. Lett.* **20**, 82–87 (2007)
28. Beck, A., Ben-Tal, A.: On the solution of the Tikhonov regularization of the total least squares problem. *SIAM J. Optim.* **17**, 98–118 (2006)
29. Nash, J.C.: The (Dantzig) simplex method for linear programming. *Comput. Sci. Eng.* **2**, 29–31 (2000)
30. Forrest, J.J., Goldfarb, D.: Steepest-edge simplex algorithms for linear programming. *Math. Program.* **57**, 341–374 (1992)
31. Planck, M.: The theory of heat radiation. *Search* **30**, 85–94 (1914)
32. Chandrasekhar, S.: Radiative Transfer, in *Energy* (Dover Publication Inc, New York, 1960)
33. Photonics H.: Characteristics and use of infrared detectors, Small, 43 (2004)
34. Bellotti, E., D'Orsogna, D.: Numerical analysis of HgCdTe simultaneous two-color photovoltaic infrared detectors. *IEEE J. Quantum Electron.* **42**, 418–426 (2006)
35. Rogalski, A.: Infrared detectors: an overview. *Infrared Phys. Technol.* **43**, 187–210 (2002)
36. OSI Optoelectronics: Two Color Sandwich Detectors. Silicon Photodiodes, 2015, <<http://www.osioptoelectronics.com/standard-products/silicon-photodiodes/two-color-sandwich-detectors.aspx>> Accessed 2 Apr 2016.

Submit your manuscript to a SpringerOpen[®] journal and benefit from:

- Convenient online submission
- Rigorous peer review
- Immediate publication on acceptance
- Open access: articles freely available online
- High visibility within the field
- Retaining the copyright to your article

Submit your next manuscript at ► springeropen.com

The anomalous sodium doublet D_2/D_1 spectral line intensity ratio – a manifestation of CCD's presaturation effect

Cite this: *J. Anal. At. Spectrom.*, 2013, **28**, 92

Bećko Kasalica,^a Stevan Stojadinović,^a Ivan Belča,^a Mirjana Sarvan,^a Ljubiša Zeković^a and Jelena Radić-Perić^{*b}

In this paper we present the results of intensity measurements of D_1 (589.5224 nm) and D_2 (588.9950 nm) sodium doublet spectral lines emitted from a short-lifetime plasma randomly appearing across the aluminum anode surface during its electrolytic oxidation from the water solution of boric acid with sodium tetraborate. We found that the D_2 to D_1 intensity ratios were not constant, varying from 2 to 1.2. Assuming that the plasma is in local thermal equilibrium it is expected that the intensity ratio of sodium doublet components equals the ratio of the statistical weights of the atomic sublevels corresponding to the electronic transitions (D_1 : $3^2P_{1/2}-3^2S_{1/2}$, D_2 : $3^2P_{3/2}-3^2S_{1/2}$) i.e. 2. After detailed analyses of a series of spectra obtained by applying different detection parameters, like exposure time, slit width, detection mode, and number of accumulations, we attributed the anomalous D_2/D_1 intensity ratio to the effect of approaching a saturation condition of the charge coupled device detector and thus to an early indication of saturation occurrence.

Received 20th June 2012

Accepted 24th October 2012

DOI: 10.1039/c2ja30239j

www.rsc.org/jaas

Introduction

Plasma electrolytic oxidation (PEO) of valve metals like Al, Ti, Zr, Ta, *etc.* is a processing technique in which surfaces of metals are transformed into oxide coatings.¹ The thickness of the coating film varies from tens to hundreds of micrometers, which is influenced by the processing parameters like power supply, electric field strength and the type of the metals and electrolytes used in the PEO process. In the conventional electrolytic oxidation process, the oxidation of the metal is a consequence of electrochemical reactions in the electrolyte (one phase) and on the electrode (the other phase), including the phase-boundary processes. In the PEO processing, due to dielectric breakdown of an anode oxide film under high electric field, a plasma state is generated in the form of visible microdischarges or (plasma) sparks. They are of short duration, typically of a few microseconds, appearing stochastically in time and in space (on the surface of the coating). The oxidation mechanism becomes now more complex, including also plasma chemical reactions.² Due to these plasma processes, the roughness of the coating as well as its morphology, the coating microstructure and composition are modified to some extent, which can be controlled by process parameters.^{3,4}

The investigation and characterization of PEO microdischarges (plasmas) are important steps for understanding of the PEO process. In a number of papers the results of optical emission spectroscopic studies of plasma generated during the PEO process have been presented.^{5–8} In these studies the recorded optical emission spectra have been used to determine the plasma composition. Based on the identification of a number of atomic spectral lines (*e.g.* of Al, Mg, H, O, Na, K, Si, *etc.*), ionic lines (*e.g.* of Al, Si, *etc.*), and molecular bands (OH, AlO, MgO, *etc.*), the presence of particular elements, originating from the coating and/or electrolyte, as well as of their predominant forms (atomic, ionic, molecular) in the PEO plasma has been proven.

In another group of papers, the recorded emission spectra have been used to determine plasma parameters like temperature and electron density. Under assumption of a local thermal equilibrium (LTE), the spectral line intensity ratio method has been applied to obtain the (electron) temperature. For this purpose, different spectral lines can be used, as for example hydrogen Balmer,⁵ Al and Mg lines.⁶ In ref. 9 and 10, the plasma temperature has been obtained from the AlO and MgO emission molecular bands. The plasma electron density can be determined from the analysis of profiles of different spectral lines, as it was done for PEO plasmas in ref. 11 using hydrogen Balmer lines. Further, the recording of the PEO spectra can be carried out continuously in time, such that the so-obtained spectra can be correlated with the time evolution of the PEO process and can be used to monitor the PEO process, too, as for example in ref. 12.

^aUniversity of Belgrade, Faculty of Physics, Studentski trg 12–16, 11000 Belgrade, Serbia

^bUniversity of Belgrade, Faculty of Physical Chemistry, Studentski trg 12–16, 11000 Belgrade, Serbia. E-mail: len@ffh.bg.ac.rs; Fax: +381-11-2187133; Tel: +381-11-3336632

The necessary condition for performing all the above-mentioned tasks is to record “good” spectra in the “proper” way. “Good” spectra means the spectra with a sufficiently large ratio of spectral lines/band intensity to noise, accompanied with well resolved spectral lines. The “proper” way means that we should pay attention to the properties of the detection device and choose the correct mode for collecting the signal in order, *e.g.*, to avoid the saturation of signals.

In this paper we present the results of intensity measurements of D_1 (589.5224 nm) and D_2 (588.9950 nm) sodium doublet spectral lines emitted from a PEO plasma during the aluminum oxidation from a water solution of boric acid with sodium tetraborate decahydrate. We found that the sodium D_2 to sodium D_1 intensity ratios, D_2/D_1 , were not constant, varying from 2 to 1.2. If the PEO plasma is in LTE this intensity ratio should be constant and equal to the ratio of the statistical weights of the atomic sublevels corresponding to the electronic transitions (D_1 : $3^2P_{1/2}-3^2S_{1/2}$, D_2 : $3^2P_{3/2}-3^2S_{1/2}$) *i.e.* 2.

Anomalous intensity ratios within spectral multiplets is a well known phenomenon. It has been observed in spectra of early type stars,¹³ in comet spectra,¹⁴ in the exosphere of the planet Mercury,¹⁵ in sodium fluorescence spectra (induced by a pulsed tunable dye laser) in flames,¹⁶ in high-density laser produced plasma¹⁷ but also in mesospheric night glow.¹⁸ Anomalous ratios within multiplet components may reflect the optical properties of particular plasma and can be a consequence of various mechanisms which cause the perturbation of the LTE. They are a typical characteristic of optically thick plasmas.¹⁹ In that case the effects of reabsorption take place, the radiation field influences the population of levels, *etc.*, as a consequence the excited levels are not populated according to their statistical weights and the Boltzmann law. So, in some papers, the cause for the anomalous sodium D_2 to D_1 intensity ratio has been attributed to the fact that the particular plasma is optically thick.¹⁷ In ref. 13, the anomalous behavior of sodium doublet components emitted from early type stars has been explained by the inhomogeneity of large (interstellar) clouds where the sodium emission originates from. It has also been stressed that the sodium D_2/D_1 intensity ratio tends to be much closer to 2 for the weaker lines than for the stronger ones.

Experimental

The PEO process was performed on high purity cold-rolled aluminum (99.999%, obtained from Goodfellow) samples of 25 mm × 7 mm × 0.12 mm. The surface of aluminum was degreased in ethanol using an ultrasonic cleaner and dried in a warm air stream. The anodic oxidation process was carried out in a 100 ml volume electrolytic cell with flat glass windows. Platinum wires were used as cathodes and the electrolyte was thermostatted at 20 °C. During anodization the electrolyte circulated through the chamber–reservoir system, and the control temperature sensor was suited by the sample. The anodization of aluminum occurred in a water solution of boric acid with sodium tetraborate decahydrate (0.1 mole H_3BO_3 and 0.05 mole $Na_2B_4O_7 \cdot 10H_2O$) as an electrolyte. The electrolyte was prepared with double distilled deionized water and PA grade

chemical substances. The PEO process took place at the constant current density of 10 mA cm^{−2} achieved by a highly stabilized power supply.

It is not a simple task to record optical emission spectra of PEO plasmas because of their random appearance across the anode surface, short lifetimes and usually low intensities. Besides, an anodizing process is time dependent and by recording spectra continuously in time, the evolution of the PEO process can be observed. Because of that, an optic-detection system with improved sensitivity has been developed.²⁰ The emission spectra of PEO microdischarges have been recorded by projecting a small area of the anode surface onto the entrance slit of the spectrograph, in the ratio of 1 : 1, Fig. 1. In order to collect and to focus the highest possible extent of the emitted light on the spectrometer slit, a collimating system consisting of a large-aperture achromatic spherical concave lens has been used. The collecting and focusing of the light on the grating have been performed using a set of flat and spherical concave mirrors, and a similar optics has been applied for the illumination of the Intensified Charge Coupled Device (ICCD) detector,^{21–24} as the most important part of this optic-detection system. A very sensitive PI-MAX ICCD cooled camera with high quantum efficiency, manufactured by Princeton Instruments, has been used. The CCD chip consists of 1024 × 256 pixels, approximately 26 μm × 26 μm each. To reduce the dark current, the CCD chip was cooled at −40 °C using Peltier devices. The real time images of the PEO plasmas have been taken with a video camera Sony DCR-DVD110 (800k pixels CCD, 40 × optical zoom and 40 mm lens filter). A reconstructed “Rank-Hilger” spectrometer with a diffraction grating of 1200 grooves per mm was used for spectra detection. Its linear dispersion is 0.07 nm per pixel, with spectral resolution in the first grating order of about 1200.

Because of the nature of the PEO plasma, the intensities of spectra are in general rather low. An increase in the spectral intensities can be achieved by choosing an appropriate combination of spectra-recording parameters like the slit width (d), exposure time (E), and by accumulation (A) of signals. The

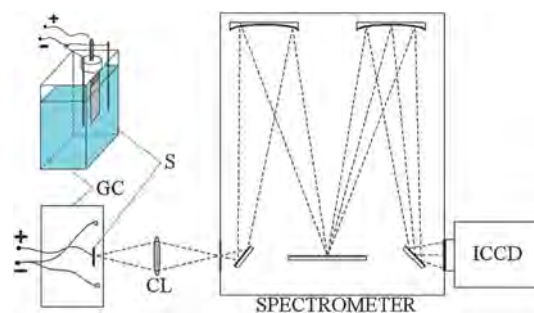


Fig. 1 Schematic diagram of the experimental set up: the electrolytic cell consists of two electrodes, platinum cathodes (−) and aluminum anode (+), in a glass container (GC) with a particular electrolyte solution; a very small area (0.07 mm × 6.7 mm) of the aluminum anode surface (S) is projected via spherical concave lens (CL) onto the slit of a spectrometer. Spectra have been detected using an intensified charge couple device (ICCD) without applying the micro-channel plate (MCP).

accumulation represents (computer) summing of A distinct signals obtained successively over a definite exposure time. The accumulation number, A , can be varied, from one ($A = 1$) to several hundreds. Thus the spectra can be recorded and presented in two manners. The first procedure (first mode) implies the recording of spectra over a certain longer exposure time. The other way (second mode, or accumulation mode) is to record spectra A times (usually $A \gg 1$) over a certain shorter exposure time and after that to accumulate the results.

The intensity of the spectral lines measured in our experiments depended not only on the particular choice of technical parameters (like the time of recording with respect to the beginning of anodization, exposure time, slit width, measuring mode, possible filters applied to reduce the light intensity) but also showed stochastic behavior. For this reason we repeated each experiment with a fixed set of these parameters several (between five and few hundreds) times. (An analogous procedure was applied in our previous studies on Al and Mg.^{9,10,25}) While generally being roughly linearly correlated with the exposure time and/or the accumulation number, the spectral line intensities showed relatively large dispersion with respect to the mean value of several measurements carried out under the same conditions. In extreme cases, appearing usually in one or two of ten experiments, particular peaks were up to one order of magnitude stronger or weaker than the mean value. In the following text we discuss our results primarily in terms of peak intensities (when working in the first mode) and the intensities divided by the number of accumulations (second mode).

All measurements described in the present study were performed without applying the microchannel plate (MCP) normally serving to intensify the signals, because the results of some previous studies^{26,27} had shown that this part of the device had been responsible for nonlinear response of ICCDs. To avoid confusion, from now on, we shall denote our detection device by CCD (instead of ICCD).

Results and discussion

In order to find an explanation for the anomalous sodium D_2/D_1 intensity ratio, found in a number of our spectra, we systematically investigated the influence of the detection parameters mentioned above on the sodium D_1 and D_2 spectral line intensities.

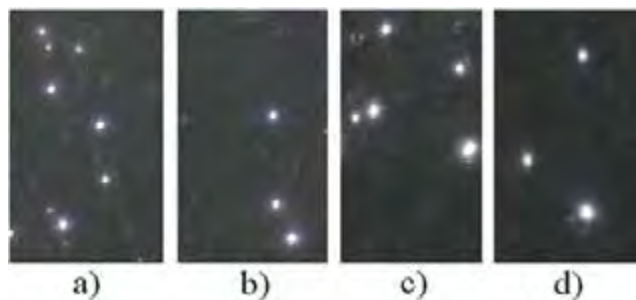


Fig. 2 Real time images of microdischarges appearing at different times t of the anodizing process: (a) 15 min; (b) 30 min; (c) 60 min; and (d) 120 min.

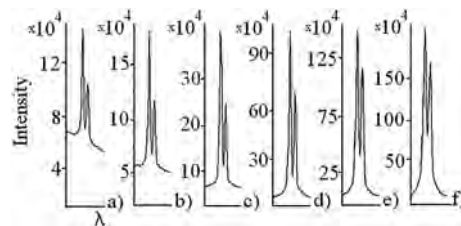


Fig. 3 Sodium D_2 and D_1 emission spectral lines recorded at different times t of the anodizing process: (a) 5 min; (b) 12 min; (c) 43 min; (d) 94 min; (e) 142 min; and (f) 256 min.

At the beginning, we present in Fig. 2 the real time images of PEO microdischarges corresponding to different times of the anodizing process, to illustrate the main PEO-plasma features. The PEO plasmas become visible at about 20 s after the beginning of the anodizing process, their size becomes larger during the PEO process, while their number reduces. They have an average cross-section area of 0.05 mm^2 .

In Fig. 3, six particular spectra involving sodium D_1 and D_2 spectral lines are presented. These spectra have been recorded at different times of the anodizing process *e.g.* at $t_1 = 5 \text{ min}$, $t_2 = 12 \text{ min}$ *etc.* (t denotes the anodizing time; $t = 0$ is the beginning of anodization) with the exposure time of 1 s, with 50 accumulations and the slit width of 0.075 mm . The intensity of sodium spectral lines increases with increasing anodizing time. It is noticeable that the D_2/D_1 intensity ratios are not constant. They vary from the value close to 2 [cases (a and b)] to 1.2 [case (f)]. As it will be shown below, we ascribe this tendency to the continuously more expressed nonlinearity of the CCD response with increasing spectral line intensities.

Particular difficulties in spectral measurements of the present kind are caused by some inherent characteristics of the PEO plasma, like its random appearance across the anode surface and its short lifetime. A consequence thereof is that the spectral features recorded are in general of low intensity (if they appear at all) and of poor reproducibility. Both of these drawbacks can be diminished by using longer exposure times and/or larger slit widths. This is illustrated in Fig. 4a and b. We present in Fig. 4a 70 records and in Fig. 4b 20 records (extracted of totally 300 ones) of the PEO plasma luminescence involving sodium D_1 and D_2 spectral lines. These spectra were recorded at $t = 183 \text{ min}$ after the beginning of the PEO without accumulation of signals ($A = 1$, mode one). In the first case (Fig. 4a) a narrow slit ($d = 0.075 \text{ mm}$) and a relatively short exposure time ($E = 0.05 \text{ s}$) were used, and in the second case (Fig. 4b) we chose a moderate slit width ($d = 0.15 \text{ mm}$) and longer exposure time ($E = 0.3 \text{ s}$). In the spectra presented in Fig. 4a sodium spectral lines are observed in only 6 records of 70 presented (an analysis of all 300 records gives a yield of 9%) and they are characterized by quite different intensities. The yield of observed sodium emission in spectra recorded with longer exposure time (Fig. 4b) is much higher (50–60%), and, naturally, higher are also the line intensities. We analyze now separately the influence of the slit width on the intensity and shape of the sodium spectral lines. The increase of the slit width results in a decrease of resolution

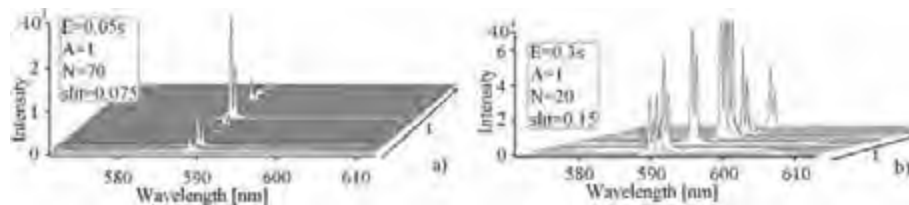


Fig. 4 Successively recorded emission spectra of PEO plasma around sodium D_1 and D_2 spectral lines: (a) spectra taken with low exposure time (0.05 s) and narrow slit (0.075 mm) and (b) spectra taken with longer exposure time (0.3 s) and wider slit (0.15 mm).

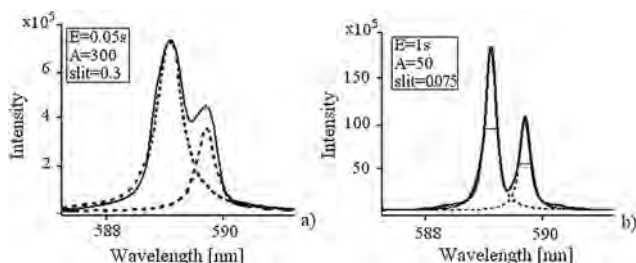


Fig. 5 Sodium D_2 and D_1 emission spectral lines: (a) recorded with a wider slit (0.3 mm) and short exposure time (0.05 s): — before deconvolution, --- after deconvolution and (b) recorded with a narrow slit width (0.075 mm) and longer exposure time (1 s): — before deconvolution, --- after deconvolution.

of the spectral lines and in an increase of their intensities. In some cases the sodium lines presented in Fig. 4b are even saturated – they appear as peaks with flat “cut” maximum.

In Fig. 5a are presented D_2 and D_1 lines recorded with a relatively broad slit of 0.3 mm, obtained in the accumulation

mode ($A = 300$) with short exposure times ($E = 0.05$ s). Let us first note that the background in our experiments is either the same for the both lines (because of their mutual vicinity) or is a very slowly varying linear function of the wavelength, and in general it is much less intense than the lines [1–2% in the first mode (without accumulation) and typically about 5% in the second (accumulation) mode]. Consequently, it can be easily subtracted from the measured spectral lines. The intensity ratio of the unresolved spectral lines (solid curve) equals (when the background is subtracted) 1.66. However, after applying a deconvolution, using Lorentzian fit, the intensity ratio of the resolved sodium lines nearly yields the theoretical value 2. However, if we deconvolute the sodium lines detected using a narrow slit ($d = 0.075$ mm) and longer exposure time ($E = 1$ s), Fig. 5b, the deviation of D_2/D_1 intensity ratios from 2 still remains ($D_2/D_1 = 1.3$). Note that the half-width of both lines is practically the same, with a consequence that the ratio of the areas below the lines (after deconvolution) equals the ratio of their intensities. Thus in order to avoid the artifacts in relative

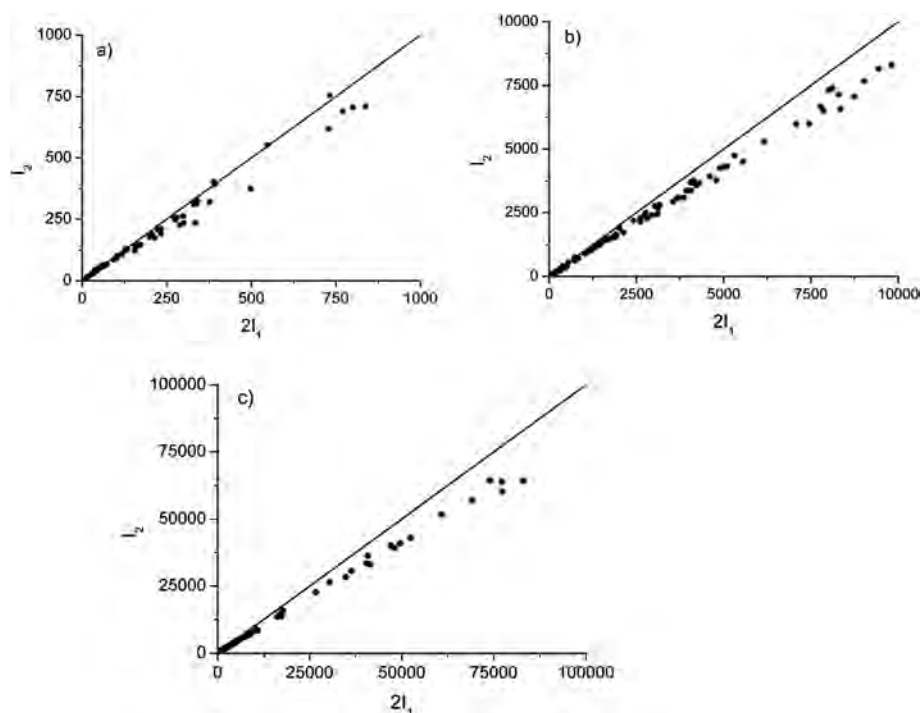


Fig. 6 Correlation between the intensity of sodium D_2 spectral line and that of D_1 line multiplied by two. In the cases where the experiments are carried out in the second mode, the intensities are divided by the accumulation number A . (a) Intensity range 0–1000; (b) 0–10 000; and (c) 0–100 000.

line intensities we carried out all the following experiments using a narrow slit, $d = 0.075$ mm.

In order to investigate the influence of the exposure time on intensities of D_1 and D_2 spectral lines and particularly on D_2/D_1 intensity ratios, we recorded a series of spectra with longer exposure times ($E = 60$ s, 20 s, 10 s, 1 s, and 0.4 s) and without accumulation, and another series of spectra with shorter exposure times (0.2 s, 0.1 s and 0.05 s) with several hundred accumulations. The results of these measurements are presented in Fig. 6a–c. We show the correlation between the intensity of D_2 spectral line and D_1 line intensity multiplied by two. In the cases where the experiments are carried out in the second mode, the intensities are divided by the accumulation number A . Theoretically, all points should be embedded along the diagonal of that diagram.

Although it could be expected that recording spectra at longer exposure time of, say 10 s, with only one accumulation (first mode) or using a short exposure time of 0.1 s with hundred accumulations (second mode) are equivalent procedures, both giving comparable spectral intensities, the right choice between these two procedures should be made, having in mind the properties of the excitation source whose spectra are recorded and the properties of the detection system. In a long exposure time mode, illumination of the detector over longer period of time and consequently the appearance of intense radiation can cause saturation effects or effects of approaching a saturation regime. As a result thereof the CCD may start operating outside the range of a linear relationship between the incident photon level and the output signal from CCD. Exceeding the saturation level is usually followed by visible signs like blooming²³ or similar effects like those that can be seen in Fig. 4b. However, the CCD usually does not produce visible signs at the stage of approaching the saturation regime,²⁴ although already operating outside the range of linear response. On the other hand, when the second (accumulation) mode of recording spectra is applied, spectra of sufficient intensities are obtained due to computer summing of particular signals obtained over a short period of time. In that way the saturation or (pre)saturation effects can be avoided.

The content of Fig. 6 speaks in favor of our belief that the anomaly in the D_2/D_1 ratio observed in a number of our experiments should be attributed to the presaturation effects. At small intensities of the spectral lines (Fig. 6a) the deviation of the measured D_2/D_1 ratio from 2 is negligible. It becomes continuously larger with increasing spectral line intensities. At highest intensities measured in this series of experiments, corresponding to the exposure time of $E = 60$ s, the D_2/D_1 ratio becomes approximately 1.6 (Fig. 6c). Note, however, that in the majority of experiments with such a long exposure time the signals are beyond the saturation point and thus are not presented in Fig. 6c. On the other hand, the lines of the same intensity obtained in the second mode (say with $E = 0.2$ s and $A = 300$) show nearly normal D_2/D_1 ratio, close to 2. We obtained the same effect (quasi-normal D_2/D_1) in long-exposure measurement using the filters that transmitted 2.4% and 0.6% of initial radiation.

An important question is whether there is another explanation for the anomaly of the D_2/D_1 ratio. A condition for

obtaining the theoretical ratio of 2 is the existence of the LTE in our plasma. There are several arguments speaking in favor of reliability of the assumption that there is LTE. The first one is that an ratio very close to 2 is always obtained when the intensities of spectral lines are low, *i.e.* at short exposure times. If we did not have the LTE, this would be reflected in both short- and long-exposure time regimes. Further, in our previous studies on AlO^9 and MgO^{10} we showed that the plasma of the present type is in the LTE, at least concerning the vibrational motion modes. Finally, in an extensive study Dunleavy *et al.*⁵ concluded that a similar plasma is in its high-temperature core region in LTE, while in the colder zones at least partial LTE takes place.

Conclusions

A series of spectra involving D_1 and D_2 sodium doublet spectral lines, emitted from the PEO plasma during the aluminum oxidation, have been recorded by varying different detection parameters, like the exposure time, slit width, detection mode, number of accumulations, *etc.* These detailed investigations have been performed in order to find an explanation for the anomalous sodium D_2/D_1 spectral line intensity ratio observed in a number of our spectra. The largest deviations of D_2/D_1 intensity ratios from the theoretical value of 2 have been found in spectra recorded with long exposure time (60 s, 20 s, *etc.*). A correlation between the deviation of the D_2/D_1 ratio from 2 and the overall spectral line intensities has been established. Based on these findings we attribute the anomalous D_2/D_1 intensity ratio to the effect of CCD's approaching a saturation regime and thus to an early indication of saturation occurrence. Let us stress that at the stage of approaching the saturation regime CCD usually does not produce visible signs like blooming or evidently saturated signals, although already operating outside the range of linear response.

Anomalous intensity ratios within doublet components can also be a consequence of complex physical and chemical processes that cause the perturbation of the LTE and of the energy level population. Having in mind that the plasma arising during the electrolytic oxidation process of different metals has not been explored enough in spite of a great number of papers dealing with it, at the beginning of our investigations we did not rule out the possibility that some complex physical and chemical processes induced the anomalous D_2/D_1 intensity ratio. But, at last, we came to the conclusion that the anomaly we observed is due to a more trivial cause connected with our detection system and CCD characteristics, *i.e.* that it represents a manifestation of the CCD's presaturation effect. This presaturation effect can be successfully avoided by recording spectra in the accumulation mode. In this mode successive scans of shorter exposure time are summed to achieve sufficiently high effective intensities without long exposure time, overcoming in that way the risk of CCD overcharging. The same effect could be, of course, achieved by the use of appropriate filters, but a consequence of that would be inconvenient lowering of the intensity of other inherently weak spectral features, particularly of molecular spectral bands.

Acknowledgements

This work is supported by the Ministry of Education and Science of the Republic of Serbia under projects no. 171035 and 172040. We thank Prof. Miljenko Perić for precious contribution to this paper.

References

- 1 A. L. Yerokhin, X. Nie, A. Lezland, A. Mathews and S. J. Dowey, *Surf. Coat. Technol.*, 1999, **122**, 73–93.
- 2 L. Wang, L. Chen, Z. Yan and W. Fu, *Surf. Coat. Technol.*, 2010, **205**, 1651–1658.
- 3 R. O. Hussein, X. Nie and D. O. Northwood, *Surf. Coat. Technol.*, 2010, **205**, 1659–1667.
- 4 M. Petković, S. Stojadinović, R. Vasilić, I. Belča, B. Kasalica and L. Zeković, *Serb. J. Electr. Eng.*, 2012, **9**, 81–94.
- 5 C. S. Dunleavy, L. O. Golosnoy, J. A. Curran and T. W. Clyne, *Surf. Coat. Technol.*, 2009, **203**, 3410–3419.
- 6 R. O. Hussein, X. Nie, D. O. Northwood, A. Yerokhin and A. Mathews, *J. Phys. D: Appl. Phys.*, 2010, **43**, 1–13.
- 7 B. Kasalica, M. Petković, I. Belča, S. Stojadinović and Lj. Zeković, *Surf. Coat. Technol.*, 2009, **203**, 3000–3004.
- 8 S. Stojadinović, J. Jovović, M. Petković, R. Vasilić and N. Konjević, *Surf. Coat. Technol.*, 2011, **205**, 5406–5413.
- 9 S. Stojadinović, M. Perić, M. Petković, R. Vasilić, B. Kasalica, I. Belča and J. Radić-Perić, *Electrochim. Acta*, 2011, **56**, 10122–10129.
- 10 S. Stojadinović, M. Perić, J. Radić-Perić, R. Vasilić, M. Petković and Lj. Zeković, *Surf. Coat. Technol.*, 2012, **206**, 2905–2913.
- 11 J. Jovović, S. Stojadinović, N. M. Šišović and N. Konjević, *Surf. Coat. Technol.*, 2011, **206**, 24–28.
- 12 S. Stojadinović, R. Vasilić, I. Belča, M. Petković, B. Kasalica, Z. Nedić and Lj. Zeković, *Corros. Sci.*, 2010, **52**, 3258–3265.
- 13 O. C. Wilson and P. W. Merrill, *Ap. J.*, 1937, **86**, 44–69.
- 14 N. S. Kovar and R. P. Kovar, *Sol. Phys.*, 1968, **3**, 611–617.
- 15 C. Barbieri, S. Verani, G. Cremonese, A. Sprague, M. Mendillo, R. Consentino and D. Hunten, *Planet. Space Sci.*, 2004, **52**, 1169–1175.
- 16 R. A. Van Calcar, M. J. M. Van de Ven, B. K. Van Uitert, K. J. Biewenga, Tj. Hollander and C. Th. J. Alkemade, *J. Quant. Spectrosc. Radiat. Transfer*, 1979, **21**, 11–18.
- 17 F. E. Irons, *Aust. J. Phys.*, 1980, **33**, 283–301.
- 18 T. G. Slinger, P. C. Cosby, D. L. Huestis, A. Saiz Lopez, B. J. Murray, D. A. O'Sullivan, J. M. C. Plane, C. Allende Prieto, F. J. Martin-Torres and P. Jenniskens, *J. Geophys. Res.*, 2005, **110**, 1–8.
- 19 *Plasma Diagnostics*, ed. W. Lochte-Holtgreven, North Holland, Amsterdam, 1968.
- 20 S. Stojadinović, M. Tadić, I. Belča, B. Kasalica and Lj. Zeković, *Electrochim. Acta*, 2007, **52**, 7166–7170.
- 21 W. S. Boyle and G. E. Smith, *Bell Syst. Tech. J.*, 1970, **49**, 587–593.
- 22 G. E. Smith, *Nobel Lecture: The Invention and Early History of the CCD*, 2009.
- 23 J. R. Janesick, *Scientific Charge-Coupled Devices*, SPIE Press, Monograph Vol. PM83, 2001.
- 24 T. J. Fellers and M. W. Davidson, Hamamatsu articles: *Concepts in Digital Imaging Technology: CCD Saturation and Blooming*, <http://hamamatsu.com/articles>, 2009.
- 25 M. Sarvan, M. Perić, Lj. Zeković, S. Stojadinović, I. Belča, M. Petković and B. Kasalica, *Spectrochim. Acta, Part A*, 2011, **81**, 672–678.
- 26 T. C. Williams and C. R. Shaddix, *Rev. Sci. Instrum.*, 2007, **78**, 123702–123707.
- 27 J. Lindén, C. Knappe, M. Richter and M. Aldén, *Meas. Sci. Technol.*, 2012, **23**, 035201–035208.



CrossMark

The mechanism of evolution of microdischarges at the beginning of the PEO process on aluminum

B. Kasalica ^{*}, J. Radić-Perić, M. Perić, M. Petković-Benazzouz, I. Belča, M. Sarvan

Faculty of Physics, University of Belgrade, Studentski trg 12, P.O. Box 368, 11000 Belgrade, Serbia

ARTICLE INFO

Article history:

Received 22 February 2016

Revised 14 April 2016

Accepted in revised form 20 April 2016

Available online 21 April 2016

Keywords:

Plasma electrolytic oxidation (PEO)

Aluminum

Plasma diagnostics

ABSTRACT

In this study, we present the results of investigation of plasma electrolytic anodization of aluminum by means of different experimental techniques, in few first minutes of the process. Scanning electron microscopy equipped with X-ray energy dispersive spectroscopy was used to study the aluminum oxide coating morphology, microstructure and composition as well as cross-sections of the obtained coating. The mechanism of evolution of microdischarges at the beginning of the plasma electrolytic anodization process is proposed. Our results indicate that during a single discharge event, new inner oxide layer is formed at the bottom of discharge channel, between the metal substrate and the Al_2O_3 layer. That new oxide layer and the gas that remains in the channel seem to present a higher barrier for dielectric breakdown than the original coating layer.

© 2016 Elsevier B.V. All rights reserved.

1. Introduction

Plasma electrolytic anodization/oxidation (PEO) is a complex electrolytic oxidation process in which a metal surface is transformed into a metal oxide coating (aluminum oxide in the present case). The anodizing (PEO) process, which takes place above the dielectric breakdown voltage, is followed by short-living visible microdischarges (plasma sparks) appearing across the anode. Metal oxide coating formed in this process is a result of both electrochemical processes involving migration of O_2^-/OH^- ions from the electrolyte to the aluminum anode and Al^{3+} across the oxide, and of the plasma-chemical reactions due to the electric breakdown of the oxide layer formed already by conventional anodizing process [1–3]. The thickness of oxide layers, limited to several hundred micrometers, depends on the process parameters such as applied voltage, current density, current regime, duration of anodization, electrolyte type etc. It was shown, e.g. for PEO of aluminum, that the obtained coating can be of low porosity, with excellent interfacial adhesion and of high resistance to the abrasive wear and to the corrosion [4–6]. Generally, aluminum oxide coatings formed during the PEO process are of enhanced hardness (depending particularly on the amount of the Al_2O_3 crystalline phase) compared to those obtained in conventionally performed anodization [7].

The morphology and the phase composition of the PEO coating are strongly influenced by the breakdown phenomenon [8,9]. Dielectric breakdown of the oxide film above the breakdown voltage occurs as a consequence of electron avalanche formed under strong electric field. It is induced by structural defects in the oxide film with initial electrons

being injected into the oxide film from the electrolyte [10,11]. As a consequence, in the oxide layer (with possibly incorporated species from the electrolyte) are built plasma channels, in which the processes like melting, evaporation, atomization, and ionization take place [12]. The cations are pushed from the plasma channels into the electrolyte together with the direct ejection of Al from the channels into the coating surface in the contact with electrolyte, forming in this way the coating of the increased thickness [3]. Finally, the plasma cools, with the reaction products being deposited on the walls. In the cooling process, Al_2O_3 in crystal form (γ , α) can be obtained. The results of previous investigations have led to the conclusions that the plasma consists of a central core at about and/or above 7000 K [13], surrounded by lower temperature (up to 3500 K) regions [14].

According to the discharge model based on the locations of discharge initiation, presented by Hussein et al. [15,16], followed by spectroscopic study of the plasma emission spectra as well as of the EDX analysis, during the PEO process three types of plasma can be identified:

- Strong, already mentioned plasma, named “B” [15], is formed due to oxide film dielectric breakdown under strong electric field at metal-oxide interface. The spectra emitted from this type of plasma consist of intensive atomic as well of ionic spectral lines of aluminum, oxygen, hydrogen, sodium (from electrolyte), etc.
- Another type of plasma, named “C” [15], occurs inside the surface holes or (micro) pores, located relatively deeply in the oxide layer. These holes can be filled with gas and/or electrolyte. The discharge in pores is believed to be induced by an initial dielectric breakdown of a barrier layer in the bottom of the micropore [17].
- At last, there is also a weak plasma, named “A” [15], occurring at the interface of the oxide coating and the electrolyte, or in the

^{*} Corresponding author.

E-mail address: kasalica@ff.bg.ac.rs (B. Kasalica).

gas attached to this interface close to the very small holes in the oxide coating.

An extensive study of the influence of the breakdown phenomenon on the formation of pores, channels, “dome shaped” protuberances representing local overgrowth of the film, up to about 0.5 μm in diameter [18], and generally on the coating morphology, has been carried out thus far. It was shown [19,20] that average diameter of obtained discharge channels in the case of the PEO process on aluminum was approximately the same as the thickness of the oxide layer. Recently, several important studies were published [21–24] in which new information about building, magnitude and lifetime of individual discharges was presented. Although carried out under different experimental conditions than those of the present study, these results are closely related to our ones and will be discussed below.

We focus in the present study to the questions concerning the formation and evolution of the channels in the coating surface and try to explain the mechanism of the processes which take place inside these channels in the early phase (few minutes after the beginning) of the PEO process. We relate these processes to the change of electric resistance at particular sites of the coating layer.

2. Experimental details

In the present PEO experiment, oxide films were formed on high purity cold-rolled aluminum (99.999%, obtained from Goodfellow) samples of 10 mm \times 10 mm \times 0.12 mm. The anodization was carried out at current density of 10 mA/cm². For anodization of aluminum we used water solution of 0.1 M boric acid + 0.05 M borax. The electrolyte was prepared using double distilled, deionized water and PA grade chemical compounds. The samples were prepared in two ways: 1. Just cleaned in acetone and ethanol using ultrasonic bath; 2. first cleaned in acetone, then annealed at 350 °C for 5 h and finally electropolished according to Tajima's instructions [25].

The anodization process took place in an electrolytic cell with flat glass windows, presented in Fig. 1. Two platinum wires were used as cathodes.

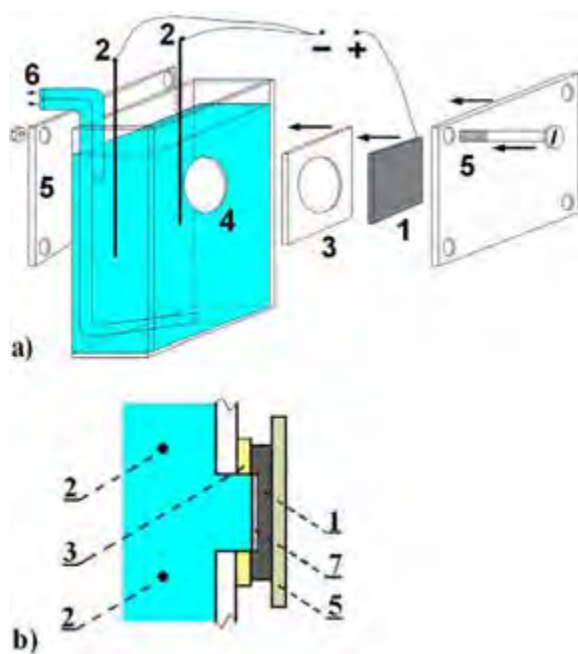


Fig. 1. a) Schematic diagram of the electrolytic cell: 1 - anode, aluminum sample; 2 - cathode, platinum wires; 3 - silicone membrane; 4 - round window on glass cuvettes; 5 - mechanism for holding and fixing of aluminum sample on round window; 6 - chamber-reservoir system; 7 - oxide layer. b) Schematic diagram of the electrolytic cell, cross-section.

This system, used also in our previous experiments [26–30], has been modified in order to enable anodization of only one of the two sample surfaces. We can now observe and analyze the PEO coating: a) at the side in contact with the electrolyte (being the usual procedure); b) at the side in contact with the metal substrate, by solving the metal in an appropriate acid; furthermore, by removing the coating from the metal substrate, we can investigate the “finger prints” of the PEO oxide on the metal surface; c) cross-section of the PEO coating. The sample has been attached on a circle-shaped window and pressed firmly by a plate to prevent leakage of the electrolyte. During anodization, the electrolyte circulated through the chamber-reservoir system, and the control temperature sensor was situated beside the sample. The temperature of the electrolyte was maintained during anodization to within 0.1 °C. In some anodized samples, aluminum was removed in a CuCl₂-based solution [100 mL HCl (38%) + 100 mL H₂O + 3.4 g CuCl₂·H₂O].

Scanning electron microscope (SEM) JEOL 840A equipped with X-ray energy dispersive spectroscopy (EDX) was used to characterize morphology and chemical composition of formed surface coatings. The morphology of surface coatings was characterized using an atomic force microscope (AFM; Veeco Instruments, model Dimension V). Thermo Scientific iCAP 6500 Duo inductively coupled plasma optical emission spectrometry (ICP-OES) was used to analyze composition of electrolyte after anodization of the sample.

For obtaining XRD patterns of oxide coatings, Rigaku Ultima IV diffractometer was used.

3. Results and discussion

3.1. Voltage and current variation during the PEO process on aluminum

Typical voltage and current vs. time curve obtained by aluminum anodization in 0.1 M solution of boric acid and borax (inorganic electrolyte) is shown in Fig. 2. In stage 1, relatively uniform growth of a barrier anodic oxide layer, at a constant current density ($j = 10 \text{ mA/cm}^2$), is characterized by a linear increase in the anodization voltage, corresponding to a conventional metal anodizing process. Uniform film thickening is terminated by attaining dielectric breakdown voltage ($\sim 400 \text{ V}$). During anodization, the total current density is the sum of the ionic current density and of electron current density. In this stage, the ionic current is two to three orders of magnitude larger than the electronic component [11].

In the second stage (2), avalanche multiplication of electrons takes place, corresponding to apparent deflection from linearity of the voltage–time curve. In this stage a relatively low voltage increase (compared with the stage I) is required to maintain the same total current density, due to the independence of the electron current density of the anodic oxide film thickness. After the breakdown the voltage–time slope decreases.

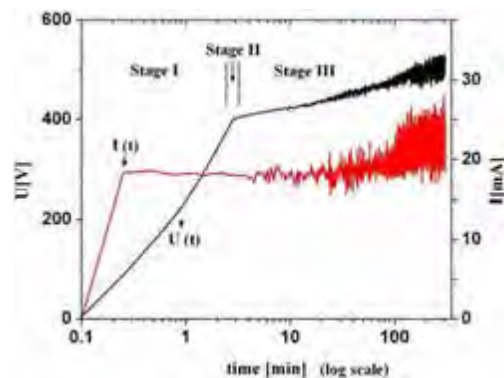


Fig. 2. Voltage–time and current–time responses during PEO process on aluminum in 0.1 M solution of borax and boric acid.

Further anodization results in a nearly constant value of the voltage of anodization (stage 3). In this stage, the fraction of electron current density becomes dominant. The total current density is almost independent of oxide film thickness.

3.2. Morphology and chemical composition of PEO coatings and electrolyte after PEO treatment

Scanning electron microscopy (SEM) equipped with X-ray energy dispersive spectroscopy (EDX) was used to study PEO coating microstructure.

In Fig. 3 is presented a high-magnification image of free PEO coatings surfaces on aluminum obtained 1 min after beginning of PEO process. It is characterized by numerous small discharge pores (average diameter in range of $0.5\ \mu\text{m}$ – $0.6\ \mu\text{m}$). As mentioned before [29], thickness of the barrier oxide layer is in the range of $0.05\ \mu\text{m}$ – $0.5\ \mu\text{m}$ and its average diameter is of comparable magnitude. There are also significant regions of surface where no discharge pores are present.

EDX analyze was used to investigate the difference in composition of these two different regions. The results are presented in Table 1. One EDX spectrum was taken in the region where a single discharge took place (Spectrum 2, Fig. 3), while the other one was taken in the area around the discharge channel where there were no visible changes in oxide caused by the PEO treatment (Spectrum 1). It is obvious that the content of Al inside the discharge channel is higher, while the content of oxygen is significantly decreased.

In course of time the area of surface covered with the micropores becomes continuously larger, indicating that new discharge sites are produced in spite of the fact that it should be expected that the anodic current would more easily pass through already present channels.

The main questions are why the EDX results indicate that the contents of aluminum and oxygen are significantly different in microchannels and at the smooth layer surface, what happens with these discharge channels after they were made, how deep they are, and why the discharge channels finally present higher dielectric barrier than rest of the oxide coating?

In order to answer these questions, it was needed to see how cross-sections of the PEO layer looked like.

It is not an easy task to obtain PEO coating cross-sections with preserved structures. In Fig. 4a and b we see the results of two different attempts. Fig. 4a represents a cross-section SEM image of the aluminum sample with PEO coating obtained by simple mechanical cutting, and Fig. 4b is the cross-section image obtained on a sample that was wrapped in epoxy and then polished. Because aluminum is soft metal and the formed PEO layer is brittle, cross-sections obtained by mechanical cuttings cannot provide good insight into the structure. The method where aluminum sample was wrapped in epoxy and then polished is

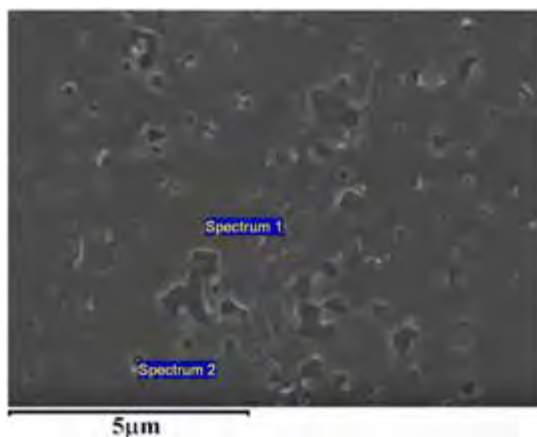


Fig. 3. SEM micrographs of aluminum oxide coating surface formed 1 min after beginning of the PEO process.

Table 1

EDX analysis of the oxide coating surface shown in Fig. 3.

	Atomic (%)	
	O	Al
Spectrum 1	54.25	45.75
Spectrum 2	30.83	69.14

also problematic. During polishing, metal and oxide particles enter into discharging channels and the real structure of oxide coating remains unknown.

In order to make possible recording of cross sections we removed the Al substrate, mechanically broke a part of the oxide layer presented in Fig. 3 and obtained the images such as two typical ones presented in Fig. 5a and b. They correspond to the time 1 min after the beginning of the PEO process. In Fig. 5a is shown the contour of a single channel, while in Fig. 5b are seen two close lying channels. We discuss this topic in some details below; at this place we only point out that the channels pass through the whole coating layer, i.e. that their depth is as large as the thickness of the coating layer. We can also identify (half-) spherical cap forms (calottes) and holes, particularly at the places where the coating layer was in contact with the metal. Finally, at the right edge of Fig. 5c (taken 6 h after beginning of the PEO process) is clearly seen a new coating layer built through joining of calottes formed at the bottom of the craters.

Since we had managed to develop the electrolyte chamber where only one side of the aluminum sample is in contact with electrolyte during the PEO process (Fig. 1), we were able later to remove metal easily

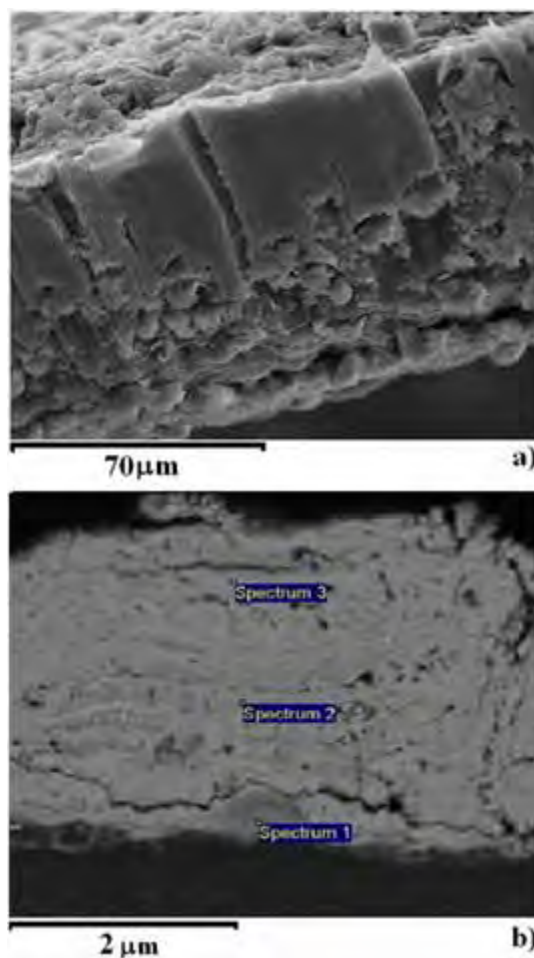


Fig. 4. SEM images of cross-section of PEO coating on aluminum; a) mechanical break and b) wrapped in epoxy and polished.

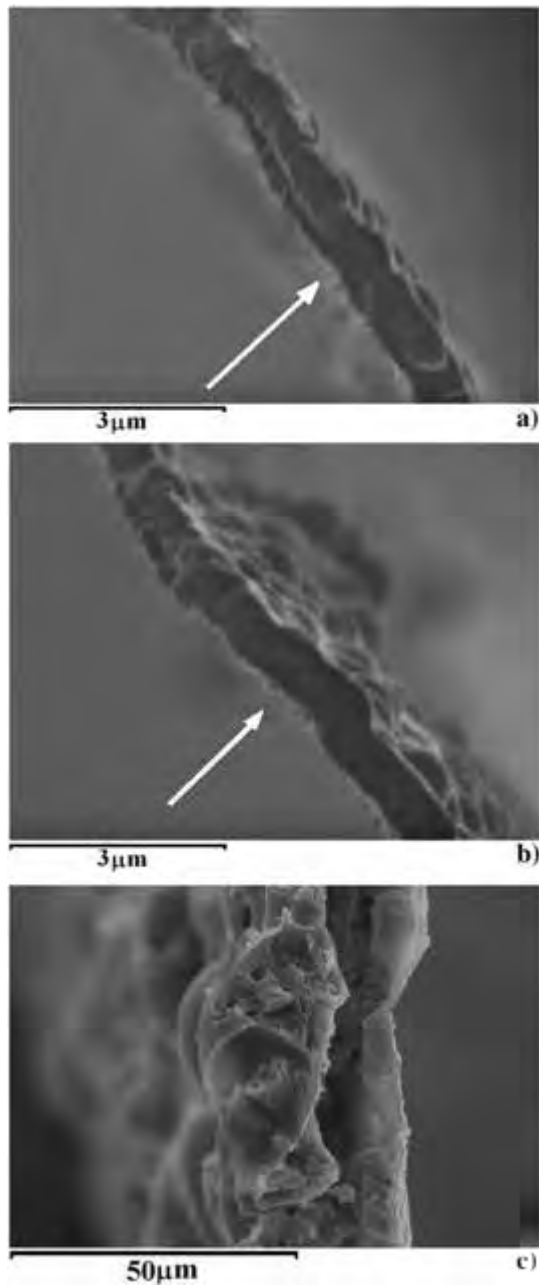


Fig. 5. a, b, SEM cross-section images of PEO oxide layer on aluminum. c. At right edge is seen new coating layer built through joining of calottes formed at the bottom of the craters, taken 6 h after beginning of the PEO process.

and to obtain preserved cross-section and surface of coating that was in contact with metal. Fig. 6 represents a SEM image of such a layer on the side that was in contact with metal. This layer has thickness of approximately 0.6 μm . This image supports the above finding that discharge channels are as deep as the thickness of the layer. We can also easily distinguish (half-) spherical cap forms (calottes) and holes.

Using another aluminum sample anodized under the same experimental conditions and removing this time PEO coating, it was also possible to see morphology of obtained metal surfaces that were in contact with coating and to see how they correspond to the same-side surfaces of PEO coating. In Fig. 7 is presented an AFM image of such a metal surface, representing “finger prints” of the features appearing in Fig. 6.

In order to obtain better insight and to answer the proposed questions, it was needed to investigate morphology of PEO coatings on aluminum samples, both electropolished and not electropolished, formed

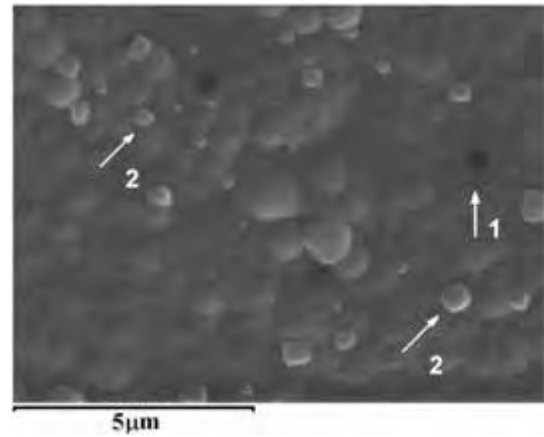


Fig. 6. SEM image of the surface of oxide layer obtained in PEO process on aluminum (surface that was in contact with metal before its removing): 1 - discharging channel and 2 - crystal islands of alumina.

before the beginning of the PEO process and in its several first minutes. The surfaces of electropolished and not electropolished samples of aluminum anodized under the voltage 350 V, i.e. before first visible microdischarges occurred, showed significant differences, as seen in Fig. 8. Although there are no visible microdischarges under these conditions, we can identify in Fig. 8b little holes in the not electropolished sample, connected with the beginning of breakdown events. On the other side, the surface of electropolished aluminum sample, anodized under the same condition is clean, as seen in Fig. 8a. It is well known that macro- and micro-defects in oxides (fissures, micropores, flaws etc.) are responsible for breakdown [18]. The breakdown voltage is lower for degreased samples, and slightly higher for electropolished ones [29,31]. Namely, electropolishing gives the cleanest and smoothest surface and that is the reason why there are no discharging channels on this surface under the mentioned voltage.

After the beginning of breakdown, increasing number of microdischarges can be noticed [6]. Surface topography of oxide coatings in the beginning stages of PEO process (5 s, 10 s, 15 s, 30 s after first visible microdischarges occurred) shows no significant differences for both samples in the sense of dimension of channels, but there is a visible increase in their number. On both samples anodized under the same conditions there are small regions where surface was changed under the PEO process but also regions where no visible changes occur, Fig. 9. The only difference between samples anodized 10 s, 15 s, 30 s, and 1 min after breakdown, is noticeable increase in the area of those regions that were changed by the PEO process. The same trend can be observed on surfaces (both electropolished and not electropolished ones) that were in contact with metal, Fig. 10.

EDX analyze of two different regions, at the place of a spherical cup (Fig. 11, Spectrum 1) and at a neighboring place where dielectric breakdown did not take place (Fig. 11, Spectrum 2) showed the same ratio of

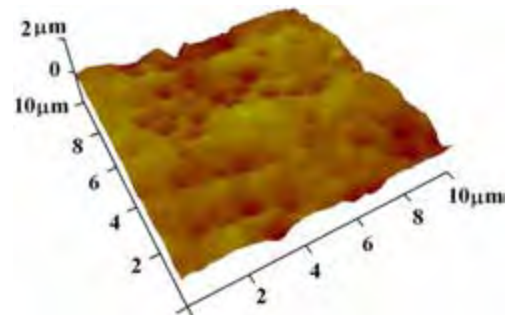


Fig. 7. AFM image of aluminum surface, taken after 1 min of PEO process, obtained after removing of oxide layer (non electropolished sample).

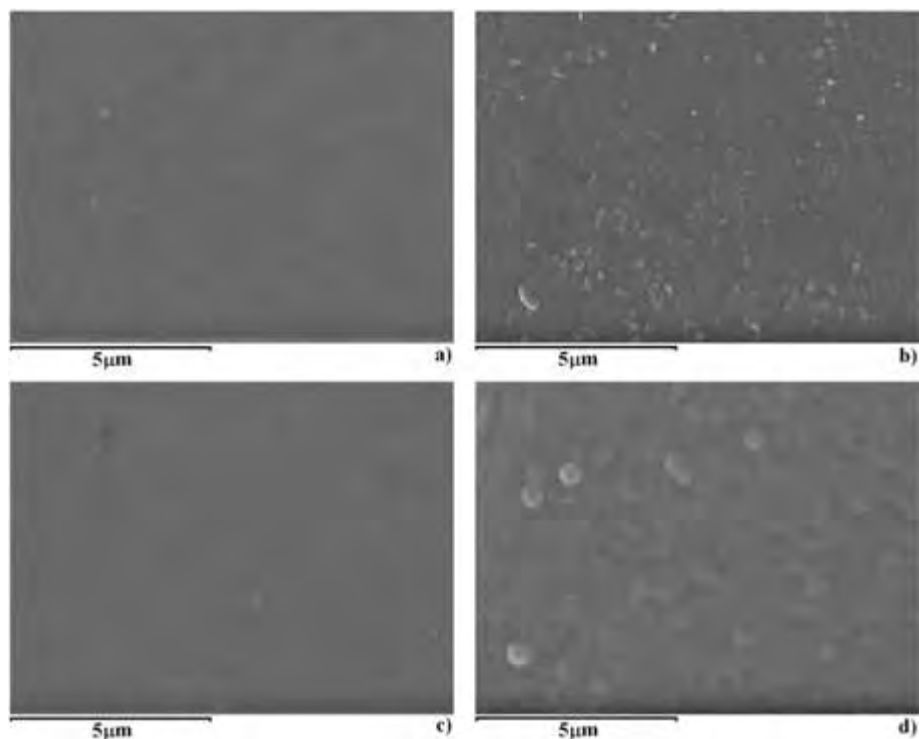


Fig. 8. SEM micrographs of oxide surface on aluminum anodized before first microdischarges occurred (voltage: 350 V): a) electropolished sample, b) nonelectropolished sample, c) electropolished sample, surface of oxide layer that was in contact with aluminum, and d) nonelectropolished sample and surface of oxide layer that was in contact with aluminum.

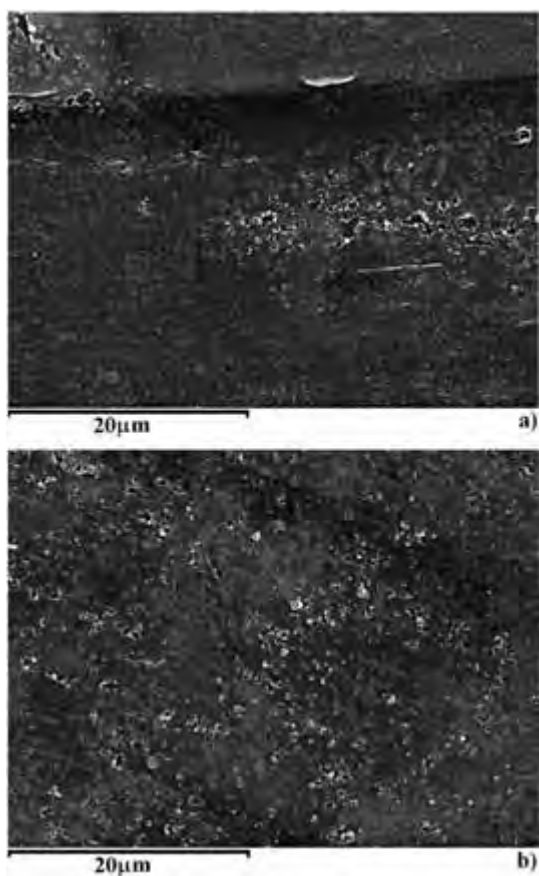


Fig. 9. SEM images of surface of the same aluminum sample, non-electropolished: a) 5 s after first visible microdischarges occurred and b) 30 s after first visible microdischarges occurred.

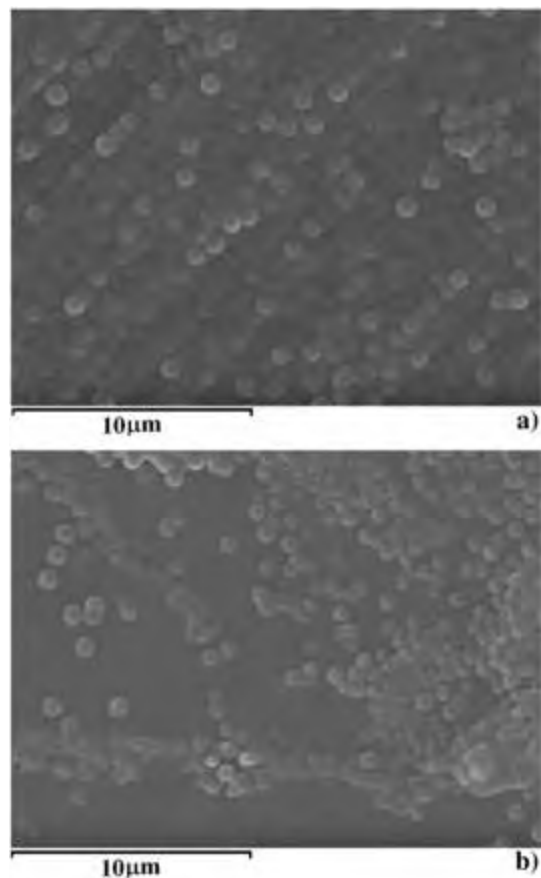


Fig. 10. SEM images of PEO layer on the side that was in contact with aluminum during anodization, 5 s after first visible microdischarges occurred: a) non electropolished samples and b) electropolished samples.

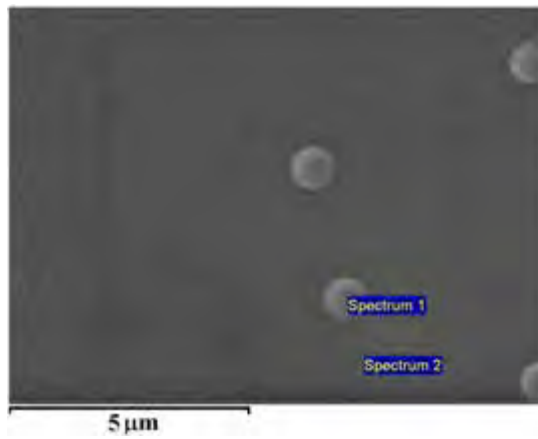


Fig. 11. SEM images of one spherical form with EDX analysis, 5 s after first visible microdischarges occurred.

Al and O. Dimension and profile of one spherical cap form is presented in Fig. 12. Fig. 13a shows AFM images of a coating surface that was in contact with metal.

Comparing this image with images of cross-sections in Fig. 5 and all other obtained results, it can be concluded that during one single PEO event, the whole material from discharge channel has been melted and evaporated. In the same process a part of the metal surface at the end of the discharging channel also melts and evaporates.

In order to carry out XRD analysis, oxide coatings were detached from the Al substrate. Since oxide films (produced within 30 s–300 s of the PEO process) were relatively thin, in order to obtain enough XRD response, we performed XRD investigations using Rigaku Ultima IV diffractometer in low angle/thin film configuration. Fig. 14 shows XRD patterns of oxide coatings formed at various stages of PEO process.

As expected, in short periods of PEO the coatings are partly crystallized and we have detected only gamma alumina crystal phase. The intensity of detected peaks increases with PEO time, indicating growth of crystal phase with increasing PEO time. The possible mechanisms of gamma alumina production are: Conversion of amorphous alumina in gamma alumina due to local heating in PEO channels and direct crystal growth at the bottom of the channels due to interaction of plasma and melted Al.

All the results obtained lead us to conclude that new oxide layer, on the bottom of discharge channel, with presumably increased percentage of crystalline phase [18] and the remaining gas in channels becomes new barrier for dielectric breakdown, higher than the barrier caused by the presence of the original layer.

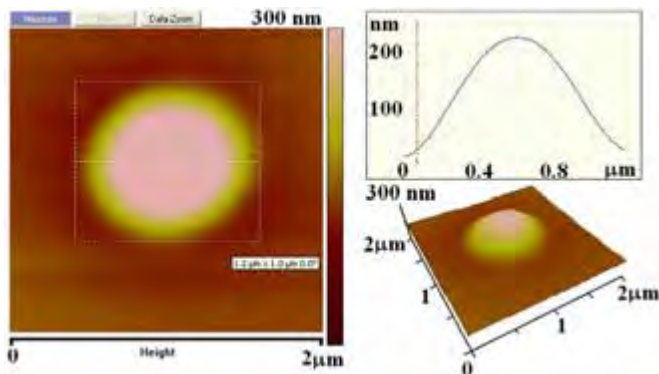


Fig. 12. AFM images of one randomly chosen oxide spherical cap obtained in PEO process on aluminum, 5 s after first visible microdischarges occurred.

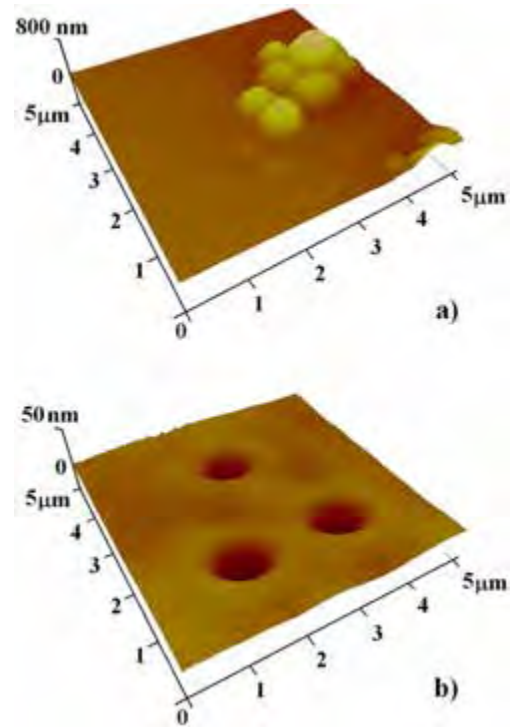


Fig. 13. AFM images of electropolished aluminum samples: a) Surface of PEO layer on the side of metal and b) surface of metal on the side of PEO coating, 5 s after first visible microdischarges occurred.

3.3. ICP-OES analysis of electrolyte during PEO

Knowing that during the PEO process, material from discharge channels is released in electrolyte, ICP-OES method was used to investigate how the content of aluminum is changed in electrolyte in course of time. The results are presented in Table 2.

The content of aluminum in electrolyte increases almost linearly with the PEO time. At the beginning of anodization, as expected, it is negligibly small but after 2 h it takes a value of roughly 40 mg/L. These results also indicate that during the PEO process, most of the content from the inside of channels evaporates, the created discharge channels remain empty (filled only with gas) and only on their bottoms, embedded on the metal surface we can detect an inner oxide layer.

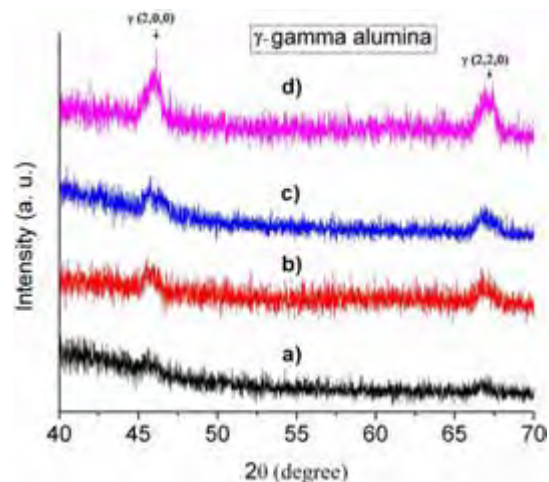


Fig. 14. XRD patterns of oxide coatings formed at various stages of PEO: a) 0.5 min; b) 1 min; c) 2 min; d) 5 min.

Table 2
IOS-ICP analysis of electrolyte in different stages of PEO.

Time of anodization (min)	Content of Al (mg/L)
0	0.00
5	2.57
15	8.94
60	25.10
120	41.95

3.4. Average energy needed for one discharging PEO event

Assuming, based on our previous investigations, that the average energy of one PEO event is approximately $\sim 10^{-1} \mu\text{J}$ [29], the question is if that is enough energy to cause melting of oxide and evaporation of metal in a discharge channel?

From a randomly chosen AFM image presented in Fig. 13, dimensions (height and base radius) of a spherical cap built at the bottom of a channel can be obtained, and based on these quantities we can calculate its volume. With the height of $h \sim 0.2 \mu\text{m}$ and base radius $r \sim 0.5 \mu\text{m}$, we obtained the volume $V = h(3r^2 + h^2)\pi/6 \sim 0.8 \times 10^{-19} \text{ m}^3$. Knowing that the molar volume of aluminum is $\sim 10^{-5} \text{ m}^3/\text{mol}$ and molar evaporation heat is $\sim 294.4 \text{ kJ/mol}$, a simple calculation gives the energy needed for melting and evaporation of substrate. That energy for the spherical cap from Fig. 13 takes the value of $\sim 3 \times 10^{-3} \mu\text{J}$. The energy required to melt and evaporate the substance both from this spherical cup and the whole channel above it, assumed to have cylindrical form with the depth of $0.5 \mu\text{m}$ (i.e. the volume of $\sim 4 \times 10^{-19} \text{ m}^3$), would be roughly $0.02 \mu\text{J}$. In our previous experiments we managed to isolate one breakdown event and obtained the average energy of $\sim 0.2 \mu\text{J}$ [29]. Our result shows that only a small amount of the energy for one PEO event is enough to heat, melt and evaporate aluminum at the bottom of discharge channel. The remaining part of that energy is used for evaporation of material in discharge channel and local heating of oxide and surrounding metal.

The results estimated above can be compared with those published by Troughton et al. [24]. Based on the result of one of their previous studies [23] these authors assumed that a typical volume of substrate being oxidized during one discharge was $\sim 10 \mu\text{m}^3$, i.e. somewhat larger than our estimate. The energy required to melt, vaporize and raise the temperature of the corresponding mass of the substrate to that of the plasma was calculated by means of the formula $Q = m(C_p\Delta T + \Delta H_{\text{melt}} + \Delta H_{\text{vap}})$ where C_p is the specific heat ($\sim 1 \text{ J g}^{-1} \text{ K}^{-1}$), ΔH_{melt} (400 J g^{-1}) is the latent heat of melting, and ΔH_{vap} ($10,500 \text{ J g}^{-1}$, being practically identical to the molar evaporation heat for Al we used) is the latent heat of vaporization. Because the plasma temperature was assumed to be not higher than $10,000 \text{ K}$, the contribution of the first term in the equation for Q is comparable to that of the third one, and since $\Delta H_{\text{melt}} \ll \Delta H_{\text{vap}}$, the second term is negligible. The result obtained for Q was $0.6 \mu\text{J}$, i.e. roughly 30 times larger than our one. However, the conclusion of the authors was the same as ours, namely, that “Vaporizing this quantity of material requires just $0.6 \mu\text{J}$, which is an insignificant fraction of the total energy input ($\sim 1 \text{ mJ}$).” Numerical differences of particular result from our study and the corresponding results published in Ref. [24] should be ascribed to different experimental conditions (in Refs. [23, 24] the PEO processing was carried out at 50 Hz AC) and random choice of the discharge channel (the difference in the values for Q would have been reduced by factor two if we had taken into account the energy needed for raising the temperature to $10,000 \text{ K}$).

3.5. Calculation of microdischarge plasma composition

Based on the results of the present work concerning the form and the magnitude of channels on the aluminum oxide layer, of the microcharge temperatures measured in our previous studies [32–34], as well as on the models proposed by the other authors we carried out computations of the plasma containing aluminum and oxygen in atomic

ratio 2:3. We assumed that we have spherical microchannels with radius of $0.5 \mu\text{m}$, that the core temperature is 8000 K , and that at the periphery is 1000 K . The calculations were carried out using the method described elsewhere [35–37]. The thermochemical data were taken from JANAF Tables [38]. The results are presented in Fig. Fig. 15. In the central zone of the plasma the dominating forms of aluminum are atomic Al and ionic Al^+ being present in comparable amounts, and that of oxygen is atomic O. However, in the vicinity of the channel walls and at the bottom, where the temperature is relatively low ($< 3000 \text{ K}$), the most abundant compounds involving aluminum are Al_2O_2 and AlO_2 molecules. During the cooling process, Al_2O_3 in solid state form could be formed involving these molecules, already at the temperatures lower than 2327 K (which is the melting point of $\alpha\text{Al}_2\text{O}_3$), via the following reaction paths:

- $2\text{AlO}_2 (\text{g}) \rightarrow \text{Al}_2\text{O}_3 (\text{s}) + \frac{1}{2}\text{O}_2 (\text{g})$, with reaction Gibbs energy: $\Delta G = -660.50 \text{ kJ}$, at 2000 K .
- $2\text{Al}_2\text{O}_2 (\text{g}) \rightarrow \text{Al}_2\text{O}_3 (\text{s}) + \frac{1}{2}\text{O}_2 (\text{g}) + 2\text{Al} (\text{g})$, with reaction Gibbs energy: $\Delta G = -174.99 \text{ kJ}$, at 2000 K .

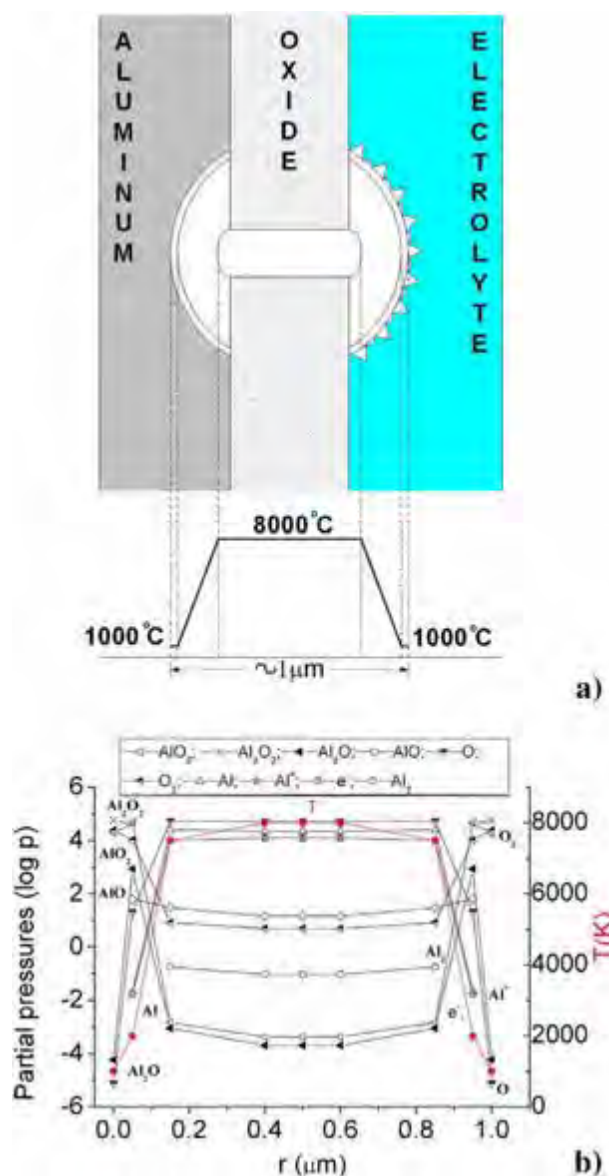


Fig. 15. a) Schematic presentation of a microdischarge with assumed temperature distribution. b) Composition of plasma containing aluminum and oxygen in atomic ratio 2:3.

Symbols s and g in the brackets denote solid and gas phases, respectively.

3.6. Proposed scheme of dielectric breakdown during PEO of aluminum

Based on all presented results we propose the following schema of the PEO process on aluminum (Fig. 16): Macro and micro defects and other inhomogeneities are initial spots for dielectric breakdown, Fig. 16a. As found in recent studies [23–24] (indeed, carried out under experimental conditions differing from the present one) individual discharges tend to occur in “cascades”, at well-defined sites on the coating layer. A breakdown event does not stop on the border metal – oxide. It continues and heats the metal surface. Metal melts and evaporates in electrolyte, Fig. 16b, leaving spherical cap forms of Al_2O_3 on the metal surface. A new oxide layer is built at the bottom of discharge channel (Fig. 16c). It, combined with the remaining high-pressure gas in the

channel gradually becomes a higher barrier for dielectric breakdown than the original coating layer. Consequently, new initial spots are formed. Finally, spherical cap forms join one another forming in this way a new coating layer (Fig. 16d).

4. Conclusions

In this study, we present the results of extensive investigation of the plasma electrolytic anodization of aluminum by means of different experimental techniques.

We identified at the bottom of discharge channels a new inner coating layer at and below the initial border between the metal substrate and the Al_2O_3 layer. Taking into account increased crystallinity of this new layer and presence of the remaining high-pressure gas in the channel, new model of mechanism of evolution of microdischarges at the beginning of the PEO process on aluminum is proposed. It is similar to that suggested by Nominé et al. [23] (see Fig. 5 of Ref. [23]) but we offer an alternative explanation for raising of the electric resistance and final quenching of the current through a channel. Nominé et al. quote: “It’s probably at this point that there is violent ejection of molten oxide from the core to the channel, giving rise to characteristic volcanic craters on the free surface of the coating.” We suggest the possibility that increase of the resistance arises as combination of the two findings mentioned in the first two sentences of this paragraph, causing in this way formation of new initial spots for breakdown events in first several minutes of PEO process. This model is supported by consideration of thermodynamic effects in the framework of a standard model for microplasmas appearing in the PEO process.

Acknowledgement

This work is supported by the Ministry of Science and Technological Development of the Republic of Serbia under Projects No. 171035.

References

- [1] J. Yahalom, T.P. Hoar, *Electrochim. Acta* 15 (1970) 877.
- [2] S. Tajima, N. Baba, K. Shimizu, I. Mizuki, *Electrocompon. Sci. Technol.* 3 (1976) 91.
- [3] L.O. Shizhko, A.L. Yerokhin, A. Pilkington, N.L. Gurevina, D.O. Misnyankin, A. Leyland, A. Matthews, *Electrochim. Acta* 49 (2004) 2085.
- [4] A.L. Yerokhin, X. Nie, A. Leyland, A. Matthews, S.J. Dowey, *Surf. Coat. Technol.* 122 (1999) 73.
- [5] X. Nie, E.I. Meletis, J.C. Jiang, A. Leyland, A.L. Yerokhin, A. Matthews, *Surf. Coat. Technol.* 149 (2002) 245.
- [6] S. Stojadinović, R. Vasilčić, I. Belča, M. Petković, B. Kasalica, Z. Nedić, Lj. Zeković, *Corros. Sci.* 52 (2010) 3258.
- [7] J.A. Curran, T.W. Clyne, *Surf. Coat. Technol.* 199 (2005) 168.
- [8] H. Kalkanci, S.C. Kurnaz, *Surf. Coat. Technol.* 203 (2008) 15.
- [9] Dehnavi, X.Y. Liu, B.L. Luan, D.W. Shoesmith, S. Rohani, *Surf. Coat. Technol.* 251 (2014) 106.
- [10] S. Ikonopisov, *Electrochim. Acta* 22 (1977) 1077.
- [11] J.M. Albella, I. Montero, J.M. Martínez-Duart, *Electrochim. Acta* 32 (1987) 255.
- [12] M.D. Klappiv, *Mater. Sci.* 35 (1999) 279.
- [13] R.O. Hussein, P. Zhang, X. Nie, Y. Xia, D.O. Northwood, *Surf. Coat. Technol.* 206 (2011) 1990.
- [14] C.S. Dunleavy, I.O. Golosnoy, J.A. Curran, *Surf. Coat. Technol.* 203 (2009) 3410.
- [15] R.O. Hussein, X. Nie, D.O. Northwood, A. Yerokhin, A. Matthews, *J. Phys. D. Appl. Phys.* 43 (2010) 105203.
- [16] R.O. Hussein, X. Nie, D.O. Northwood, *Surf. Coat. Technol.* 205 (2010) 1659.
- [17] A.L. Yerokhin, L.O. Shizhko, N.L. Gurevina, A. Leyland, A. Pilkington, A. Matthews, *J. Phys. D. Appl. Phys.* 36 (2003) 2110.
- [18] G. Shimizu, G.E. Thomson, G.C. Wood, *Thin Solid Films* 92 (1982) 231.
- [19] S. Stojadinović, I. Belča, M. Tadić, B. Kasalica, Z. Nedić, Lj. Zeković, *J. Electroanal. Chem.* 619–620 (2008) 125.
- [20] S.P. Sah, Y. Tatsuno, Y. Aoki, H. Habazaki, *Corros. Sci.* 53 (2011) 1838.
- [21] J. Martin, A. Melhem, I. Shchedrina, T. Duchanoy, A. Nominé, G. Henrion, T. Czerwicz, T. Belmonte, *Surf. Coat. Technol.* 221 (2013) 70.
- [22] C.S. Dunleavy, J.A. Curran, T.W. Clyne, *Appl. Surf. Sci.* 268 (2013) 397.
- [23] A. Nominé, S.C. Troughton, A.V. Nominé, G. Henrion, T.W. Clyne, *Surf. Coat. Technol.* 269 (2015) 125.
- [24] S.C. Troughton, A. Nominé, A.V. Nominé, G. Henrion, T.W. Clyne, *Appl. Surf. Sci.* 359 (2015) 495.
- [25] S. Tajima, K. Shimizu, N. Baba, S. Matsuzawa, *Electrochim. Acta* 22 (1977) 845.
- [26] B. Kasalica, I. Belča, S. Stojadinović, M. Sarvan, M. Perić, Lj. Zeković, *J. Phys. Chem.* 111 (2007) 12315.

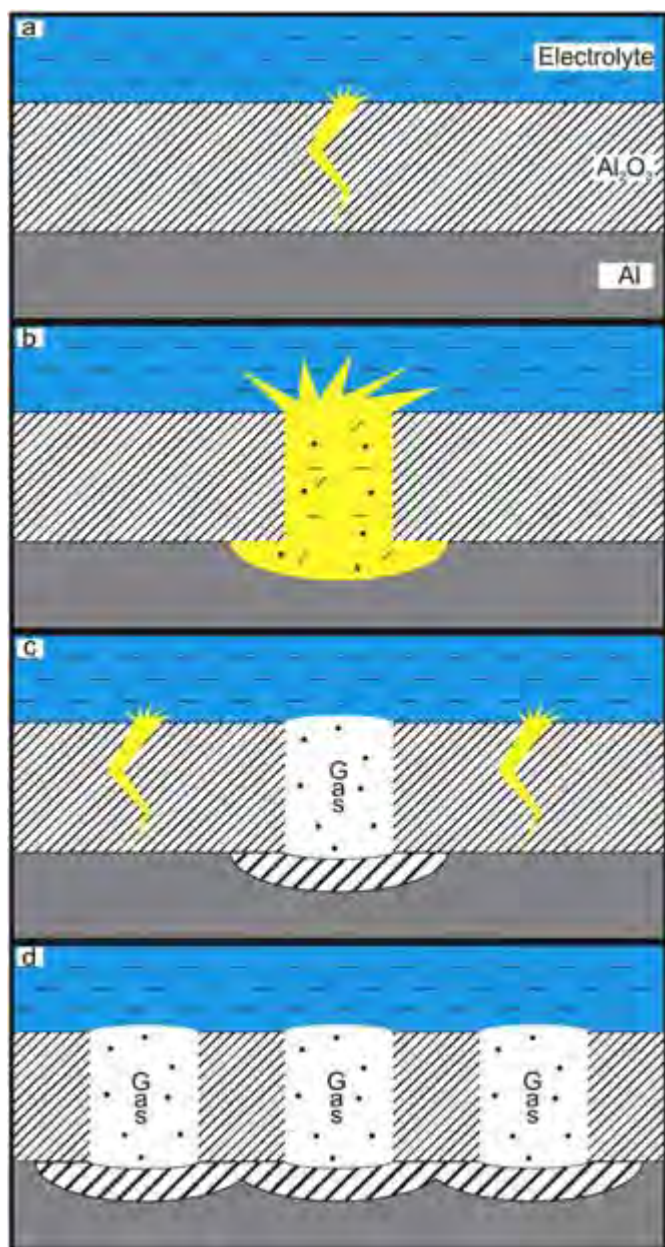


Fig. 16. Proposed scheme of PEO process on aluminum.

- [27] S. Stojadinović, I. Belča, M. Tadić, B. Kasalica, Z. Nedić, Lj. Zeković, J. Electroanal. Chem. 619–620 (2008) 125.
- [28] S. Stojadinović, M. Tadić, I. Belča, B. Kasalica, Lj. Zeković, Electrochim. Acta 52 (2007) 7166.
- [29] B. Kasalica, M. Petković, I. Belča, S. Stojadinović, Lj. Zeković, Surf. Coat. Technol. 203 (2009) 3000.
- [30] S. Stojadinović, R. Vasilic, Z. Nedić, B. Kasalica, I. Belča, Lj. Zeković, Thin Solid Films 519 (2011) 3516.
- [31] S. Stojadinović, R. Vasilic, I. Belča, M. Tadić, B. Kasalica, Lj. Zeković, Appl. Surf. Sci. 255 (2008) 2845.
- [32] J. Jovović, S. Stojadinović, N.M. Šišović, N. Konjević, J. Quant. Spectrosc. Radiat. Transf. 113 (2012) 1928.
- [33] S. Stojadinović, M. Perić, J. Radić-Perić, R. Vasilic, M. Petković, Lj. Zeković, Surf. Coat. Technol. 206 (2012) 2905.
- [34] M. Sarvan, J. Radić-Perić, B. Kasalica, I. Belča, S. Stojadinović, M. Perić, Surf. Coat. Technol. 254 (2014) 270.
- [35] W.B. White, S.M. Johnson, S.B. Dantzig, J. Chem. Phys. 28 (1958) 751.
- [36] J. Radić-Perić, M. Perić, Spectrochim. Acta 35 (1980) 297.
- [37] S. Stojadinović, M. Perić, M. Petković, R. Vasilic, B. Kasalica, I. Belča, J. Radić-Perić, Electrochim. Acta 56 (2011) 10122.
- [38] JANAF Thermodynamical Tables: Nat. Stand. Ref. Data Series, Vol. 27, US Nat. Bur. Stand., 1971. M.W. Chase Jr., NIST-JANAF Thermodynamical Tables, J. Phys. Chem. Ref. Data (1999), fourth ed.